Patient-Specific Dosimetry for Targeted Radionuclide Therapy Using Deformable Anthropomorphic Phantoms

By

Susan Danica Kost

Dissertation

Submitted to the Faculty of the

Graduate School of Vanderbilt University

in partial fulfillment of the requirements

for the degree of

DOCTOR OF PHILOSOPHY

in

Physics

August, 2015

Nashville, Tennessee

Approved:

Michael G. Stabin, Ph.D.

David R. Pickens, Ph.D.

Manuel Morales-Paliza, Ph.D.

Kelly Holley-Bockelmann, Ph.D.

W. Paul Segars, Ph.D.

Ronald R. Price, Ph.D.

To all who find themselves on an unexpected journey in life.

And to those who supported me along this one.

I am among those who think that science has great beauty.
–Marie Curie

ACKNOWLEDGMENTS

I would not have seen this dissertation journey to completion without the support and encouragement from numerous people.

First, thank you to my advisor Dr. Michael Stabin for taking me in as a down-and-out graduate student and giving me the opportunity and motivation to become the scientist I am today. Your excitement and dedication to the field of internal dosimetry is infectious and inspiring.

I would also like to thank the rest of my committee: Drs. Ronald Price and David Pickens (the "Dr. P's") for always having an open door for questions and the occasional graduate school complaint; Dr. Manuel Morales for your professional mentoring as a clinical medical physicist and optimistic outlook on life; Dr. Kelly Holley-Bockelmann for showing me how to navigate a field with too few women and become a superstar in the process; and lastly, Dr. Paul Segars for graciously serving as a member of my committee despite the distance between Vanderbilt and Duke Universities and for providing me with the initial code for the Phantom Morphus software. There is no way I could have created something so complete (and functional) without it!

I am grateful to all those who have collaborated with me on this project. I am especially indebted to Dr. Yuni Dewaraja at the University of Michigan for providing me the time-sequenced SPECT/CT patient data and co-authoring my publication on VIDA. Thank you to Dr. Rick Abramson for reviewing the manually-segmented CT images and verifying that I did, in fact, define the pancreas correctly. And many thanks to Darren Julao for helping me develop the Point Cloud Fit algorithm and write the C++ code to make it actually work; you are the best brother-in-law on earth!

Fellow graduate students Diana Carver, Sarah Crews, Desmond and Lauren Campbell, Jennifer Alexander, and Ken Lewis, you, above all others, understand the daily struggle of the Ph.D. candidate. I am thankful to have gone on this crazy adventure with you right beside me. I am honored to call you my friends and look forward to sharing in all our future successes.

Lisa Genovese and Catherine Frame, thank you for being the best of friends for which I could have ever dreamed. Our "family" dinners every Sunday night gave me something to look forward to during tough weeks. I love you both to pieces!

Rob Garner, thank you for sticking around despite experiencing at times some of my more unfavorable personal qualities. You are truly my best friend. Thank you for feeding my cats those weeks I was in Seattle coding with Darren and for watching countless hours of Investigation Discovery on TV because I like it.

Thank you to Ryan Gillespie for my emotional education. I am truly grateful for all the hours we sat across from each other. I am a far better and stronger person for the experience.

Thank you to all my friends, near and far, including Stacey Jones, Jessica Dillon, Mike Hussey, the Dawson family, Nick Fraser, Justin Howard, Amy Patrick, Eugenia Perevalova, Armaghan Naik, the Nolletti family, the Garner family, Jeremiah Sager, and many, many others for cheering me on. Your support and encouragement throughout these years is immeasurable.

And lastly, thank you to my family for your continued support. I love you more than words express. Thank you to my parents for knowing the importance of an education and providing me with opportunities to receive this one. Thank you to my sister Amanda for pushing me to be my best and taking me out to fancy dinners that a graduate student cannot afford. And to my nephew Lonan and niece Jaelithe, you make the future brighter and my world a magical place.

TABLE OF CONTENTS

Page

ACKNOWLEDGMENTS iv

LIST OF TABLES viii

LIST OF FIGURES ix

ABBREVIATIONS xii

Chapter

I. INTRODUCTION 1

Overview 1
Objectives 3
Outline 5

II. BACKGROUND 7

Clinical Overview of Targeted Radionuclide Therapy 8
Internal Dose Calculations 14
Use of Anthropomorphic Phantoms in Internal Dosimetry 27
Motivation for Patient-Specific Dosimetry 37
Advancements in Patient-Specific Internal Dosimetry 40

III. DEVELOPMENT AND VALIDATION OF VIDA: A VOXEL-BASED DOSIMETRY APPLICATION FOR TARGETED RADIONUCLIDE THERAPY 51

Introduction 51
Monte Carlo Simulation 52
3D Kinetics Processing 62
Validation 66
Summary 73

IV. PATIENT-SPECIFIC ANATOMICAL MODELING USING DEFORMABLE NURBS PHANTOMS 75

Introduction 75
Overview of NURBS 77
Development of the Phantom Morphus Software 81
Validation 97
Summary 108

V. APPLICATION TO PATIENT STUDIES 110

Introduction 110
Methods 111
Results 115
Discussion 119
Summary 124

VI. DISCUSSION AND CONCLUSIONS 125

Summary of Results 125
Future Work 128

Appendix

A. PHYSICAL PRINCIPLES OF INTERNAL DOSIMETRY 131

Radioactive Decay Mechanisms 131
Particle Interactions in Matter 134
Absorbed Dose 141
Radiobiological Considerations 142

B. FUNDAMENTALS OF NUCLEAR MEDICINE IMAGING 145

Single Photon Emission Computed Tomography (SPECT) 145
Positron Emission Tomography (PET) 150

C. OVERVIEW OF MONTE CARLO METHODS 156

D. MATERIAL TYPES AND INDENTIFIERS FOR ORGANS IN VIDA 161

E. SAMPLE INPUT FILE FOR VIDA MONTE CARLO SIMULATION 163

REFERENCES 164

LIST OF TABLES

Table Page

II.1: Common radionuclides and treatment indications. Mean energies are reported for beta decay emissions 9

II.2: SPECT reconstruction algorithms for quantitative imaging 42

III.1: Material definitions for VIDA MC simulation 56

III.2: Electromagnetic processes in VIDA MC simulation 58

III.3: Materials used in the simulation of dose factors for the reference adult male phantom. Tissue definitions taken from Oak Ridge National Lab Report ORNL/TM-8381/V1, Table A-1 (Cristy & Eckerman 1987) 69

III.4: Relative percent differences in VIDA and OLINDA/EXM sphere dose factors 70

IV.1: Description of patients used in deformable model validation 99

IV.2: Evaluation metrics for patient-specific deformable models 103

IV.3: Mean evaluation metrics for each organ 103

IV.4: Comparison of organ absorbed doses calculated from patient-specific NURBS models and manually segmented CT data expressed in relative percent differences 104

V.1: Administered tracer and therapy activity and whole body pharmacokinetics 112

V.2: Comparison of mean absorbed tumor doses between VIDA and DPM 116

V.3: Mean absorbed doses to organs and tumors from post-therapy dosimetry 118

C.1: List of organs and assigned material type in VIDA Monte Carlo simulation 161

LIST OF FIGURES

Figure Page

II.1: Radiolabeled anti-CD20 monoclonal antibody targets cancerous NHL B-cells.....12

II.2: Non-penetrating and penetrating radiation in human tissue. 17

II.3: Dose kernel convolution using both anatomical and functional image information to produce a dose map. The CT image on the left provides tissue density information. The center image represents the distribution of activity which is convolved with the dose kernel. The image on the right is the resulting dose distribution (Tsougos et al. 2010) ...24

II.4: Dose-volume histograms for metastatic thyroid carcinoma tumors treated with ^{131}I (Sgouros et al. 2004).....27

II.5: Schematic representation of the stylized Snyder-Fisher phantom (Snyder et al. 1978)....29

II.6: Pediatric phantom series developed by Cristy and Eckerman. This series models the anatomy of newborn, 1-year, 5-year, 10-year, 15-year, and adult patients (Cristy & Eckerman 1987) 30

II.7: 3D view of the internal organs of the VIP-Man voxel based model (Xu et al. 2000).....32

II.8: Boundary representation models constructed from NURBS for organ and body surface definition, (a) NCAT and (b) XCAT phantom.....36

III.1: VIDA procedure flow with key components and inputs 52

III.2: Schematic drawing of a nested parameterization in Geant4. Repetitions in each direction are assigned a copy number. Voxels in the geometry are identified by a unique combination of copy numbers representing the row, column and slice position 54

III.3: Step size control in Geant4 with *dRoverRange* and *finalRange* 60

III.4: Graphical user interface of the MATLAB-based exponential fitting tool in VIDA 64

III.5: 3D viewer in VIDA exponential fitting tool to evaluate integrated dose map and voxel fits 65

III.6: Anterior views of the RADAR adult male NURBS phantom 68

III.7: DF comparison between VIDA and OLINDA/EXM for unit density soft tissue spheres of different masses.....70

III.8: Self and cross organ dose factors for liver, spleen, and pancreas in the RADAR adult male phantom. Solid bars are reference values (Stabin et al. 2012) and outlined bars are

from VIDA. Percent differences are listed above each pair, defined as $100 \times (DF_{VIDA} - DF_{RADAR}) / DF_{RADAR}$ 71

IV.1: Schematic representation of knot vectors that divide the NURBS surface into piecewise segments. Surface degree of $p = 3$ and $q = 3$ with knot vectors given by $\mathbf{U} = (0, 0, 0, 0, u_1, u_2, 1, 1, 1, 1)$ and $\mathbf{V} = (0, 0, 0, 0, v_1, v_2, 1, 1, 1, 1)$. Note that the spacing is not uniform in each parametric direction 79

IV.2: Modification of NURBS surface by moving control points. (a) NURBS representation of a plane with controls points (*) aligned on the surface. (b) Surface with shaped altered by translating two of the center control points in the z-axis 80

IV.3: 3D and 2D views of the Phantom Morphus software main graphical user interface 83

IV.4: GUI of image view tools for CT image display 84

IV.5: GUI for NURBS phantom viewing options and selection of structures 84

IV.6: GUI of surface transformation tools 85

IV.7: Result of organ modification using affine transformation of the left kidney. The top panel shows the original position of left kidney. The bottom panel shows the organ after scaling, rotation and translation.The phantom kidney is shown as a yellow contour in the images 86

IV.8: Example iteration of point inversion algorithm. The cloud point (black dot) is projected onto the curvature circle (black curve) to update the surface parameters corresponding to the foot point. The red arrows indicate the tangent and normal vectors at the current surface point 89

IV.9: Eliminated Bézier patch. Closest surface points lay on the boundary curves 90

IV.10: Example of data point selection and results for surface fitting to a point cloud. Each pair of images represents one set of results. The left image in each pair shows the original phantom kidney contour along with the point cloud to fit. The right image in each pair shows the resulting contour of the fitted phantom kidney 93

IV.11: Overlap of the lungs at the base before deforming structures to match the patient (a) and after modification (b). The white area is the left diaphragm that is voxelized as body and replaced by other organs including the spleen (red), stomach and heart (pink) 95

IV.12: Example of fitting the body contour to the patient. The ROI contours are defined approximately every 20 slices in the axial view (top). The surface mask is created using a threshold range of CT intensities and interpolated in the longitudinal direction (lower left). The partial NURBS surface is fit to the mask (lower right) 97

IV.13: Example patient-specific NURBS model and reference manual segmentation for (b) male and (b) female patients. The opaque body contours and breasts are not shown. 102

V.1: Fused SPECT/CT images for (a) Patient 1 and (b) Patient 2 with matching 3D dose maps overlaid on CT for (c) Patient 1 and (d) Patient 2. Dose maps are displayed in Gy. 116

V.2: Patient anatomy defined by (a) manual segmentation and (b) deformable NURBS..... 117

V.3: Tumor DVHs from tracer and therapy scans for (a) Patient 1 and (b) Patient 2. The tumor volumes were taken from the first post-tracer scan..... 118

V.4 Overlay of high heart activity uptake in patient 1 on CT image 120

A.1: (a) Excitation of orbital electron due to inelastic collision with a charged particle. (b) Characteristic x-ray emission from relaxation of excited electron 136

A.2: Ionization of orbital electron and subsequent excitation by the δ-ray electron 136

A.3: Bremsstrahlung emission due to coulombic interaction between a free electron and the nucleus of an atom..... 137

A.4: Coherent scattering of photon from interaction with orbital electron 139

A.5: The photoelectric effect 140

A.6: Compton scattering of an incident photon..... 141

A.7: The linear-quadratic model of the radiation effect on biological tissue with α the number of logs of cell kill per Gy and β the number of logs of cell kill per Gy^2 143

B.1: SPECT camera and image acquisition..... 146

B.2: Non-uniform attenuation in SPECT 147

B.3: Compton scattering in SPECT. Scattered photons may be detected in the energy window of the photopeak causing decreased image contrast. Correction is made using the triple-energy-window method, shown by the shaded trapezoid 148

B.4: Geometric contribution to CDR. The spatial resolution of the camera decreases with increasing depth of the imaging plane 149

B.5: PET imaging acquisition and electronic collimation by coincidence event detection 151

B.6: Types of detection events in PET: (a) true, (b) scattered, and (c) random. The dotted lines indicate the assigned and incorrect LOR for scattered and random events 152

B.7: PET projection data formed from events collected in a single detector ring..... 155

C.1: Process of reducing photon interaction lengths during Monte Carlo simulation of particle interactions in matter 159

ABBREVIATIONS

Δ	Energy emitted per disintegration
Φ	Absorbed Fraction
2D	Two-Dimensional
3D	Three-Dimensional
3D-ID	3D Internal Dosimetry
3D-RD	3D Radiobiological Dosimetry
4D	Four-Dimensional
Ã	Cumulated Activity
AC	Attenuation Correction
BED	Biologically Effective Dose
BKG	Background
BREP	Boundary Representation
CDF	Cumulative Distribution Function
CDR	Collimator-Detector Response
CT	Computed Tomography
DF	Dose Factor
DICOM	Digital Imaging and Communications in Medicine
DNA	Deoxyribonucleic acid
DOTA	1,4,7,10-tetraazacyclododecane-1,4,7,10-tetraacetic acid
DPM	Dose Planning Method
DTPA	Diethylene Triamine Pentaacetic Acid

DVH	Dose-Volume Histogram
EDTMP	EthyleneDiamine TetraMethylene Phosphonic acid
EGS	Electron-Gamma Shower
ESSE	Effective Scatter Source Estimation
EUD	Equivalent Uniform Dose
FBP	Filtered Back Projection
FDA	Food and Drug Administration
FWHM	Full Width at Half Maximum
GEANT	Geometry and Tracking
GPS	General Particle Source
GSF	National Research Center for Environment and Health (German)
GUI	Graphical User Interface
HU	Hounsfield Unit
ICRP	International Commission on Radiological Protection
LOR	Line of Response
LQ	Linear-Quadratic
MABDOSE	Monoclonal Antibody Dosimetry
MC	Monte Carlo
MC-LDDMM	Multichannel Large Deformation Diffeomorphic Metric Mapping
MCNP	Monte Carlo N-Particle
mIBG	metaiodobenzylguanidine
MIRD	Medical Internal Radiation Dose
MLEM	Maximum Likelihood Expectation Maximization

MRI	Magnetic Resonance Imaging
MSC	Multiple Scattering
NaI	Sodium Iodide
NCAT	NURBS-based Cardiac Torso
NHL	Non-Hodgkin Lymphoma
NURBS	Non-Uniform Rational B-Splines
OLINDA/EXM	Organ Level Internal Dose Assessment/ Exponential Modeling
OSEM	Ordered Subsets Expectation Maximization
PDF	Probability Density Function
PDM	Point Distance Minimization
PENELOPE	Penetration and Energy Loss of Positrons and Electrons
PET	Positron Emission Tomography
PMF	Probability Mass Function
PMT	Photomultiplier Tube
PRRT	Peptide Receptor Radionuclide Therapy
PVC	Partial Volume Correction
RADAR	Radiation Dose Assessment Resource
RE	Relative Effectiveness
RIT	Radioimmunotherapy
RMDP	Royal Marsden Dosimetry Package
ROI	Region Of Interest
SAF	Specific Absorbed Fraction
SC	Scatter Correction

SIMIND	Simulation of Imaging In Nuclear Detectors
SIRT	Selective Internal Radionuclide Therapy
SPECT	Single Photon Emission Computed Tomography
TEW	Triple-Energy-Window
TOF	Time Of Flight
TRT	Targeted Radionuclide Therapy
VIDA	Voxel-based Internal Dosimetry Application
VIP-Man	Visible Photographic Man
VOI	Volume Of Interest
XCAT	Extended Cardiac-Torso

CHAPTER I

INTRODUCTION

Overview

The past decade has ushered in an era of personalized medicine with the growing ability to customize care and optimize patient response to therapy. In 2010, a New England Journal of Medicine Perspective shared a vision of "steering patients to the right drug at the right dose at the right time" (Hamburg & Collins 2010). Improved understanding of genetic and molecular characteristics of cancerous cells has opened the door to creating selective biological vehicles designed to bind specifically to malignant tissue. Often, these tissue-specific agents can be paired with radioactive elements to create powerful diagnostic and therapeutic tools. Cell-targeting carriers labeled with photon-emitting radionuclides enable disease diagnosis and localization with nuclear medicine imaging techniques. Likewise, tumor-targeting agents can concentrate cytotoxic radiation in diseased tissue through the emission of short-ranged charged particles.

The use of radiopharmaceuticals as a systemic treatment modality has a unique distinguishing feature compared to other methods of personalized treatment, such as chemotherapy, that target diseased tissue through molecular mechanisms. The capability of imaging radionuclides permits quantification of patient pharmacokinetics for use in treatment planning to optimize the delivered dose. This high level of individualized dosage differs greatly from chemotherapy that is administered based on body weight and a maximum tolerated dose determined in clinical trial. Thus, cancer treatment using targeted radionuclides offers two levels of personalized medicine. The "right drug" is achieved by selecting the appropriate

radiopharmaceutical based on the specificity of cancer cell biology and receptor expression. The "right dose" is administered by individualized treatment planning through the use of a tracer amount for pre-assessment of uptake and retention.

Despite the prospect for highly individualized therapy using targeted radionuclides, dosimetry is not routinely employed as a clinical tool to optimize patient treatment. Instead, most patients receive similar amounts of radioactivity based on the maximum activity to deliver sufficient dose to diseased tissue while avoiding toxicity in normal tissue determined in clinical trials. The conservative "fixed activity" approach to treatment results in only a small percentage of patients receiving optimal care and largely under-dosing the majority of those treated. This is in stark contrast compared to other radiation oncology therapies that routinely employ individualize treatment plans. For external beam therapy, the radiation energy is selected based on tumor depth for maximum dose deposition and the beam is contoured to specifically match the shape of the tumor. Furthermore, real-time patient imaging during treatment permits dynamic planning as tumor shape and position change.

The lack of an established, widely adopted treatment planning method in targeted radionuclide therapy is due, in part, to the complexity of the procedure and also because early attempts failed to demonstrate a relationship between delivered dose and patient outcome. However, recent developments offer improved quantification of pharmacokinetics and new approaches to modeling radiobiological response. These advances offer promise for patient-specific dosimetry and the ability to relate dose to important biological end points, namely tumor control and toxicity. Many efforts have been made towards making individualized treatment a clinical reality. These include the development of accurate techniques for activity quantification and applications capable of performing complex dose calculations by Monte Carlo (MC)

simulation and other voxel-level dose estimation methods. One facet of patient-specific dosimetry that requires attention is the ability to quickly and accurately define patient anatomy necessary for modeling tissue composition in MC simulations and calculating absorbed doses to organ and tumor volumes. The current methods include using a standard anthropomorphic phantom that may differ drastically from the actual patient morphology or the creation of a patient-specific model from imaging data through time-consuming manual and semi-automatic segmentation. A different approach to modeling patient anatomy that is both accurate and fast must be established in order for patient-specific dosimetry to be clinically efficient.

Objectives

The goal of the research described in this dissertation is to explore the use of deformable anthropomorphic phantoms as a way to produce patient-specific anatomical models for dose assessment in targeted radionuclide therapy. This research was motivated by the development of standard phantoms consisting of Non-Uniform Rational B-Splines (NURBS) surfaces (Segars et al. 2001, Segars et al. 2010). The phantom organs are easily transformed by manipulating the control points that define their shape to generate models with varying anatomy. This research project is of interest because the quick adaption of an existing body model to an individual patient, without having to perform time-consuming image-based manual segmentation of anatomical structures, allows patient-specific dosimetry to be completed in a time-frame more favorable with the clinical treatment schedule. It is our aim that the development of a real-time application to create patient models for organ and tumor identification in conjunction with 3D dose estimates through MC simulation will facilitate the effort to replace current "fixed activity" treatment protocols with personalized plans.

This work is divided into two separate parts. The first project focuses on the development and validation of a voxel-based Monte Carlo simulation application for dose calculation. Our objective is to construct a dosimetry code that is capable of modeling the decay scheme of any type of radionuclide in order to be widely-applicable to current and future therapies. The second part is to develop an application to create patient-specific 3D models from deformable NURBS phantoms. These models will serve as input to the dosimetry application to accurately define patient anatomy and designate tissue properties in the simulation. We will then test the effectiveness of this method by performing patient-specific dosimetry in clinical studies. The specific aims are defined as followed:

1. To develop and validate a 3D dosimetry application using the Geant4 Monte Carlo toolkit. Geant4 provides an easy and comprehensive method of modeling any radionuclide through the use of the built-in radioactive decay module. The toolkit is also very flexible for defining the simulation geometry and scoring energy transferred to tissue at the voxel level. The dosimetry application produces 3D dose distributions that show tumor dose non-uniformities and permit radiobiological modeling.

2. To develop a patient-specific deformable model application including a Graphical User Interface (GUI) to display the NURBS surfaces and patient Computed Tomography (CT) images for easy user manipulation. The deformable model application has the ability to perform many different manipulations of the NURBS surfaces that define the phantom body contour and internal organs. These methods include simple transformations such as translation, rotation, and scaling as well as more complex algorithms for vector field transforms and surface reshaping to fit a set of points. These algorithms provide the user with a robust toolkit for easily creating a patient-specific model using a standard phantom as a template.

3. To assess accuracy of patient models created by modification of a NURBS-based standard phantom by comparing them to manually segmented image data. The accuracy of the patient models is assessed using a variety of different metrics, including comparing total organ volumes, calculating a distance map between organs, and computing the percent volume overlap of a specific organ. The data used in this study represents patients of different sizes, genders, and ages, which provides a measure of the robustness and flexibility of the deformable models program.

4. To demonstrate the utility of the dosimetry and deformable models techniques through application to clinical studies. The use of data from patient studies will establish the clinical viability of our dosimetry application and serve as an additional validation of our 3D dose assessment by comparing results to an established dosimetry method.

Outline

The work of this dissertation is organized into five major chapters. Chapter 2 begins with an introduction to clinical treatment applications using open source radioactivity. The chapter continues with a discussion of the methodology of determining dose from internal emitters and the role of anthropomorphic phantoms in internal dosimetry. The chapter concludes with a summary of research findings that serve as motivation for performing patient-specific dosimetry for these patients and advancements made in the field.

Chapter 3 focuses on the creation and validation of the Voxel-based Internal Dosimetry Application (VIDA), a toolkit using MC simulation and a custom exponential fitting tool to perform patient-specific imaged-based dosimetry. The material in this chapter is an extension of an article, "VIDA: a voxel-based dosimetry method for targeted radionuclide therapy using Geant4", published in Cancer Biotherapy and Radiopharmaceuticals (Kost et al. 2015).

Chapter 4 summarizes the method for creating a patient-specific anatomical model based on a standard NURBS phantom. The introduction section includes background on NURBS surfaces and the advantages for using them as a primitive for realistic modeling of the human body. The chapter continues with a discussion the Phantom Morphus software application and its algorithms that deform the NURBS surfaces of a reference phantom to match patient anatomy from CT imaging. The chapter also contains a study using high-resolution CT imaging that investigated the accuracy of identifying volumes of interest from the individualized NURBS model compared to manual and semiautomatic segmentation methods and an analysis of the impact of using deformable models for 3D dose assessment with VIDA.

Chapter 5 describes a clinical application of patient-specific dosimetry using the methods defined in Chapters 3 and 4. Individualized dosimetry was performed for two non-Hodgkin lymphoma (NHL) patients treated with a ^{131}I-labeled monoclonal antibody using multiple hybrid Single Photon Emission Computed Tomography (SPECT)/CT scans. The chapter presents results of voxel-level doses using organ maps created from conventional segmentation methods and from a patient-specific NURBS model. The chapter also includes a comparison of the results with doses calculated with another 3D dosimetry code that serve as additional validation of VIDA.

Finally, Chapter 6 summarizes the results of the previous chapters and discusses the clinical value of using patient-specific NURBS phantoms for dose assessment and treatment planning for radionuclide therapy. This chapter also outlines future advancements that can be made to expand the method for deforming NURBS phantoms into individualized models and the additional steps required to release the created dosimetry application to the broader nuclear medicine community.

CHAPTER II

BACKGROUND

Patient-specific dosimetry involves determining the amount, rate and distribution of internal doses from ionizing radiation based on individual anatomy and biokinetics. Internal dose assessment is not performed using direct measurements, but instead on theoretical calculations dependent on a number of principles, including fundamental physical processes of radioactivity and particle interactions, the biological response to radiation, pharmacokinetics of treatment agents, nuclear medicine imaging techniques for the detection and treatment disease, and computational simulation of dose deposition in models of the human body.

This chapter is organized into five sections. The first section contains an overview of clinical aspects of radionuclide therapy. The following section provides a brief overview of the two main approaches to internal dosimetry, namely fixed-geometry and 3D imaged-based methods. The third section discusses the historical development of anthropomorphic phantoms. These phantoms define anatomical structures and their tissue compositions necessary for dose calculations. The remaining sections focus on the motivation for performing patient-specific dose calculations and a summary of research developments that make personalized dosimetry viable in the clinical setting. For readers unfamiliar with basic physical concepts relating to nuclear medicine and internal dosimetry such as radioactive decay, particle interactions and absorbed dose, a review is included in Appendix A. The methodology behind nuclear medicine imaging techniques, including SPECT and Positron Emission Tomography (PET), is summarized in Appendix B. A brief overview of MC methods is found in Appendix C.

Clinical Overview of Targeted Radionuclide Therapy

Targeted radionuclide therapy[1] (TRT) employs locally, regionally or generally administered unsealed radioactive sources to selectively deliver radiation to tumors or target organs. Successful treatment depends on the sufficient uptake and prolonged retention of the radiopharmaceutical in the target region while limiting the toxicity to normal tissue. This specificity is achieved by selecting appropriate radionuclides that emit short range electrons through beta decay. As a cancer treatment, TRT combines the advantage of target selectivity from external beam therapy and the benefit of whole body treatment similar to chemotherapy. The systemic nature of TRT makes it an attractive treatment choice by simultaneously targeting primary tumor sites and distant metastatic disease that may be undetectable by diagnostic imaging.

Historically, TRT has exploited the human body's natural tendency for concentrating specific elements in certain tissue, such as iodine uptake in the thyroid or phosphate and strontium accumulation in bone. Many efforts have focused on developing a so called "magic bullet" with a mechanism for specific binding to target tissue. Progress has been made in the form of radioimmunotherapy (RIT) by combining immunotherapeutic and radiation mechanisms to target cancer cells that express specific antigens. Peptide receptor radionuclide therapy (PRRT) aims to target tumor cells with bioengineered radiopeptides that bind to specific membrane receptors with high affinity. Selective internal radionuclide therapy (SIRT) employs radioactive microspheres that are selectively delivered to tumors in the liver via the hepatic

[1] The use of unsealed radioactive source in cancer treatment has historically been known by a variety of names including isotope treatment, targeted radionuclide therapy, radiopharmaceutical therapy, internal radionuclide therapy, and more recently, molecular radiotherapy. There may be some nuances in each of these names, e.g. molecular radiotherapy is used to describe treatment with radioactive agents that interact with molecular sites and receptors. However, the vast majority of literature in this field employs the term targeted radionuclide therapy. Hence, in this work, any treatment relating to unsealed radiopharmaceuticals will be referred to as such.

artery. Table II.1 summarizes common therapeutic radionuclides including their decay properties and treatment indications. Comprehensive reviews of TRT for cancer treatment can be found in the literature (e.g. Brans et al. 2007, Ersahin et al. 2011).

Table II.1: Common radionuclides and treatment indications. Mean energies are reported for beta decay emissions.

Radionuclide	Half Life	Key Emissions		Treatments
		γ (keV)	β- (MeV)	
^{131}I	8.02 d	365	0.192	Benign and malignant thyroid disorders B-cell non-Hodgkin lymphoma Neuroendocrine tumors
^{90}Y	64.1 h	—	0.934	B-cell non-Hodgkin lymphoma Neuroendocrine tumors Microspheres for liver metastases
^{111}In	2.80 d	171 245	—	Neuroendocrine tumors Imaging analogue for ^{90}Y
^{177}Lu	6.73 d	208	0.149	Neuroendocrine tumors
^{89}Sr	50.5 d	—	0.585	Bone metastases
^{153}Sm	46.5 h	103	0.640 0.710 0.810	Bone metastases
^{166}Ho	26.8 h	80.6	0.651 0.694	Multiple myeloma Microspheres for liver-related disease
^{188}Re	16.9 h	155	0.795	Microspheres for hepatocellular carcinoma, colorectal cancer and neuroendocrine tumors

Radioiodine Therapy

The first application of targeted radionuclide therapy began in the 1940's with the use of radioiodine (^{131}I) for the treatment of hyperthyroidism (Graves' disease) and malignant thyroid conditions (Frantz et al. 1944, Hertz & Roberts 1946). Radioactive iodine is a natural choice for treatment due to its tendency to concentrate in thyroid tissue, with minimal or no adverse effects

on normal tissue including radiosensitive red marrow. Radioiodine decays with both beta and gamma emissions. The primary beta emission has an approximate maximum range in tissue of 2 mm, concentrating large doses to the thyroid. The detectable photon provides a method for characterizing the activity uptake in diseased and normal tissue.

Neuroendocrine tumors such as neuroblastoma and phaeochromocytoma can also be treated with radioiodine. Neuroblastoma is extremely radiosensitive and external beam therapy provides good control of local disease; however dose constraints of total body irradiation limit its success for systemic treatment. Targeted therapy with radioiodinated metaiodobenzylguanidine (^{131}I-mIBG) exploits the active uptake pathway for noradrenaline expressed in tumors of neural crest origin (Meller 1997). ^{131}I-mIBG therapy is most effective in treating small metastases due to the limited penetration range of ^{131}I beta particles, and is mostly utilized as a secondary treatment for patients with metastatic disease that exhibit poor response to chemotherapy. Other studies (Mukherjee et al. 2001, Prvulovich et al. 1998) have shown that ^{131}I-mIBG also has potential to treat metastatic carcinoid tumors in patients with advanced disease.

Bone-Seeking Therapies

Bone-seeking radionuclides offer an alternative palliative treatment for painful bone metastases. Skeletal tissue is a common place for metastatic disease with the majority of cases linked to prostate or breast cancer (Ersahin et al. 2011). External beam radiotherapy has been successful in treating both localized tumor sites and widely disseminated disease using half or total body irradiation. However, this approach can be very toxic and TRT may be equally effective but better tolerated (Chatal & Hoefnagel 1999). The most frequently used radionuclides for metastatic bone disease are ^{89}Sr and ^{153}Sm. ^{89}Sr is a pure beta emitter and acts as calcium analogue with preferential uptake in the skeleton. Treatment with ^{153}Sm is administered as a

molecule linked to a calcium salt (EDTMP) that has an affinity for skeletal tissue exhibiting increased bone turnover (Bauman et al. 2005). A novel bone-targeted therapy using the alpha emitter ^{223}Ra has been approved to treat metastatic castration-resistant prostate cancer. ^{223}Ra dichloride mimics calcium in the body and binds to areas of increased bone turnover as found in metastases. Energetic alpha particles have a very short range in tissue (< 100 μm), resulting in high linear energy transfer and cytotoxic DNA double-strand breaks (Bruland et al. 2006). The short range of alpha particles also offers the advantage of reduced dose to bone marrow compared to beta particles emitted by ^{89}Sr and ^{153}Sm.

Bone-seeking radiopharmaceuticals can also be used to treat multiple myeloma as a preparative regimen to high-dose chemotherapy and peripheral blood stem cell transplantation (Breitz et al. 2006). Tetraphosphonate molecules radiolabeled with ^{166}Ho localize on bone surfaces. ^{166}Ho is primarily a beta emitter with maximum energy of 1.85 MeV corresponding to a pathlength of 8.7 mm in soft tissue and 3.8 mm in bone, concentrating radiation in the skeleton while sparing normal tissue. The short physical half live of ^{166}Ho (27 hours) permits delivery of high-dose chemotherapy and reinfusion of preserved peripheral blood stem cells within 6–10 days, offering an advantage over high-dose therapy with longer lived radionuclides such as ^{131}I or ^{90}Y (Breitz et al. 2006).

Radioimmunotherapy

RIT for B-cell NHL is an attractive treatment option because lymphoma cells are inherently sensitive to radiation. Moreover, approximately 90 percent of patients with follicular lymphoma present with disseminated disease and cannot be cured with external-beam radiotherapy to localized sites (Kaminski et al. 2005). Several radiolabeled monoclonal antibodies have been developed that selectively bind to CD20 antigen on the surface of normal and malignant B cells

(see Figure II.1). The CD20 antigen is an ideal target for immunotherapy of B-cell NHL because it is expressed in most cases of NHL and on normal B lymphocytes but not on stem cells, plasma cells, or nonhematopoietic tissues (Witzig et al. 2002). When labeled with ^{131}I (^{131}I-tositumomab, drug name Bexxar) or ^{90}Y (^{90}Y ibritumomab tiuxetan, drug name Zevalin) and administered systemically, the antibody can deliver cytotoxic doses of radiation to all sites of disseminated disease. ^{90}Y-labeled antibodies may provide better response when treating bulky, poorly vascularized tumors and tumors with heterogeneous antigen expression. ^{90}Y delivers higher beta energy radiation than ^{131}I (2.3 MeV vs. 0.6 MeV) and can penetrate soft tissue up to 5 mm compared to the 1 mm range of ^{131}I. Furthermore, as a nearly pure beta-emitter, ^{90}Y ibritumomab tiuxetan can be administered on an outpatient basis without the need for patient isolation due to radiation safety concerns (Witzig et al. 2002).

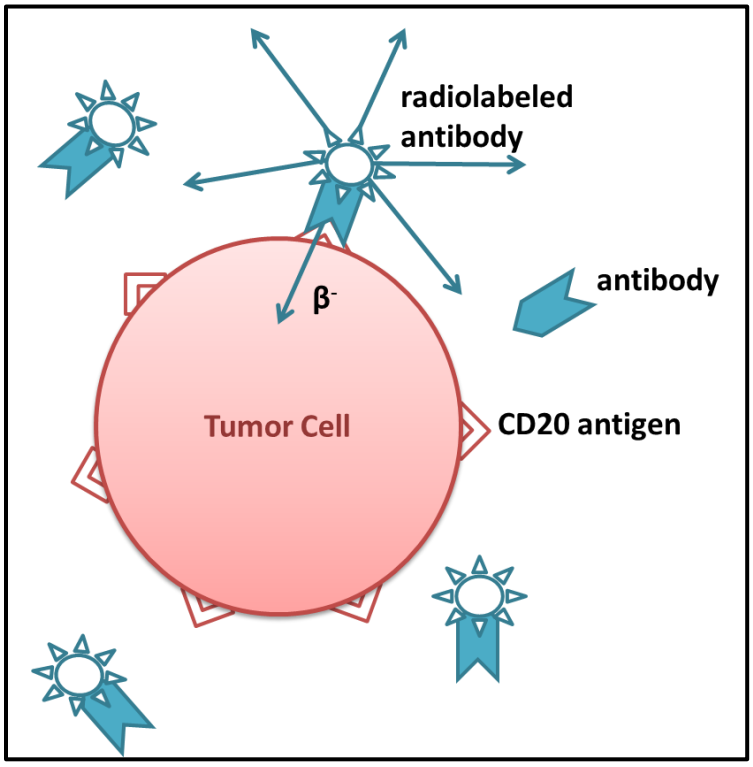

Figure II.1: Radiolabeled anti-CD20 monoclonal antibody targets cancerous NHL B-cells.

Peptide Receptor Radionuclide Therapy

PRRT has been investigated by several clinical trials as targeted treatment for neuroendocrine tumors. Therapy with radiopeptide exploits the overexpression of somatostatin receptors in a restricted number of tumor types. Somatostatin analogues were first labeled with ^{111}In in the form of ^{111}In-DTPA^{0}-octreotide and used mainly for tumor imaging. Initial treatment studies were performed by administering high activities of this radiopeptide with encouraging results (Valkema et al. 2002). However, ^{111}In is not an ideal radionuclide for PRRT because of its small particle range and therefore short tissue penetration (Kwekkeboom et al. 2003). Another radiolabeled somatostatin analogue ^{90}Y-DOTA^{0}-Tyr^{3}-octreotide was developed specifically for radiotherapy. As a pure beta emitter, ^{90}Y offers the advantage of delivering targeted dose to receptor-positive tissue while sparing normal tissue. However, the use of ^{90}Y must be paired with an imaging tracer counterpart for dosimetry calculations. The imaging tracer may not be chemically identical but must yield comparable radiopharmacokinetics and biodistribution. Recently a new analogue DOTA^{0}-Tyr^{3}-octreotate has been developed with a ninefold higher affinity for the somatostatin receptor subtype 2 as compared with DOTA^{0}-Tyr^{3}-octreotide (Kwekkeboom et al. 2003). Octreotate has been labeled with the beta and gamma-emitting radionuclide ^{177}Lu for therapy, offering several benefits over ^{111}In and ^{90}Y labeled radiopeptides. Studies indicated that the concentration of ^{177}Lu-octreotate was comparable to ^{111}In-octreotide for normal tissue but was up to fourfold higher for tumors. The increased tumor uptake obtained with ^{177}Lu-octreotate results in higher absorbed doses to malignant cells with similar doses to organs at risk for toxicity. ^{177}Lu-labeled peptides offer the advantage of having a lower maximum beta energy (0.49 MeV) and penetration range (2 mm) compared to ^{90}Y which may be important when targeting small tumors. ^{177}Lu also decays via gamma emission allowing for

activity quantification and dosimetry calculations using the therapeutic agent. A clinical investigation of the use of ^{177}Lu-DOTA^{0}-Tyr^{3}-octreotate for treatment of inoperable, somatostatin receptor positive gastro-entero-pancreatic neuroendocrine tumors is currently ongoing.

Selective Internal Radiation Therapy

Radiolabeled microspheres selectively treat primary or metastatic liver tumors through infusion into the hepatic artery. This treatment, known as SIRT, is based on observation that liver tumors larger than 2 cm in diameter receive more than 80% of their blood supply from the hepatic artery (Giammarile et al. 2011). Conversely, normal liver parenchyma receives the majority of its blood from the portal vein. The use of microspheres provides a highly specific treatment with upwards of 90% of the radioactivity localized in the liver.

^{90}Y embedded in resin or glass microspheres is the most popular radionuclide for SIRT. Fat droplets of iodized esters of poppy seed oil are also used by substituting stable iodine (^{127}I) with radioiodine. Microspheres containing ^{166}Ho and ^{188}Re are also used. With the exception of ^{90}Y, these radionuclides emit gamma photons that can be imaged, permitting patient-specific dose estimates from SPECT (Burrill et al. 2011, Shcherbinin et al. 2014).

Internal Dose Calculations

Internal dose assessment requires the determination of the total energy absorbed per unit mass of tissue for volumes of interest (i.e. whole organs, tumors, or voxels). The absorbed dose from internal sources is dependent on the type of particles emitted, their energies, and the tissues with which they interact. Absorbed dose calculations also require measurement of the uptake and retention of radiopharmaceuticals administered to the patient. Two approaches to internal dose calculations, fixed-geometry and 3D image-based dosimetry, are described in this section.

Fixed-Geometry Dosimetry

The conventional method for estimating absorbed dose from internal sources was standardized in the 1960's by the Medical Internal Radiation Dose (MIRD) committee of the Society of Nuclear Medicine (Loevinger & Berman 1976, Loevinger et al. 1988). The MIRD approach divides the dose calculation into the physical factors that determine the fractional energy of emitted particles absorbed by the tissue and the biodistribution of activity in the body. The method calculates the radiation dose to a target organ from radioactivity in one or more source organs based on absorbed fractions derived from a fixed geometry using a standard anatomical model.

Fixed geometry dosimetry using the MIRD schema separates the components of absorbed dose in a target volume into three distinct quantities. The dose is dependent on (1) the amount of activity as a function of time in the source organ, (2) the energy emitted per disintegration in the source organ and (3) the fraction of emitted energy absorbed by the target organ.

Cumulated Activity

Dose delivered by a source organ to a target organ is a function of the amount of activity in the source organ and the time the activity is present. The product of these values characterizes the number of total disintegrations in a source volume. This quantity, called cumulated activity ($\tilde{A}_s$), is determined by integrating the time-activity curve for a particular source organ (see equation II.1).

$$\tilde{A}_s = \int_0^\infty A_s(t)dt = A_0 \int_0^\infty f_s(t)dt \qquad \text{II.1}$$

The number of disintegrations in the source region depends on both the spatial and temporal distribution of the radionuclide within the body. Clinically, this value is obtained from a time-

sequence of nuclear medicine scans after injection of the radiopharmaceutical. These data are modeled as a sum of exponential functions (see equation II.2), with effective clearance rates dependent on the physical and biological half-lives of the source.

$$f_s(t) = f_1 e^{-(\lambda_1+\lambda_p)t} + f_2 e^{-(\lambda_2+\lambda_p)t} + \cdots + f_N e^{-(\lambda_N+\lambda_p)t} \quad \text{II.2}$$

The terms $f_1 \ldots f_N$ represent the fractional uptake of administered activity within the first to N^{th} components of the source region, $\lambda_1 \ldots \lambda_N$ represent the biological clearance rates for the corresponding N components and λ_p is the physical decay constant of the radioactive source (Stabin 2008b).

Energy Emitted Per Disintegration

The mean energy emitted per disintegration (Δ_i), also known as the equilibrium absorbed dose constant, is a product of both the average energy of the i^{th} emission and the relative frequency of the emission per decay. The equilibrium absorbed dose constant is a physical property of the radionuclide and may be obtained from standard dosimetry tables. For sources that have multiple emissions in their decay scheme, the total mean energy per transition must be calculated as the sum of the mean energies for all particles emitted. The product of the mean energy emitted per disintegration and the cumulated activity serves as an expression for the total energy emitted by the i^{th} emission for the time radioactivity is present in the source organ.

Absorbed Fraction

The final quantity in the MIRD schema for absorbed dose calculations is the absorbed fraction (ϕ_i). The absorbed fraction accounts for the emission type and particle energy as well as the geometrical factors relating the source to the target tissue. This value represents fraction of the total energy emitted in a source region that is absorbed in the target organ. The target receiving the energy can be the region emitting the radiation (self-dose) or other organs

throughout the body (cross-organ dose). For non-penetrating radiation (see Figure II.2a), most energy is deposited in the source resulting in an absorbed fraction near or equal to unity. In human tissue, beta particles, electrons and photons with energies below 20 keV are classified as 'non-penetrating' radiation (Loevinger et al. 1988). Radiation that deposits significant energy to organs other than the source is labeled as 'penetrating' and will have absorbed fractions between zero and one (see Figure II.2b). Because the absorbed fraction is dependent on the geometry relating the source region to the target region and the absorption properties of the tissues comprising the body, values are often obtained from MC calculations that model particle transport and energy deposition between source and target regions.

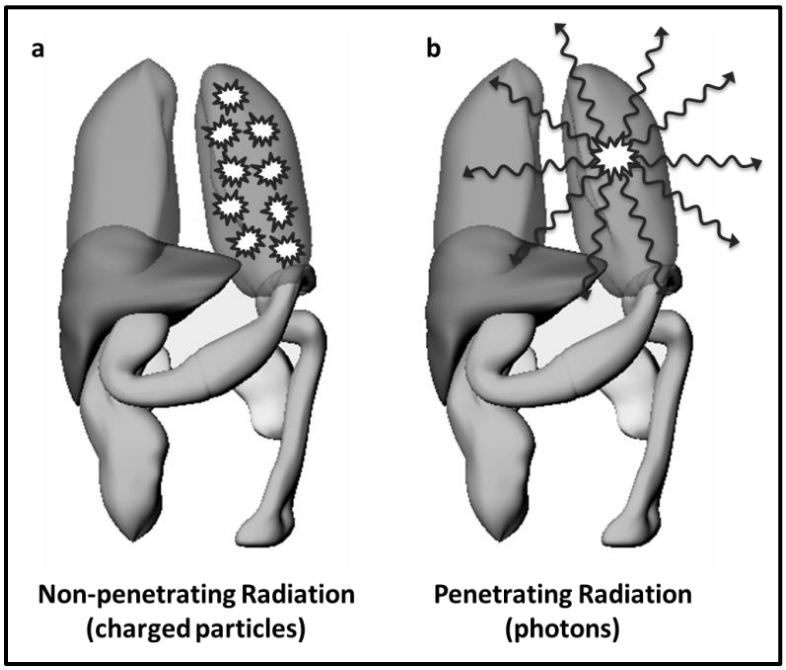

Figure II.2: Non-penetrating and penetrating radiation in human tissue.

Absorbed Dose

Expressing the total absorbed energy in terms of cumulated activity ($\tilde{A}_s$), energy emitted per disintegration (Δ_i), and absorbed fraction (ϕ_i) results in an equation describing the dose contribution to a target region from a source given by:

$$D_{T \rightarrow S} = \frac{k\tilde{A}_S \times \sum_i \Delta_i \cdot \phi_i}{m_T} \quad \text{II.3}$$

In equation II.3, m_T is the mass of the target region and k denotes a constant of proportionality. It can be reduced to a simple product of two values, the cumulated activity in a source region ($\tilde{A}_s$) and the absorbed dose to a target region per unit cumulated activity in the source, called the S-value (S) (see equation II.4).

$$D_{T \leftarrow S} = \tilde{A}_S \times S \quad \text{II.4}$$

By comparing equation II.3 to equation II.4, the S-value takes the following form:

$$S_{T \leftarrow S} = \frac{k \sum_i \Delta_i \cdot \phi_i}{m_T} \quad \text{II.5}$$

The total absorbed dose to the target (D_T) is simply the sum of the dose contributions to the target from all the different source regions (see equation II.6).

$$D_T = \sum_i \tilde{A}_{S_i} \times S_{T \leftarrow S_i} \quad \text{II.6}$$

The virtue of a fixed-geometry approach to dosimetry is that it reduces complex computations to a simple formula. S-values can be pre-calculated for a specific anatomic model and tabulated for each radionuclide, considerably reducing the required numerical work. The methodology is easily extended to clinical use in the form of software applications, requiring the user to only provide the cumulated activity for each source organ exhibiting uptake. The RAdiation Dose Assessment Resource (RADAR) Task Group of the Society of Nuclear Medicine has created large databases of S-values, calling them instead Dose Factors (DFs) (Stabin & Siegel 2003).

Three-Dimensional Image-based Dosimetry

For many years, dose calculations were limited by available computational resources and were generated using fixed geometry with standard phantoms. The approximations of applying a fixed geometry approach to patient dosimetry could result in errors up to 100% (Flux et al. 2006). While these uncertainties are acceptable for estimating stochastic risks from diagnostic nuclear medicine studies and radiation protection surveys, they are inadequate for therapeutic dosimetry when tumor control and toxicity are imperative. Several other limitations arise when fixed-geometry dosimetry is employed in TRT. Fixed-geometry dosimetry has no way to incorporate the spatial distribution of activity and only reports mean organ doses from uniform activity sources. Moreover, the use of pre-determined specific absorbed fractions (SAFs), the absorbed fraction scaled by the mass of the target volume, from standard phantoms lacks a suitable method for quantifying dose to and from tumor volumes, which is the primary goal of dosimetry for disease-targeting radioactive agents. Finally, radiobiological models, used to assess the biologic effects indicative of toxicity and tumor control from non-uniform absorbed doses, require knowledge of the spatial dose distribution to tumors and sensitive tissue. In the last few decades, significant efforts have been made towards patient-specific image-based approaches to dosimetry. Technological advancements in tomographic image, the availability of greater computational resources, and enhanced simulation capabilities have overcome many of the limitations to performing voxel-based 3D dosimetry.

Image-based dosimetry requires the following essential components. 3D anatomical images enable the definition of volumes of interest (organs and tumor) and provide tissue density information. Time-sequential voxel-based activity distributions describe the radiopharmaceutical kinetics permit the calculation of total absorbed dose. Lastly, a computational method for dose

calculation in the patient-specific model, such as MC simulation, is necessary. A detailed discussion of each of these elements is provided below.

Anatomical Model

The application of absorbed fractions to patient anatomy that greatly differs from a standard phantom causes a large amount of uncertainty in dose estimates using the MIRD schema. Incorporating a patient-specific anatomical model helps to reduce the error in the dose calculation. Patient anatomy provides accurate information about organ sizes and densities and permits tumor localization. Suitable image modalities for obtaining anatomical data include CT and magnetic resonance imaging (MRI), as both yield high contrast and high resolution 3D images. Image segmentation techniques, both automatic and manual, are used to define source and target region of interests (ROIs).

Radiopharmaceutical Kinetics

Personalized dose estimates require a quantitative measurement of the biodistribution of the radionuclide based on the uptake, retention and clearance rates of different organs. Once the source regions are identified from anatomic imaging, the distribution of the radiopharmaceutical in the body can be determined by sequential quantitative imaging methods such as SPECT or PET. At the present time, most therapeutic radionuclides do not emit positrons, making SPECT more applicable for activity quantification. However, there have been several studies investigating the use of PET-based imaging analogues in 3D dosimetry (Hobbs et al. 2009, Sgouros et al. 2011, Sgouros et al. 2004).

The selection of optimal time points for sampling is an important factor in activity quantification. The temporal sampling is related to the effective half-life of the radiopharmaceutical and applying inappropriate sampling points may have a significant effect on

the accuracy of the cumulated activity measurements. Insufficient sampling of tissue activity at times just after administration results in an overestimation of the area under the time-activity curve. If long-term retention is neglected from insufficient sampling at times long after administration, the cumulated activity will be underestimated (Siegel et al. 1999). Imaging after administering a therapeutic level of activity may be postponed due to the dead time of the camera. A short but finite amount of time is required to process a recorded event and proceeding events may be lost or incorrectly positioned during this time. At high levels of activity, these losses may be substantial, requiring either a delay of imaging, dead-time correction or both.

When the imaging tracer differs from the therapeutic one, it is necessary to correlate the behavior of the imaging and the therapeutic radiopharmaceutical. For chemically different imaging tracers, as is the case when using a gamma-emitting image surrogate to predict the therapeutic response from beta emitters such as ^{90}Y, it is assumed that the similar physical and biological half-lives of the two agents yield comparable *in vivo* pharmacokinetics and biodistributions (Brans et al. 2007). Half-life differences must be accounted for when determining the cumulated activity for the therapeutic agent by multiplying the measured activity at a given time point by the ratio between the decay constants for the therapeutic agent and imaging tracer.

The tomographic quality of SPECT permits modeling radiopharmaceutical kinetics for each voxel in the source region. Ideally, several SPECT studies are taken over time and registered to each other and the anatomical image (CT). The integration of voxel activities yields a 3D representation of cumulated activity. If multiple 3D images are unavailable, a hybrid planar/3D method of pharmacokinetic analysis is possible. The 3D cumulated activity is derived from a single SPECT scan by assuming a static spatial distribution for the region of interest and

applying average kinetics over the whole volume from the planar images. Values obtained based on average kinetics using the hybrid method may under- or over-estimate voxel-level doses by more than 50% compared to estimates made from time-sequenced 3D data (Sgouros et al. 2004).

It is important to note that the acquisition and reconstruction methods for diagnostic SPECT imaging may not be optimal for activity quantification for patient-specific 3D imaged-based dosimetry. A review article by Frey et al. (Frey) summarizes aspects of the imaging process that affect the reliability of quantitative measurements. Factors that degrade the image during acquisition include attenuation and scatter in the patient, increased septal penetration in the collimator due to higher energy gamma emissions associated with therapeutic radionuclide, and the intrinsic sensitivity of the detector to the emitted photon energies. Reconstruction of projection images using iterative statistical algorithms such as ordered-subsets expectation-maximization (OSEM) compensates for attenuation, scatter, collimator–detector response and partial volume effects, and generally yields more accurate quantitative data (He et al. 2005). In addition, quantitative methods require a conversion of image counts to a physical activity value. For planar imaging, this may be a simple counts-to-activity conversion factor that includes both the imaging system sensitivity as well as an approximate correction for source thickness (He & Frey 2006). However, voxel-level activity cannot be obtained from multiplication of a spatially invariant conversion factor without compensation for physical image degrading effects such as attenuation and scatter during reconstruction. The current guidelines for best practices in quantitative SPECT imaging for dosimetry are summarized in MIRD Pamphlet 23 (Dewaraja et al. 2012).

Absorbed Dose Calculations

Unlike absorbed dose estimates using the MIRD schema, image-based dosimetry does not rely on pre-determined SAFs from reference phantoms to relate the cumulated activity in a source to the dose deposition in a target. Therefore a method must be employed to model particle transport and energy deposition using patient anatomy and the biodistribution of the radionuclide. The spatial distribution of absorbed dose is determined by one of several methods including assuming complete, local absorption of short-range electrons, the application of voxel S values, dose-point kernel convolution, or direct calculation from MC simulation (Dewaraja et al. 2012).

The simplest approach is to assume local energy absorption of all electron and beta emissions within the same voxel as the decay. This method is fast as it only requires a rescaling of the activity distribution based on the energy spectrum and abundances for the radionuclide. It is best suited for pure-beta emitters (i.e. ^{90}Y) and may limit accuracy in the absorbed dose estimates for radionuclides with significant gamma emissions (i.e. ^{131}I) that deposit energy far from their source (Ljungberg & Sjögreen-Gleisner 2011).

Voxel level S value calculations provide another simple technique for determining spatially variant dose rates without having to perform patient-specific MC simulations. This method applies the MIRD schema to a target voxel using S values for nearby source voxels (see equation II.7) (Bolch et al. 1999).

$$D_{voxel\ T} = \sum_{i}^{N} \tilde{A}_{voxel\ S_i} \times S_{voxel\ T \leftarrow voxel\ S_i} \qquad \text{II.7}$$

Computation of voxel S values assumes the source and target voxels are contained within an infinite homogeneous medium. Therefore, voxel S value method offers accurate dosimetry for

anatomic regions of uniform density tissue but does not support tissue inhomogeneity. In addition, S values are specific to voxel dimensions. S values must be generated for each set of tissue type, voxel dimension, and photon or electron energy. Efforts have been made to tabulate S values for different voxel dimensions and radionuclides (Lanconelli et al. 2012) and create methods to rescale S values to arbitrary voxel sizes (Fernández et al. 2013) in order to make voxel S values a reliable and fast approach to dosimetric calculations.

The dose kernel convolution method (see Figure II.3) involves convolving the spatial activity distribution with a medium-specific radionuclide dose kernel. The dose kernel is defined as the absorbed dose per decay at a radial distance (r) from the source, assuming an infinite, homogeneous medium. Monte Carlo simulation is used to sample initial photon energies from the radionuclide decay scheme, generate the particle in a random direction, and score its energy deposition at a distance from the point source.

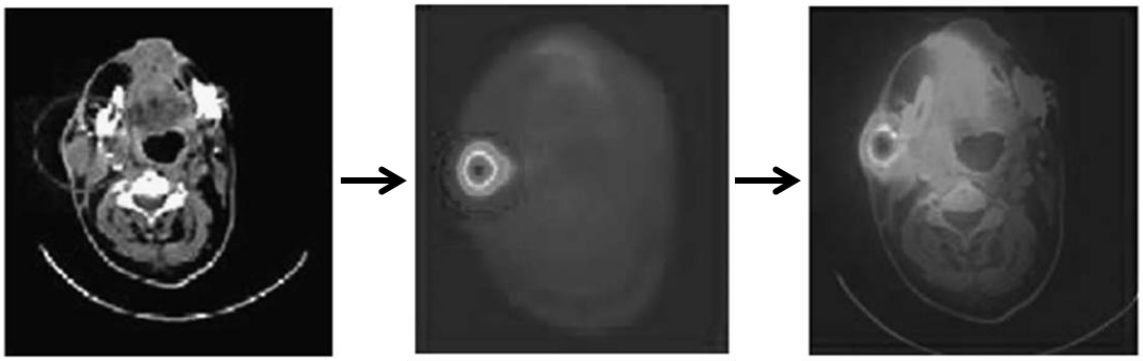

Figure II.3: Dose kernel convolution using both anatomical and functional image information to produce a dose map. The CT image on the left provides tissue density information. The center image represents the distribution of activity which is convolved with the dose kernel. The image on the right is the resulting dose distribution (Tsougos et al. 2010).

Dose kernels are simple to implement and calculation times are not prohibitively long especially if carried out in the Fourier domain. However, the dose kernel method has two major shortcomings. First, photon dose kernels do not model dose deposition due to electrons. This

limitation may be mitigated by assuming the electron dose is deposited within the voxel containing the activity. Second, modeling tissue inhomogeneity is difficult because dose kernels are generated assuming an infinite, homogeneous medium. Tissue density corrections can be applied using an energy loss factor derived from the specific material dose kernel such as water (soft tissue), bone or air (Loudos et al. 2009), but contain significant inherent uncertainties.

Direct patient-specific dose calculations are possible with the use of MC codes that simulate the transport of radiated particles and record energy deposits in complex geometries and for heterogeneous media. A personalized simulation is performed based on the patient geometry, radionuclide type, and activity concentration. Three-dimensional dose information is determined by discretizing the patient body into a voxelized phantom with a different material and activity assigned to each voxel. Common MC computer codes suited for internal dosimetry calculations include Geometry and Tracking (Geant4) (Agostinelli et al. 2003, Allison et al. 2006), Monte Carlo N-Particle (MCNP) (Sweezy et al. 2003) and Electron-Gamma Shower (EGS) (Hirayama et al. 2005). These codes have been developed over many years by teams of experts. Some have unique advantages (e.g. Geant4's visualization tools are superior to those provided with a standard MCNP or EGS installation), but all have undergone significant validation to provide reliable results for most particle energies and geometries.

Monte Carlo methods for dose calculations are known to be the most accurate; however there are some limitations. MC simulations are computationally rigorous, requiring considerable computing resources, and may exceed time constraints for clinical dosimetry. Furthermore, dose estimates from MC methods must be validated. The inherent flexibility in generic MC packages may cause large variability in results. Inconsistencies in particle transport and interaction models

and cross-section data and variances in patient anatomy and overall simulation geometry may contribute to these differences.

Many of the above techniques are applied to activity distributions at a moment in time after administration of the radionuclide. Therefore, the result is a 3D map of the dose *rate* at the time of image acquisition. In order to determine the total absorbed dose, 3D dose rate maps must be calculated using sequential SPECT or PET scans, co-registered and integrated voxel-by-voxel.

Analysis of 3D Absorbed Dose

Fixed-geometry dosimetry is limited to reporting mean doses to tumor and organs. In reality, tissues often manifest a heterogeneous distribution of activity, and thus dose during treatment. Results of 3D imaging-based calculations can be expressed as the mean or range of absorbed doses for a delineated volume or as a Dose-Volume Histogram (DVH) (see Figure II.4). DVHs are valuable for comparing organs doses from TRT to standard constraints used by conventional methods such as external beam therapy. Tumor isodose curves overlaid on anatomical images indicate the conformality of treatment. Performing these analyses from a pre-therapy tracer study allows optimization of the dose delivered to malignant tissue while avoiding possible toxicity during treatment.

Evidence indicates that deterministic biological effects including tumor response and normal tissue toxicity are not well predicted by the mean absorbed dose and may be significantly influenced by the spatial and temporal dependence of the dose rate (Flynn et al. 2003, O'Donoghue 1999). Radiobiological modeling of the 3D absorbed dose distribution may help to correlate patient outcome with delivered dose by taking into account these dependencies. Converting the spatially-variant dose distribution into the equivalent uniform dose (EUD) results in a single dose value that would yield a similar biological response similar. The EUD may

indicate the likelihood that the magnitude and spatial distribution of the absorbed dose is sufficient for tumor kill. Likewise, the biologically effective dose (BED) is an adjustment to the physical dose to yield the expected biological effect if it were delivered at a reference dose rate. The BED may provide a metric of how the temporal dependence of dose rate influences response and its relationship to tumor control and normal tissue toxicity.

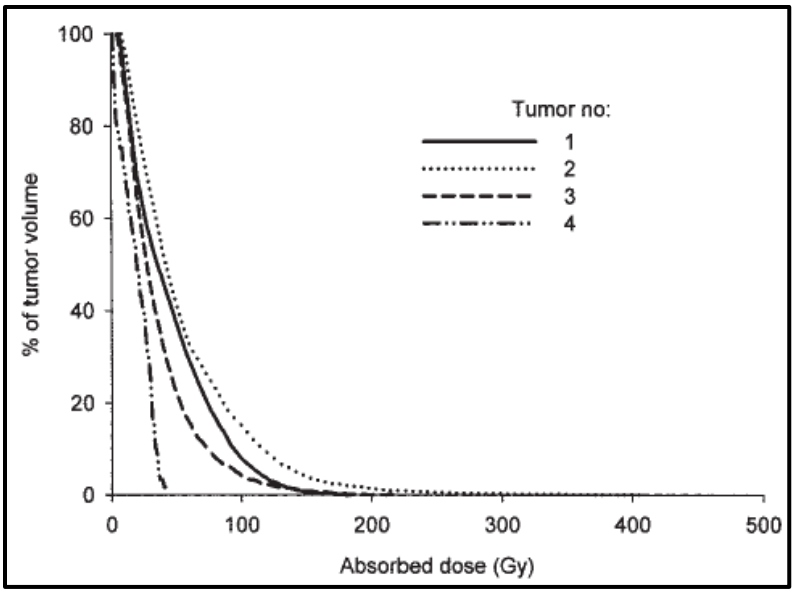

Figure II.4: Dose-volume histograms for metastatic thyroid carcinoma tumors treated with ^{131}I (Sgouros et al. 2004).

Use of Anthropomorphic Phantoms in Internal Dosimetry

The goal of internal dosimetry is to assess the biological response of healthy and diseased tissue from a spatially and temporally-dependent distribution of radioactivity in the body. Because it is impractical to measure dose from energy imparted to organs using *in vivo* physical detectors, dosimetry methods must rely on realistic computational phantoms to model human anatomy. Anatomical models contain body surface definition, organ geometry and volume, and tissue densities and compositions. Computational phantoms are classified into one of three main categories including stylized phantoms, voxel phantoms, and boundary representation phantoms.

This section summarizes each type of anthropomorphic phantom and some of their specific applications in internal dosimetry. A comprehensive review of anatomical models used in radiation dosimetry has been compiled previously (Xu & Eckerman 2010).

Stylized Computational Phantoms

The first type of model developed for dosimetry represented the human body using geometric shapes. These mathematical, or stylized, phantoms were based on the idea of a standard or "reference man", characterizing the average size and weight of adults in primarily Western populations. The use of simple mathematical equations for organ and body definition minimized computational time for simulation of particle interactions from internal emissions. The original stylized reference phantom, described below, was created for the specific purpose of calculating SAFs for internal dose assessment using the MIRD schema (Snyder et al. 1969). Other standard models were also developed to include pediatric ages (Cristy 1980), separate male and female adults (Kramer et al. 1982), and even pregnant females at different stages of gestation (Stabin et al. 1995).

Snyder-Fisher Phantom

In the 1960's, Snyder and Fisher developed the first stylized computational phantom for internal dose assessment (Snyder et al. 1969). The hermaphroditic phantom, shown in Figure II.5, consisted of a cylindrical base representing the combined torso, abdomen, and arms. An elliptical cylinder modeled the head and neck and legs were approximated as a truncated elliptical cone. The dimensions of the phantom were chosen to represent an average-sized man, modified later in accordance with the International Commission on Radiological Protection (ICRP) Reference Man (ICRP 1975). Originally, the entire phantom consisted of homogeneous soft tissue but was later updated to include the skeleton and lungs.

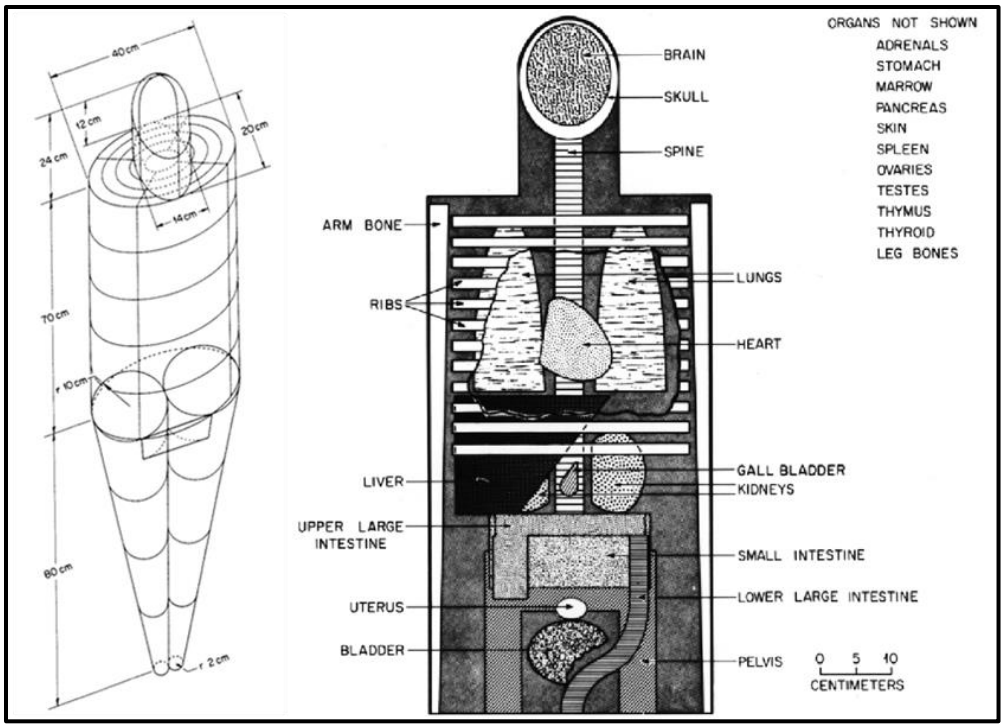

Figure II.5: Schematic representation of the stylized Snyder-Fisher phantom (Snyder et al. 1978).

The MIRD schema was first implemented using S values from the Snyder-Fisher phantom, with results published in MIRD Pamphlet No. 5 (Snyder et al. 1969) and a subsequent revision (Snyder et al. 1978). SAFs for 12 photon energies were estimated by MC simulation with uniform distribution in the source organ. Photon transport was tracked with the assumption of local energy deposition from photon-electron interactions.

Cristy-Eckerman "Family" Phantom Series

The limitations of scaling the reference adult Snyder-Fisher phantom for use in age-dependent applications motivated the creation of individualized pediatric phantoms. In the 1970's, Cristy and Eckerman developed a series of phantoms of adults and children ages newborn, 1, 5, 10 and 15 years (Cristy 1980). These phantoms were constructed in the same fashion as the existing Snyder-Fisher adult phantom to form a developmentally consistent family. The pediatric phantoms have relatively larger heads; their legs are relatively smaller, and

the trunk is relatively thicker than the adult models. The positioning of the organs varies from birth to adulthood based on age-dependent anatomical data (see Figure II.6). Reference phantom and organ masses were based on ICRP Publication 23 (ICRP 1975).

Additional improvements on the Snyder-Fisher phantom were made to the Cristy-Eckerman series. Female breast tissue was added to the 15-year-old phantom to represent an adult female. Breasts were also added to the hermaphroditic adult phantom to represent a larger than average female. Modifications to individual organs include an updated heart model and changes to the lungs to incorporate different sizes of the right and left lungs. Changes were made to the density and composition for soft tissue, lung, and skeletal tissues with different skeletal and soft tissue compositions for the newborn phantom.

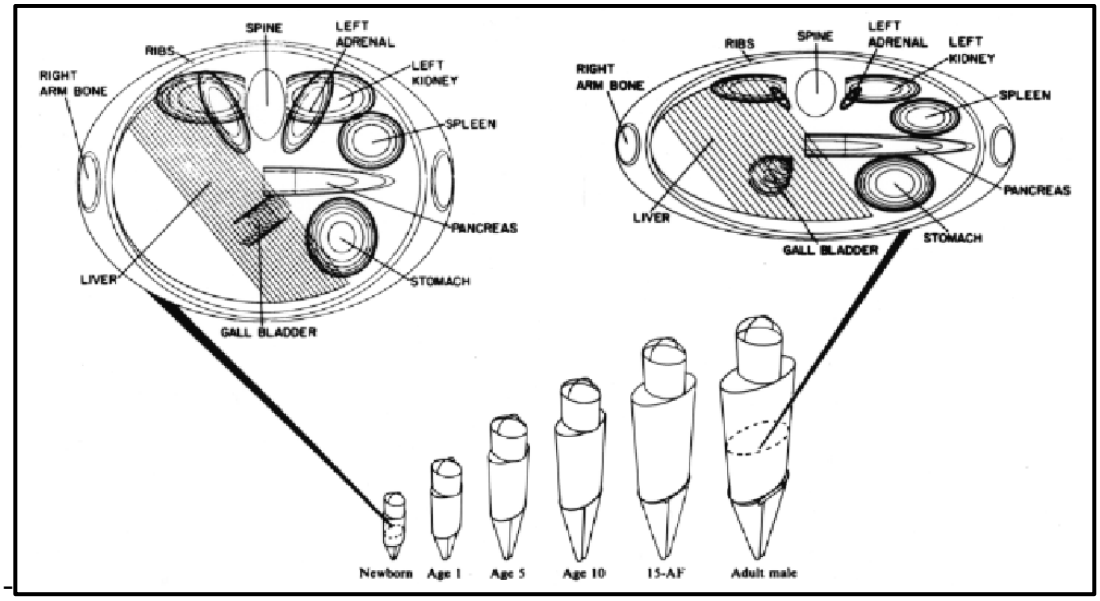

Figure II.6: Pediatric phantom series developed by Cristy and Eckerman. This series models the anatomy of newborn, 1-year, 5-year, 10-year, 15-year, and adult patients (Cristy & Eckerman 1987).

Specific absorbed fractions were calculated for these phantoms using MC simulations of photons similar to the method used by Snyder et al. (Cristy & Eckerman 1987). Cristy and

Eckerman also implemented a new technique to estimate the dose to red bone marrow in the vicinity of higher density bone where electronic equilibrium is not established. The MC transport code was adapted to determine the photon fluence in the skeletal volume from the target and calculate the dose to the active marrow using the linear attenuation coefficients for those photon energies.

Voxel Computational Phantoms

Stylized computational phantoms, although simple to implement in MC simulations, lack sufficient complexity to realistically model the details of the human body. Computer technology advancements in the 1980's, including the development of tomographic imaging (CT, MRI) to visualize internal anatomy, no longer restricted models of the human body to idealized geometric shapes. Instead, imaging data could be used to create a highly accurate representation of a human body comprised of small 3D volume elements (voxels). These phantoms, named voxel computational models, consist of an identification number for each voxel corresponding to a tissue type or organ and the specification of its density and elemental composition.

Many research groups have created voxel-based phantoms (e.g. Williams et al. 1986, Xu et al. 2000, Zankl et al. 1988, Zubal et al. 1994). These models consist of either the whole body or a partial body region such as head-torso or trunk only. Below is a summary of two of the more widely used types of voxel models, the VIP-Man and the GSF family of voxel phantoms.

<u>VIP-Man</u>

One of the first whole-body, high resolution voxel computational models, the Visible Photographic Man or VIP-Man (see Figure II.7), was developed at the Rensselaer Polytechnic Institute (Xu et al. 2000). The phantom was created using high resolution images (voxel size of 0.33 × 0.33 × 1 mm) of a 38-year-old male from the Visible Human Project that includes 3D

representations of the normal male and female human bodies from CT, MRI and color photography. Organs were identified on the color images and segmented using mainly manual techniques. Because the phantom is a representation of an actual person, the mass of the whole body and individual organs are not reference values. The VIP-Man is 103 kg, containing more than 30 kg of fat compared to the reference male of 70 kg.

Monte Carlo simulations of the VIP-Man voxel phantom were used to calculate SAF's for internal electron emitters (Chao & Xu 2001). Voxels were assigned tissue compositions and densities using recommended values in ICRP Publication 23 (ICRP 1975). These calculations were the first for charged particles and were significant for internal dosimetry. They permitted the investigation of subtle dose variations in anatomical structures due to incomplete energy absorption of the emitted electrons that were traditionally assumed to be non-penetrating. The results showed that over 20% of the energy can escape even large organ volumes at electron energies above 1 MeV.

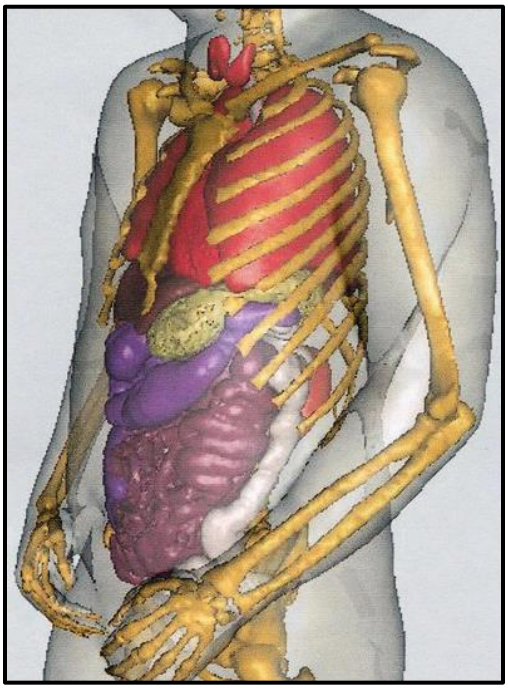

Figure II.7: 3D view of the internal organs of the VIP-Man voxel based model (Xu et al. 2000).

GSF Voxel Computational Phantom Family

A long-term research effort by the National Research Center for Environment and Health (GSF) in Neuherberg, Germany resulted in a series of voxel-based phantoms (Petoussi-Henss et al. 2002, Veit et al. 1989, Zankl et al. 1988, Zankl & Wittmann 2001). These phantoms were created using high-resolution CT images of individuals over a wide range of ages. The subjects included both adult males (Frank, Golem, Otoko) and females (Donna and Helga) of various physical builds and an infant and child (7 years).

Organ segmentation was accomplished using a variety of methods. For high contrast volumes such as the lung and skeleton, structures were defined based on specified ranges of Hounsfield Units (HUs) in the images. For most of the other organs, the mask created from image thresholds required additional processing to sharpen boundaries and reduce unwanted artifacts. In these cases, a number of image processing software packages were used to perform morphological operations (i.e. dilation or erosion based on shape parameters) and manual segmentation to clearly define the organ volumes. Due to the difficulty to visually delineate bone marrow on a CT image, the amount of red marrow was determined for each bone voxel using linear interpolation of the HU between values for pure cortical bone and pure red marrow. Tissue densities and compositions were compiled from multiple sources (Cristy 1980, Kramer et al. 1982).

The GSF voxel phantom series was used to determine the influence of body size and varying organ masses on absorbed doses (Petoussi-Henss et al. 2002). SAFs for internal photon emitters were calculated from MC simulation and compared to values from stylized MIRD-type phantoms. The SAFs to the voxel phantoms were found to be different (greater or lower) by factors of up to 1000 for low photon energies and small organs. Organ doses were comparable if

the masses were similar between phantoms, but deviated up to a factor of three in some cases. Changes in body morphology including organ size, shape and location contributed to these differences, confirming the limitations inherent in stylized geometrical phantoms.

Boundary Representation Phantoms

Voxel computational phantoms are anatomically realistic but, because they are created from patient images, represent an individual and not a reference man, woman or child. Moreover, voxel models may not correctly define the thickness of anatomical structures (i.e. skin or stomach and intestinal walls) because it is not possible to segment volumes smaller the resolution of the image. In the early 2000's, efforts began to create "deformable" human models from boundary representation (BREP) techniques, which can be manipulated to fit particular organ shapes and used to simulate time-dependent body motions. BREP modeling, initially created for computer-aided design, delineates solid volumes using a bounding surface consisting of a set of a connected faces (or patches). Most BREP phantoms consist of organs and body contours constructed from NURBS, a precise mathematical representation of a surface defined by a set of control points. These surfaces can be scaled and translated via affine transformations, making phantoms constructed from NURBS easily manipulated to replicate the size and shape of a specific patient.

Segars created the first BREP anthropomorphic phantom, the NURBS-based Cardiac Torso (NCAT) phantom, which incorporated dynamic modeling of the cardiac and respiratory cycles (Segars et al. 1999, Segars et al. 2001a, Segars et al. 2001). Since then, many other NURBS phantoms have been developed, including a series of adult and pediatric models at ICRP Publication 89 reference ages (Stabin et al. 2012), adult and pediatric phantoms of various ages,

sizes and statures (Johnson et al. 2009, Marine et al. 2010) and moderately and severely obese adults (Clark et al. 2010).

NCAT/XCAT Phantom

As mentioned above, the NCAT phantom (Segars et al. 2001) (see Figure II.8a) was the first BREP phantom developed. The phantom was constructed using manually-segmented CT images from the Visible Human Project. Segmented structures were converted to polygon meshes that were then fit with cubic NURBS surfaces. A time-dependent phantom was created to model the cardiac cycle using 4-dimensional (4D) tagged MRI data and respiratory motion based on respiratory-gated CT. The NCAT phantom consists of approximately 100 structures, limited to the torso region of the body. A later update, the extended cardiac-torso (XCAT) phantom (see Figure II.8b), contains thousands of anatomical structures including detailed modeling of the brain, nervous and vascular systems (Segars et al. 2010). The original XCAT phantoms were scaled to match body and organ volumes for a 50^{th} percentile adult male and female defined in ICRP Publication 89 (Valentin 2002). The XCAT series has been further expanded to include a number of models representing adults and pediatrics at various ages and sizes (Norris et al. 2014, Norris et al. 2014a, Segars et al. 2013).

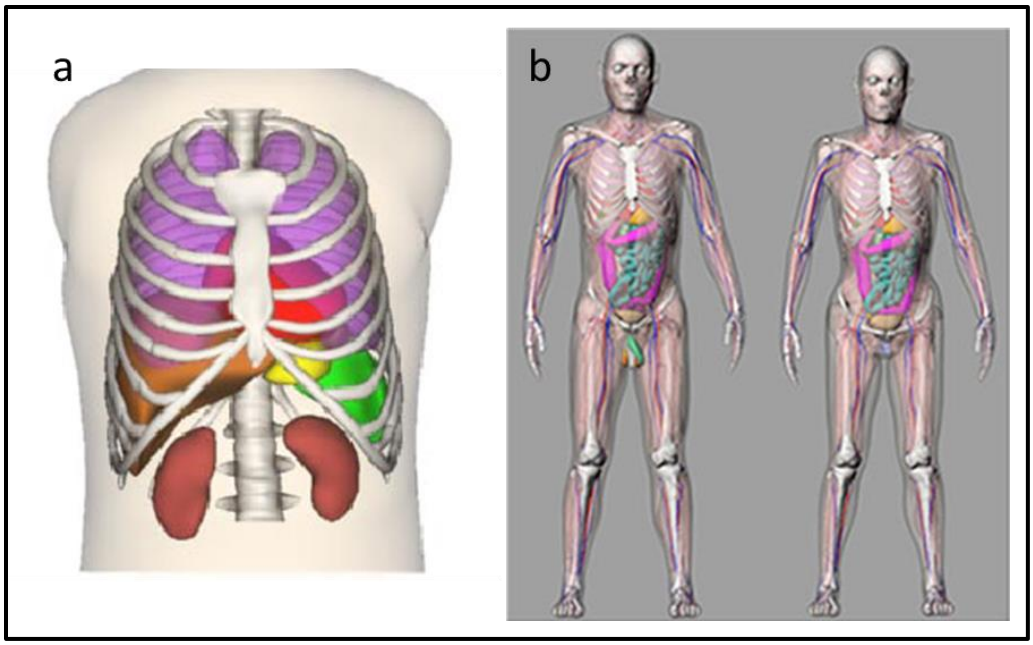

Figure II.8: Boundary representation models constructed from NURBS for organ and body surface definition, (a) NCAT and (b) XCAT phantom.

The NCAT/XCAT phantoms have been used in various applications related to internal dosimetry. Quantitative SPECT reconstruction methods have been evaluated using simulated projection data from the phantoms (He et al. 2009, He et al. 2005). The impact of 3D volume of interest definition on activity quantification using simulated planar and SPECT imaging was investigated by randomly moving control points to the nearest neighbor voxel to deform the original organ volumes (He & Frey 2010). In this same study, the effect of misregistration of sequential SPECT images on time-activity in organs was assessed by shifting the simulated images of the NCAT phantom by up to ± 1 voxel in each direction.

RADAR Reference Adult and Pediatric Phantom Series

In 2012, a new generation of NURBS-based reference phantoms was created at Vanderbilt University to update photon- and electron-SAFs originally derived from stylized models (Stabin et al. 2012). The phantom series includes male and female adults, pediatric ages for both sexes

and the pregnant woman. They were based on the original NCAT adult phantom (Segars et al. 2001) with modifications of the organ, body, and fetal masses using ICRP Publication 89 recommended values (ICRP 2002).

Changes in the SAFs in the NURBS reference phantoms were observed, but in most cases were small. Some cross-organ contributions from photons were found to increase due to organ proximity in the NURBS phantoms being much more realistic. Moreover, electron SAFs were explicitly modeled using MC simulation and non-negligible contributions were found for organs in direct contact (e.g. lung/liver and kidneys/adrenals) due to beta energy deposited in the first few millimeters of the boundary.

Motivation for Patient-Specific Dosimetry

In contrast with radiotherapy using external sources, patient-specific dose calculations for internal emitters are not routinely employed in clinical practice. Typical TRT treatments are based on administering a fixed activity to all patients. The aim is to deliver sufficient dose to the tumor while limiting toxicity to healthy tissue determined by the maximum tolerated dose in clinical trial. The fixed-activity approach is well established for treating thyroid disorders with radioactive iodine that has a large therapeutic window (the difference in dose levels between tumor and normal tissues). However this method is ill-suited for other forms of therapy including RIT and PRRT that have lower tumor-to-normal tissue dose ratios. If a fixed-activity is employed, patients are almost always given low amounts of the radionuclide in order to avoid harmful effects to normal tissue. Because there is significant variability in the biokinetics of radiopharmaceuticals in different patients and because the administered activity is based on the maximum tolerated dose of a patient population, only a small fraction of patients receive optimal

care. Although this method spares the normal tissue, it may result in incomplete tumor response and possible relapse (Stabin 2008c).

Pre-therapy dosimetry calculations using fixed-geometry methods can be performed to assess normal tissue toxicity; however, these measurements are not without significant errors. The largest uncertainties stem from applying phantom-related parameters such as SAFs and target organ mass to individuals that vary from the median represented by the model. Absorbed dose estimates based on standard phantoms may have uncertainties of a factor of two or greater. Patient-specific dosimetry can reduce the uncertainty in dose estimates to ±10-20% when data acquisition, analysis, and measurement of individual organ volumes are optimized (Stabin 2008c).

The most significant obstacle to employing patient-specific dose assessment for clinical treatment planning is the lack of data indicating a tumor dose-response correlation. Although studies attempting to correlate dose to treatment efficacy and patient survival have been conducted, the investigation of dose-effect relationships in TRT has never been the focus of a large multi-center clinical trial (Strigari et al. 2014). The limited number of statistically significant correlations between delivered dose and patient outcomes combined with the lack of a standardized method for performing dosimetry has made clinicians hesitant to adopt an individualized approach to treatment.

Despite the skepticism from the clinical community, significant research findings over the past decade indicate the necessity of patient-specific dosimetry, as summarized in a review article by Strigari et al. (Strigari). Studies indicate that better outcomes are achieved when dosimetry is performed for ^{131}I treatments (e.g. Flux et al. 2010, Lassmann et al. 2010). In the case of thyroid therapy with radioiodine, the use of activity-based criteria results in over-dosing

the majority of patients (Jönsson & Mattsson 2004). A similar comparison was performed for treatment of B-cell lymphoma using ^{131}I-tositumomab (Brans et al. 2007). It was determined that administering activity calculated per kilogram body weight resulted in 50% of patients being either over- or under-dosed by 10% or more and 16% of patients by 25% or more compared to therapeutic activity calculated on the basis of a diagnostic pre-therapy tracer study. Furthermore, Dewajara et al. (Dewaraja) investigated the relationship between tumor dose and patient outcomes in ^{131}I RIT for lymphoma with the inclusion of radiobiological modeling and found clear separation of progression-free survival curves at a threshold of 2 Gy. Dosimetric studies for PRRT have largely focused on renal toxicity as a limiting factor in treatment. Barone et al. (Barone) determined that nephrotoxicity was dose-dependent for neuroendocrine tumors treated with ^{90}Y-DOTATOC when including patient-specific parameters such as kidney volume and dose rate. Likewise, a comprehensive study of 200 patients treated with ^{177}Lu-octreotate using the standard protocol of 7.4 GBq per cycle concluded that over 50% of patients could tolerate more than the typical four cycles without reaching the kidney dose limit of 23 Gy (Sandström et al. 2013). These results indicate that determining both the administered activity per cycle and the number of cycles given to each patient is essential to tumor control and toxicity as the majority of patients receiving fixed activity amounts die from lack of control of their disease. Patient-specific dosimetry was performed in a Phase II clinical study of the safety and response of high-risk osteosarcoma tumors to high dose of ^{153}Sm-EDTMP as a follow up treatment to the standard low-dose administered activity (Senthamizhchelvan et al. 2012). It was determined from post-therapy dosimetry for both the low- and high-dose treatments that absorbed tumor doses over 21 Gy or EUD greater than 6 Gy led to a reduction of tumor size and stable disease.

In summary, evidence suggests that individualized dosimetry offers four major advantages over current fixed-activity treatments:

- The minimum effective and maximum tolerated absorbed doses are determined for each individual patient, which allow for optimized treatment and improved outcomes.
- Normal organ toxicity is predicted from pre-therapy dosimetry, preventing deleterious side-effects from treatment.
- 3D image-based dosimetry permits radiobiological modeling that accounts for varying dose rates and non-uniformity, which is suggested as an improved metric for determining tumor dose-response relationships.
- And lastly, dose-response results of different patients can be compared and correlated to outcome.

Advancements in Patient-Specific Internal Dosimetry

Over the years, great strides towards patient-specific dosimetry have been made. These developments aim to provide clinical techniques for optimized personal treatment planning and dose assessment in TRT. Efforts have focused on methods for quantitative imaging, simulation applications for dose calculations, and patient outcome prediction with radiobiological modeling and analysis of tumor dose-response. This section provides a brief summary of the research that has advanced the field of patient-specific dosimetry in TRT. The discussion is not an exhaustive review of all research found in the literature, but instead highlights major accomplishments.

Quantitative Imaging

The ability to accurately quantify 3D voxel activity at each imaging time point directly influences the reliability of dosimetry calculations for TRT. Research efforts have focused on the

development and validation of custom image reconstruction algorithms due to the lack of commercially available systems supporting quantitative SPECT. Other groups have investigated the use of PET imaging surrogates to estimate activity distributions for non-positron emitting therapeutic radionuclides. This section presents an overview of current capabilities for activity quantification and the results of recent studies aimed to evaluate their efficacy.

Table II.2 summarizes research studies on quantitative SPECT, including details about the reconstruction algorithm and validation methods. Most of these quantitative reconstruction methods employ OSEM algorithms that optimize using a different subset of the projections in each iterative update. Attenuation correction (AC) and compensation for the collimator-detector response (CDR) is performed by including attenuation factors and the depth-dependent CDR in the system model matrix. Image-degrading photons from Compton scattering are compensated using methods for scatter correction (SC) including triple-energy-window (TEW)-based scatter estimation and sophisticated models such as effective scatter source estimation (ESSE). In some cases, partial-volume correction (PVC) is applied to small volumes to recover count spill-out. Each method requires a camera sensitivity calibration factor that converts reconstructed counts to absolute activity derived from experimental measurement of known activity quantities.

Table II.2: SPECT reconstruction algorithms for quantitative imaging

Reference	Radionuc.	Reconstruction Method	Validation	Quantification Error
(Ljungberg et al. 2002)	^{131}I	OSEM, CDR, EESE SC, CT-based AC	Zubal voxel phantom, SIMIND-simulated projection images	9% (total phantom) 2-54% (most organs)
(Koral et al. 2005)	^{131}I	OSEM, CDR, CT-derived AC, energy window-based SC, PVC	Physical lung phantom with central 100 ml uniform sphere & no bkg.	5.2-7.3%
(Dewaraja et al. 2005)	^{131}I	OSEM, CDR, CT-based AC, TEW SC, no post-filtering	Zubal voxel phantom with added spherical tumor volumes, SIMIND-simulated projection images	<7% (organs and spheres 16-56 ml) 37% (7 ml sphere)
(He et al. 2005)	^{111}In	OSEM, CDR, CT-based AC, EESE SC, PVC	Physical torso phantom with uniform spheres, lung, heart, liver and bkg. Activity	2-12 % (8-23 ml spheres)
(He et al. 2009)			Voxelixed NCAT phantom population (7 total)	1-9% (organ averages)
(Shcherbinin et al. 2008)	^{111}In, ^{131}I	OSEM, CDR, CT-derived AC, analytic photon distribution SC	Physical thorax phantom with 32 ml uniform cylinders & no bkg.	3-5% (32 ml cylinders)
(Shcherbinin et al. 2012)	^{177}Lu		Physical phantom with 70 ml uniform cylinder & no bkg.	<2% (70 ml cylinder)
(Dewaraja et al. 2010a)	^{131}I	OSEM, CDR, CT-derived AC, energy window–based SC	Physical phantom with 4-95 ml uniform spheres & bkg. activity	<17% (8-95 ml spheres) 31% (4 ml sphere)
(Ljungberg & Sjögreen-Gleisner 2011)	^{111}In, ^{131}I, ^{177}Lu	OSEM, CDR, density AC, ESSE SC	Voxelized XCAT phantom with added spherical tumor volumes in liver, SIMIND-simulated projection images	<9% (spheres, no bkg.) <38% (18-61 ml spheres, liver bkg.)

In vivo evaluation of quantitative reconstruction algorithms is difficult and therefore quantitative accuracy is typically established from either experimental measurements using physical phantoms or image simulation studies. Physical phantom measurements represent the true imaging capabilities of the clinical system, but often have simplified geometries with spherical, uniform sources. Therefore, simulation of image acquisition using voxel-based anthropomorphic phantoms with known activity uptake provides a method to determine quantitative accuracy in patient geometries. The simulation application SIMIND (Simulation of IMaging In Nuclear Detectors) (Ljungberg & Strand 1989) was developed to model all aspects of a clinical SPECT camera and has been used to create simulated projection images for reconstruction algorithm evaluation.

There have been several studies designed to obtain quantitative activity from SPECT images reconstructed by commercial software. Pereira et al. (Pereira) performed phantom studies with ^{99m}Tc, ^{131}I and ^{111}In using different source activity concentrations in spheres or organ regions and variable background activities in the surrounding water. Images were reconstructed with CT-based attenuation and window-based scatter corrections using the OSEM algorithm on the clinical workstation. System calibration factors for each radionuclide were applied to yield quantitative activities in spherical sources ranging from 1.4 to 11.5 ml. Quantification errors were found to vary greatly with source volume and activity concentration as well as background activity level. For the largest sphere (11.5 ml) the errors ranged from 2–30% for ^{131}I and from 2–52% for ^{111}In. Another study aimed to quantify activity distributions from ^{177}Lu SPECT using a commercially available camera system and corresponding reconstruction software (Beauregard et al. 2011). Images were reconstructed using a proprietary OSEM algorithm allowing for both attenuation and window-based scatter correction with no filtering selected. In addition to

applying a system calibration factor to convert counts to activity, a dead time correction factor for a paralyzable system based on the observed wide-spectrum count rate was used to compensate for dead-time losses. This method was validated with a physical phantom consisting of uniform activity cylinders (175 and 2500 ml) with quantitative SPECT activity deviating from the calibrated activity between 4 and 10%.

Quantitative measurements of beta-emitting ^{90}Y have been accomplished with SPECT through the detection of bremsstrahlung radiation. SPECT imaging of ^{90}Y does not rely on a photopeak but instead detects the continuous bremsstrahlung energy spectrum with photons mostly below 50 keV. Image quality is typically poor due to the low camera sensitivity and non-linearity at this energy range combined with scatter and septal penetration of high energy photons. Despite the poor image quality, ^{90}Y bremsstrahlung SPECT has been shown to be an effective method for estimating tumor and liver doses and extrahepatic side effects from SIRT treatments with ^{90}Y microspheres (Ahmadzadehfar et al. 2012, Machac et al. 2007, Walrand et al. 2011).

Research efforts have also focused on using quantitative PET for patient-specific 3D dosimetry. Compared to SPECT, PET imaging is more sensitive by two orders of magnitude and is currently the most accurate clinical method for determining activity distributions. Quantification of PET is well established (Boellaard 2009, Pentlow et al. 1991) and image-degrading effects, such as random coincidences, dead time, and attenuation and scatter are routinely corrected before reconstruction in the clinical setting. However, because the majority of therapeutic radionuclides are not positron emitters, the use of PET imaging analogues of the same radioisotope is required for 3D dosimetry. Several groups have been successful employing high resolution, high sensitivity PET images for TRT dosimetry including using ^{124}I as an

analogue for ^{131}I treatment of thyroid cancer (Hobbs et al. 2009, Kolbert et al. 2007, Kolbert et al. 1997, Sgouros et al. 2004) and ^{86}Y PET for analysis of possible kidney toxicity from ^{90}Y-DOTA^{0}-Tyr^{3}-Octreotide in PRRT (Barone et al. 2005).

Recently, direct assessment of the biodistribution of ^{90}Y-labelled therapeutic agents using time-of-flight (TOF) PET has been performed for patients undergoing radioembolization of the liver with ^{90}Y microspheres (Lhommel et al. 2009). Although ^{90}Y decays via β^{+} emission, there is a minor branch to the 0+ excited state of ^{90}Zr that de-excites via electric monopole transition with internal electron–positron pair production at an abundance of 32 emissions per one million decays (Greenberg & Deutsch 1956). Despite low yield and high intrinsic background noise in the detector, successful ^{90}Y PET imaging of the liver has been achieved post-therapy with superior resolution and sensitivity compared to ^{90}Y bremsstrahlung SPECT (Kao et al. 2013, Kao et al. 2011).

Dosimetry Methods

One major obstacle for patient-specific dosimetry in TRT is the lack of clinical applications capable of performing the required complex dose calculations. In response, custom software has been developed that implements either fixed-geometry organ-level dose assessment using standard phantoms or direct absorbed fraction calculations by dose kernel convolution or MC simulation to determine the spatial dose distribution. This section summarizes available dosimetry applications and highlights their use in clinical studies on patient-specific dose estimation.

Since the MIRD methodology was developed, several groups have created applications for fixed-geometry dosimetry. MIRDOSE3 (Stabin 1996) and its successor Organ Level INternal Dose Assessment/EXponential Modeling (OLINDA/EXM) (Stabin et al. 2005) is the most

widely distributed fixed-geometry dosimetry software. The current application facilitates the implementation of equation II.6 and is capable of determining dose from over 1000 radionuclides with patient anatomy based on sex and age using the Cristy-Eckerman phantom series. The dose calculations are individualized by adjusting for variations between phantom and patient body and organ masses. OLINDA/EXM is also capable of simple tumor modeling in the form of self-dose to small unit density spheres of various sizes based on published absorbed fractions assuming uniform activity distribution (Stabin & Konijnenberg 2000). Another fixed-geometry dosimetry application MABDOSE (Monoclonal AntiBody DOSimEtry) (Johnson et al. 1999) was developed in an attempt to overcome the lack of contributing tumor dose from penetrating radiation from radionuclides with significant gamma emissions. MABDOSE allowed for user-defined tumor placement in a standard male or female phantom followed by MC simulation of radiation transport for penetrating radiations based on cumulated activities in each source region. Combining the energy deposition from the gamma rays with locally deposited energy from charged particle radiation produced updated S values for both tumor and normal organs.

Fixed geometry methods using standard phantoms are not optimal for dose assessment to individuals treated with TRT. Organ-level dosimetry applications based on standard phantoms including OLINDA/EXM and MABDOSE provide no information about the 3D distribution of dose in normal tissue and tumors as spheres with uniform activity. The lack of 3D dose information prevents radiobiological analysis, which may be necessary to fully assess toxicity and tumor control. In response to these limitations, many groups have developed 3D image-based dosimetry applications including 3D Internal Dosimetry (3D-ID) (Kolbert et al. 1997) upgraded to 3D Radiobiological Dosimetry (3D-RD) (Prideaux et al. 2007), SIMDOS (Tagesson et al. 1996), SCMS (Yoriyaz et al. 2001), the Royal Marsden Dosimetry Package (RMDP) (Guy

et al. 2003), VoxelDose (Gardin et al. 2003), OEDIPE (Chiavassa et al. 2005), an adapted version of Dose Planning Method (DPM) (Wilderman & Dewaraja 2007), and RAYDOSE (Marcatili et al. 2013). These custom dosimetry codes typically use MC simulation to determine voxel-level dose deposition; although some employ MIRD voxel S values (RMDP, VoxelDose) and 3D-ID initially performed dose kernel convolution.

3D-ID and its successor 3D-RD are the dosimetry codes with the most experience with clinical application. 3D-ID was used to perform patient-specific dosimetry for radioiodine therapy for thyroid cancer (Kolbert et al. 2007, Sgouros et al. 2004) and ^{131}I radiolabeled antibody treatment for NHL (Sgouros et al. 2003). Patient-specific dosimetry including radiobiological modeling with 3D-RD was implemented for thyroid cancer (Hobbs et al. 2009, Prideaux et al. 2007) and ^{153}Sm-EDTMP treatment for osteosarcoma (Senthamizhchelvan et al. 2012).

Significant progress for 3D imaged-based tumor dosimetry for ^{131}I RIT has been accomplished using DPM. Studies were performed to measure mean tumor dose that incorporated measured changes in tumor volume (Dewaraja et al. 2009, Howard et al. 2011). Radiobiological modeling to determine tumor EUD has also been applied using 3D dose distributions derived from DPM in conjunction with MATLAB-based routines (Dewaraja et al. 2014, Dewaraja et al. 2010).

Clinical investigations of personalized dosimetry in TRT have also been completed using custom voxel S value calculations. Doses for ablation of thyroid remnants using ^{131}I in differentiated thyroid cancer were determined using voxel S values generated from EGSnrc (Flux et al. 2010). Voxel based dosimetry in patients undergoing ^{90}Y RIT using Zevalin was evaluated with MATLAB-based voxel S value convolution from data computed using MCNP (D'Arienzo

et al. 2012). Patient-specific dose distributions from microspheres labeled with ^{188}Re for liver embolization (Shcherbinin et al. 2014) and ^{177}Lu PRRT for treatment of neuroendocrine tumors (Jackson et al. 2013) were produced through convolution of voxel S values from MC simulation using custom-based EGSnrc code DOSXYZnrc (Strigari et al. 2006).

Radiobiological Modeling and Tumor Dose-Response

The ultimate goal of patient-specific dosimetry is to correlate absorbed dose with tissue response. This may be tumor control and regression in the case of tumors or toxicity for radiosensitive organs. However, initial attempts to relate mean absorbed tumor doses to patient outcome were not successful, especially in the case of RIT (Sgouros et al. 2003). Studies indicate that deterministic biological effects including tumor response and normal tissue toxicity are not well predicted by the mean absorbed dose and may be significantly influenced by non-uniform doses and temporally changing dose rates (e.g. Barone et al. 2005, O'Donoghue 1999, Wessels et al. 2008). Radiobiological models that better predict desired treatment end points such as normal tissue complication probability and tumor control probability have been developed, but require knowledge of the 3D dose distribution to tissue (Sgouros & Hobbs 2014). Recent research has focused on identifying dosimetric and radiobiological factors that predict patient outcomes. These studies have mainly been retrospective in nature, evaluating tumor dose-response relationships post treatment.

The first patient-specific dosimetry application dedicated to radiobiological modeling 3D-RD incorporates the BED and EUD formalisms (Prideaux et al. 2007). Since its conception, 3D-RD has been applied to several clinical studies including radiobiological dosimetry for ^{131}I thyroid cancer (Hobbs et al. 2009, Hobbs et al. 2013, Sgouros et al. 2011), kidney toxicity from PRRT (Baechler et al. 2012), and osteosarcoma tumor dosimetry with ^{153}Sm-EDTMP

(Senthamizhchelvan 2012). The initial thyroid dosimetry studies were limited to a few patients to demonstrate clinical application of radiobiological methodology. However, Hobbs et al. (Hobbs) used 3D-RD to investigate salivary gland toxicity in ^{131}I treatment of thyroid cancer where toxicity is observed despite measured absorbed dose values below expected thresholds. Retrospective dosimetry for five patients using 3D-RD was performed on serial ^{124}I-PET images to determine if the BED of salivary glands may correlate better with toxicity and if using 3D voxel-based dosimetry may identify localized high absorbed dose values. Similarly, Baechler et al. (Baechler) proposed a treatment planning methodology using 3D-RD based on individualized dosimetry of kidneys with the goal of reducing renal toxicity in PRRT. The three most common radionuclides for PRRT (^{177}Lu, ^{90}Y, and ^{111}In) were evaluated and the approach centered on maximizing the administered activity, with optimal fractionation, to limit the absorbed dose or the BED to the renal cortex to published constraints. 3D-RD has also been used to assess tumor-dose response in a clinical trial for ^{153}Sm-EDTMP treatment of osteosarcoma (Senthamizhchelvan et al. 2012). A sample of 6 patients (19 tumors) who received both low and high amounts of administered activity were evaluated three months post-treatment with stable disease correlating with absorbed doses above 21 Gy (6 Gy EUD). Likewise statistical tests yielded a positive correlation between both mean tumor-absorbed dose and EUD, and percent tumor volume reduction.

Researchers at the University of Michigan developed a methodology to incorporate radiobiological modeling in patient-specific 3D dosimetry for NHL ^{131}I RIT. (Amro et al. 2010). This model was used to evaluate the treatment response of 20 patients that participated in a 3D patient-specific dosimetry study (Dewaraja et al. 2010). It was determined with statistical significance that a EUD of 200 cGy separated the responders (both partial and complete) from

those with stable disease. A regression analysis study of 39 ^{131}I RIT patients using this model assessed the relationship between patient outcomes and various dosimetric values (Dewaraja et al. 2014). Mean tumor-absorbed dose and equivalent biologic effect showed statistically significant correlation with progression free disease with clear separation of response curves when stratified by a mean tumor-absorbed dose of 200 cGy.

Other groups have also applied radiobiological modeling to RIT. Cicone et al. (Cicone) investigated dose non-uniformities in patients receiving ^{90}Y RIT for treatment of NHL and their correlation with tumor response. BED and EUD were derived from the 3D dose distributions and compared with patient outcome three months after treatment. Although the study sample (6 patients, 11 lesions) was not large enough to yield statistically significant results, complete response did correlate with larger tumor BED and EUD whereas patients who received low radiobiological doses exhibited stable or progressive disease. Hobbs et al. (Hobbs) developed a dosimetric method founded on radiobiologic modeling to optimize a combination therapy of both ^{131}I- tositumomab and ^{90}Y-ibritumomab tiuxetan for treatment of lymphoma. The treatment planning steps center around limiting toxicities to normal organs based BED values and optimizing response by maximizing the tumor BED within the established normal-organ constraints.

CHAPTER III

DEVELOPMENT AND VALIDATION OF VIDA: A VOXEL-BASED DOSIMETRY APPLICATION FOR TARGETED RADIONUCLIDE THERAPY

Introduction

This chapter describes the development of VIDA (Voxel-based Internal Dosimetry Application), a 3D image-based dosimetry technique using the Geant4 MC toolkit for voxel-by-voxel absorbed dose calculation. VIDA performs patient-specific dosimetry by coupling 3D anatomical data (CT) with functional images (SPECT or PET). VIDA was designed to perform particle transport based on the activity distribution at each time point, thus generating instantaneous dose rate maps. The total absorbed dose is determined by fitting the time-sequenced voxel dose rates to exponential functions and integrating over time. The application consists of two main components (see Figure III.1), the Geant4 simulation code to generate 3D maps of voxel-level absorbed energy and a custom exponential fitting tool developed in MATLAB. This chapter also includes a discussion of the methods used to validate the particle transport and energy deposition in the MC simulation. VIDA was validated under several conditions including dose to uniform activity spheres and organ dose factors from various sources in an anthropomorphic phantom. The content presented in this chapter is an extension of a paper by S. D. Kost, Y. K Dewaraja, R. G. Abramson and M. G. Stabin, "VIDA: A voxel-based dosimetry method for targeted radionuclide therapy using Geant4", © Mary Ann Liebert, Inc., reprinted with permission, from (Cancer Biotherapy and Radiopharmaceuticals, vol. 30, pp. 16-26, 2015) (Kost et al. 2015).

VIDA does not provide a method for quantitative SPECT image reconstruction. Quantitative estimation of activity from tomographic images requires attenuation and scatter correction as well as knowledge of the collimator-detector response that is highly system specific. Therefore, it is assumed that functional images used to model patient pharmacokinetics in VIDA are representative of quantitative activity. Moreover, VIDA does not contain a method to register time-sequence images. Images may be registered via external algorithms, such as the intensity-based registration routine in MATLAB. The incorporation of image registration in VIDA is an area for future development.

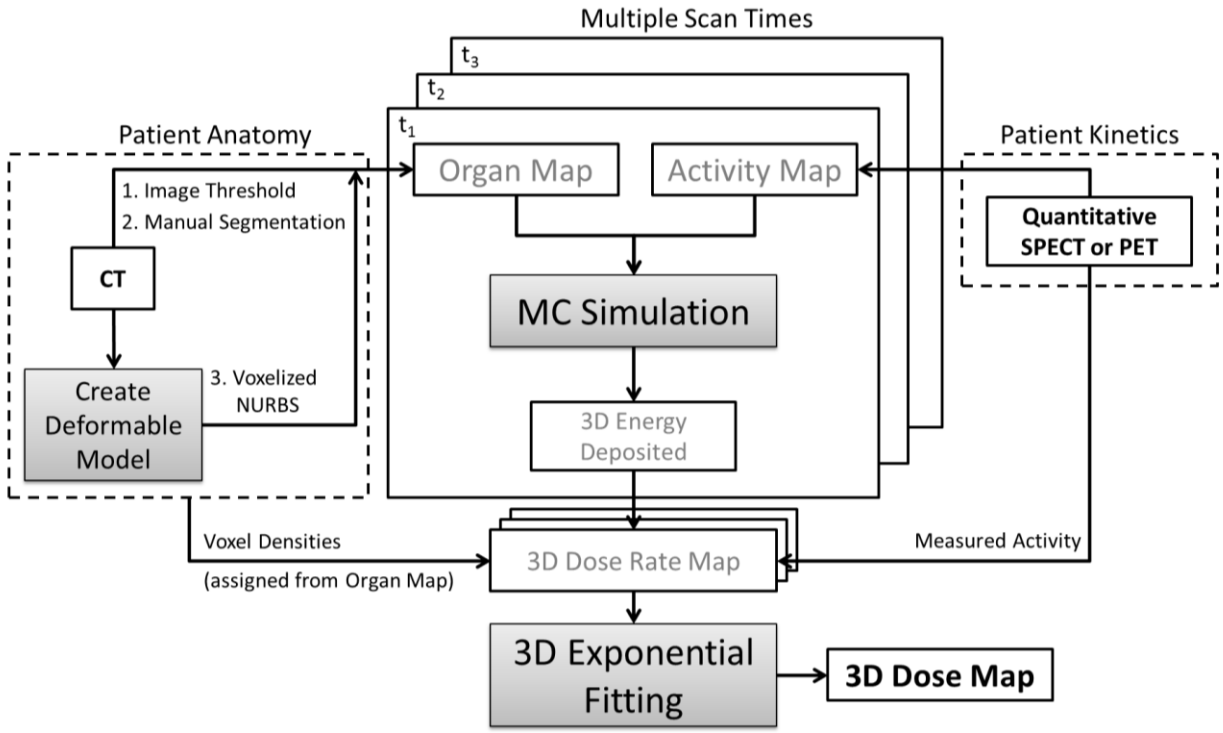

Figure III.1: VIDA procedure flow with key components and inputs.

Monte Carlo Simulation

Geant4 is an open source, integrated radiation transport package that simulates many different particles and their interactions based on a user-specified geometry. The toolkit provides

a comprehensive framework for all areas of MC simulation including geometry, tracking, physics models, and run and event management. In addition, Geant4 features a set of random number generators with different sampling algorithms and random distributions (i.e. exponential, Gaussian, Poisson). The toolkit was designed for a wide array of applications including particle physics, space engineering, and medical physics. Given the broad and flexible nature of the toolkit, the user is required to define specific characteristics of their simulation including the detector geometry, materials, particles, physics processes, and primary events generation.

The Geant4 framework is a suitable platform for performing MC simulation for TRT for several reasons. The built-in radioactive decay module allows for direct simulation of nearly any radionuclide without user specification of the decay spectra. Geant4 is supported by a large collaboration of researchers and includes the most accurate and up-to-date models for physical processes and particle interactions. Moreover, efforts relating to the validation of Geant4 have been extensively published and include relevant topics such as radioactive decay simulation (Hauf et al. 2013b) and electromagnetic processes of low energy electrons (Lechner et al. 2009).

VIDA was developed from an existing simulation that tracked photons and electrons uniformly distributed in a source organ using a standard anthropomorphic phantom (Stabin et al. 2012). The detector definition in this simulation was a parameterized (repeated) volume in each dimension to represent a voxelized reference phantom. Voxels were assigned a material type based on an integer identification number. The materials modeled included air, soft tissue, lung tissue and whole bone with the same density and compositions as the Cristy-Eckerman phantom series (Cristy & Eckerman 1987). Primary events consisted of either monoenergetic photons or electrons generated uniformly in the source organ that were tracked throughout the body. The energy deposited in the whole organ was tallied for each target region based on its identifier.

Using this existing simulation as a foundation, several updates and modifications were required for VIDA to function as a 3D patient-specific dosimetry code. First, the quantity and location of primary events must be based on the activity distribution in the patient. Second, primary events must be created with the correct particle types, energies, and abundances in the decay scheme of the radionuclide. Third, the energy deposited needed to be tallied at the voxel level, creating a 3D map of energy deposition that can be converted to a dose rate map. And lastly, the detector geometry and materials definitions required updating to include identification of multiple tumor volumes. Detailed descriptions of each part of the simulation are included in the following sections.

Detector Geometry and Materials

Detector definition in VIDA consists of a nested parameterized 3D volume, as shown in Figure III.2. The physical parameterized volume is defined to match the patient image array size and voxel dimensions. Each voxel is assigned a tissue type by pairing a specific material with the integer identifier for each organ contained within the 3D organ map (see appendix C).

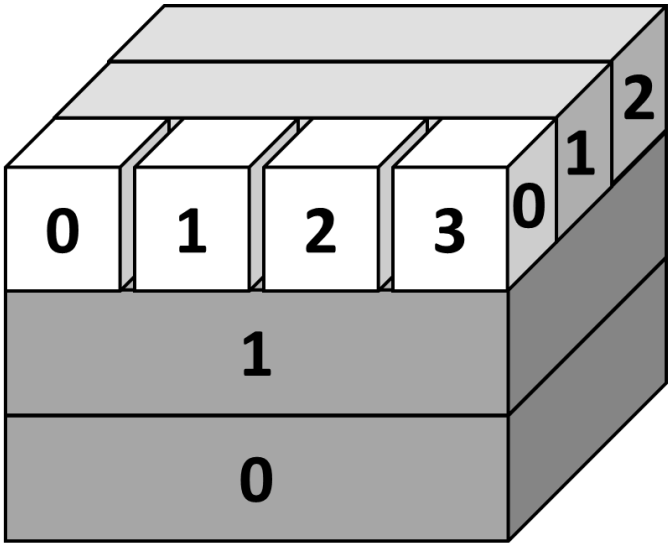

Figure III.2: Schematic drawing of a nested parameterization in Geant4. Repetitions in each direction are assigned a copy number. Voxels in the geometry are identified by a unique combination of copy numbers representing the row, column and slice position.

The material definitions in VIDA (Table III.1) include air for voxels surrounding the body contour and soft tissue, lung, cortical bone, red and yellow marrow, whole bone, and whole skull derived from data tabulated in International Commission on Radiation Units (ICRU) Publication 46 Appendix A (ICRU 1992). Patient geometry is represented by a 3D map of integer organ identification numbers instead assigning voxel density and composition directly from CT images, as done in the Geant4 DICOM application. This approach allows patient anatomy to be modeled by a NURBS-based deformable phantom that is digitized to a 3D organ map (see Chapter IV). Organ maps can also be created from conventional segmentation methods for delineation of organs of interest and tumor volumes on the patient CT. For multiple time points, segmentation of each CT can be time-consuming and tissue maps of relevant materials can be quickly created for simulation using density thresholds. VIDA includes several different material definitions for skeletal tissue. The NURBS models have cavities inside each bone so that cortical bone surfaces and marrow can be assigned specific materials. Similarly, if the skeleton is delineated by segmentation, hard bone and marrow voxels may be assigned using specific cortical bone thicknesses and marrow cellularity values. In the case of using density thresholds to generate an organ map, skeletal tissue should be assigned to whole bone. A flag in the data input file (see Appendix D) controls which materials are assigned to the skeleton during simulation.

Table III.1: Material definitions for VIDA MC simulation

Material	Density (g/cm^3)	Chemical Composition (% by mass)									
		H	C	N	O	Na	P	S	Cl	K	Other
Air	1.21×10^{-3}		0.01	75.5	23.2						1.3 (Ar)
Water	1.00	11.1			88.9						
Soft Tissue*	1.03	10.5	25.6	2.7	60.2	0.1	0.2	0.3	0.2	0.2	
Lung Tissue†	0.26	10.3	10.5	3.1	74.9	0.2	0.2	0.3	0.3	0.2	
Adipose&	0.95	11.4	59.8	0.7	27.8	0.1		0.1	0.1		
Mammary Tissue‡	1.06	10.2	15.8	3.7	69.8	0.1	0.1	0.2	0.1		
Whole Bone§	1.35	6.5	28.6	3.6	41.7	0.1	5.9	0.2	0.1	0.1	0.1(Mg) 13.2 (Ca) 0.1 (Fe)
Whole Skull‖	1.65	4.8	20.5	4.1	43.5	0.1	8.4	0.3			0.2 (Mg) 18.1 (Ca)
Cortical Bone#	1.92	3.4	15.5	4.2	43.5	0.1	10.3	0.3			0.2 (Mg) 22.5 (Ca)
Red Marrow	1.03	10.5	41.4	3.4	43.9		0.1	0.2	0.2	0.2	0.1 (Fe)
Yellow Marrow	0.98	11.5	64.4	0.7	23.1	0.1		0.1	0.1		

*'average soft tissue, male'
†'lung, adult healthy, inflated'
&'adipose tissue, adult #3'
‡'breast-mammary gland adult #3'
§composite material defined using average density and elemental compositions of adult whole bones (excluding cranium and mandible)
‖composite material defined using average density and elemental compositions of adult whole cranium and mandible
#'skeleton-cortical bone, adult'

Particles and Physics Processes

Geant4 has the capability to model a wide range of particles and the physics processes governing their interactions with matter. Each particle type is associated with a unique set of processes. The user can choose to apply only those processes that are relevant to their simulation and register them via the process manager. In the case of TRT, electromagnetic interactions for all decay products must be considered. The particle types registered to the simulation were

defined by the particle constructor of the decay physics class and include leptons, bosons, mesons, baryons and ions created in radioactive decay. Physics processes in VIDA include decay of unstable particles, radioactive decay of unstable isotopes, and standard electromagnetic processes such as photoelectric absorption, Compton scattering, gamma conversion, coulomb scattering, and bremsstrahlung.

Geant4 also contains several options for modeling electromagnetic physics processes. The standard electromagnetic physics package is optimized for electron and photon interactions at high energies between 1 keV and 100 TeV. At low energies, atomic shell structure plays a significant role in particle interactions and additional electromagnetic physics processes for photons, electrons, hadrons, and ions have been implemented in Geant4 in order to extend the validity for these energies. Low energy models available in Geant4 include the Livermore and PENELOPE packages that make direct use of shell cross section data, providing reliable results for energies as low as 250 eV. This is in contrast with the standard electromagnetic processes that rely on parameterizations of these data.

The physics models implemented in VIDA (Table III.2) are a modified version of the standard electromagnetic package. The low energy Livermore and PENELOPE models available for the version of Geant4 used in this work (Geant4 9.4) contain older interaction cross-section data and the Geant4 Low Energy Electromagnetic Physics Working Group advised against their use. Moreover, the standard package available for Geant4 9.4 was updated to be a coherent approach to the modelling of all electromagnetic interactions over both low and high energies (Ivanchenko et al. 2011). Options were selected to increase accuracy when tracking electrons, hadrons, and ions at low energies. Detailed explanations for these options follow below.

Table III.2: Electromagnetic processes in VIDA MC simulation.

Particle Type	EM Process	Model
Gamma	Photoelectric Effect	*(G4PEEffectFluoModel)*
	Compton Scattering	Klein-Nishina *(G4KleinNishinaModel)*
	Gamma Conversion	Bethe-Heitler *(G4BetheHeitlerModel)*
e^- and e^+	Multiple Scattering	L. Urban *(G4UrbanMscModel95)*
	Ionization	Möller (e^-e^-) Bhabha (e^+e^-) *(G4MollerBhabhaModel)*
	Bremsstrahlung	*(G4eBremsstrahlungModel)*
	$e^+ e^-$ Annihilation (e^+ only)	*(G4eplusAnnihilation)*

VIDA includes a Compton scattering model that allows atomic de-excitation of the resulting ionized atom. The standard model for Compton scattering in Geant4 assumes the energy of the recoil electron is large compared to the binding energy and ignores the binding energy when determining the kinetic energy of the electron. This assumption becomes invalid in the low energy realm. The Compton scattering model used in VIDA contains Doppler broadening due to the non-negligible influence of atomic shell effects at low interaction energies that may result in interactions with non-valance electrons producing atomic shell vacancies.

Atomic relaxation processes induced by ionization events that leave the atom in an excited state are activated in VIDA. These processes include fluorescence and Auger electron emission and make use of radiative and non-radiative transition probabilities for each sub-shell of each element. Characteristic x-rays and Auger electrons are produced above the same threshold energy as secondary electrons and bremsstrahlung gammas, defined in the simulation as a production cut range (set to 1 mm for electrons, positrons, and gamma rays).

Many interaction parameters including the mean rate of energy loss below the secondary particle production cut, the total cross section per atom for the ejection of a secondary of energy

greater than the production cut and, given multiple processes providing energy loss for a given particle, the total continuous part of the energy loss are pre-calculated during run initialization and stored by Geant4 in tables for use in the simulation. By default, the standard electromagnetic package generates these data across the energy interval from 100 eV to 10 TeV divided into 84 bins. In order to increase the sampling across the range of energies encountered in TRT dosimetry, the energy interval in VIDA was set from 10 eV to 50 MeV divided into 220 bins.

One of the most critical parameters in MC simulation is the step size limit. The simulation must balance computational efficiency while also ensuring the step size is small enough that all relevant interaction cross sections remain approximately constant during the step (an assumption required to randomly sample the distance to interaction for each physics process). Continuous energy loss imposes an additional limit on the step size due to the energy dependence of interaction cross sections. Typically, tracking precision can be preserved while not compromising execution performance by limiting the step-size to no more than 20% of the stopping range. At low kinetic energies (i.e. less than 1 MeV), this limit results in step sizes that are too short. Geant4 imposes a lower limit on the step size, controlling the step function with two parameters (see Figure III.3). At high energy, the step is limited by the ratio of step size to stopping range (*dRoverRange* = 0.20) As the particle interacts and loses kinetic energy, the step size decreases gradually until it becomes lower than a specified cut off (*finalRange*). Below this range, the remaining distanced traveled is completed in a final step. A large portion of the energy imparted to tissue in TRT comes from continuous energy loss from charged particles and the parameter *finalRange* in VIDA was reduced from the default of 1.0 mm to 0.1 mm for electrons and positrons to ensure accurate dose deposition.

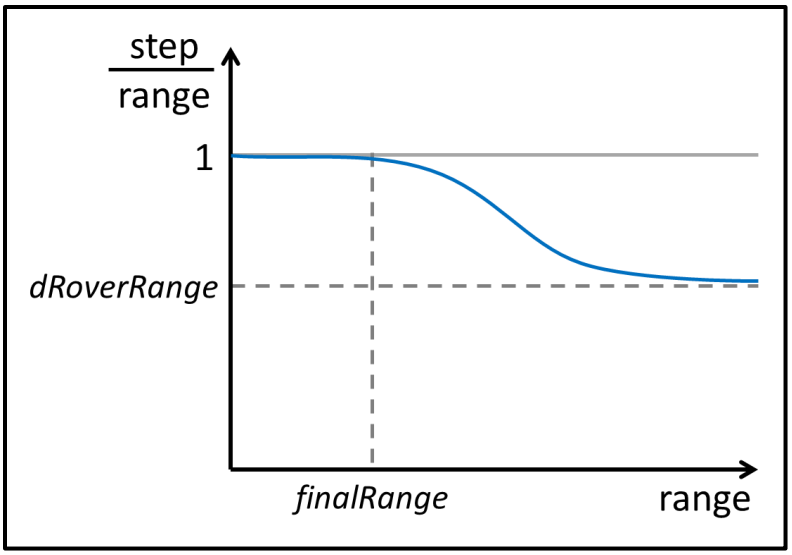

Figure III.3: Step size control in Geant4 with *dRoverRange* and *finalRange*.

The multiple scattering (MSC) algorithm for charged particles accounts for changes in the geometrical step length due to scatterings along the step. The MSC models in Genat4 limit the step size based on three parameters, two of which may be modified by the user (Ivanchenko et al. 2010). The step size limit (L) for MSC is determined by computing the minimum of the following values:

$$L = \min\{F_R \cdot \max(R, \lambda), F_S \cdot s, D/F_G\} \qquad \text{III.1}$$

The range factor (F_R) scales the maximum range computed based on the particle energy and inverse interaction cross sections (λ) for all possible interactions. If F_R is decreased, the limit on step size decreases and the simulation will perform more steps. The distance to a geometrical boundary (D) is weighted by the geometry factor (F_G) to insure a minimal number of simulation steps within each volume. An additional safety factor (F_s), fixed at 0.3, weights the straight distance between the start and end point of the step (s). The default values for MSC range factors (*"fUseSafety"*) are 0.04 for F_R, and F_G is ignored. The low energy electromagnetic processes constructor used in the VIDA employs the strictest variant for MSC step sizes ("*fUseDistanceToBoundary*") setting F_R to 0.04 and F_G to 2.5.

Primary Event Generation and Scoring

Instead of randomly placing events in the source region to create a uniform activity distribution, events in VIDA are generated voxel-by-voxel based on an activity map derived from quantitative SPECT or PET imaging. The simulation can be run to include events in the whole body or by selecting an organ or tumor volume as source, as specified in the input file (see Appendix D). Within each voxel, events are assumed to be uniformly distributed, with randomly selected position and direction vectors.

VIDA employs the built-in radioactive decay module (Hauf et al. 2013a) to produce primary particles based on the branching ratios and decay energy of the radionuclide of interest. The radionuclide is defined as an ion with an atomic number and mass from the simulation input file. The decay library includes information on the nuclear half-life, nuclear structure of the parent and progeny, branching ratios, and energy of the decay structure taken from the Evaluated Nuclear Structure Data File (Tuli 1996) for each nuclide. For the case of nuclides that decay to excited isomers, the prompt de-excitation of the daughter nucleus via isomeric transition occurs based on photon evaporation files that include internal conversion coefficients.

Particle interactions in Geant4 are performed "silently," requiring the user to define a scorer for the detector volume(s) to extract desired information. Each scorer collects one physics quantity for each physical volume. VIDA employs a primitive scorer for deposited energy. Energy deposition due to each primary event, including secondary particles and any subsequent gamma emission due to de-excitation of the nucleus, is tallied for each voxel. Once all events are tracked, the simulation produces a map of the total energy deposited that is used to create a 3D dose rate map for input to VIDA's voxel-level kinetics processing.

The ability to produce primary events based on the decay scheme of a radionuclide and perform whole field of view simulation by sampling the activity distribution in a patient from 3D functional image is a distinctive feature of VIDA. Other 3D dosimetry applications such as 3D-RD (Prideaux et al. 2007) require separate simulations of decay products (i.e. electrons for β^- and Auger emission or photons for gamma emission and characteristic x-rays). The energy deposition distributions from all decay components must then be added together, weighted by the transition probabilities. The Geant4 3D dosimetry code RAYDOSE (Marcatili et al. 2013) uses the general particle source (GPS) to access the radioactive decay module. The GPS is limited to generating primary particles with 2D spatial sampling and thus, each slice of the functional image must be run independently. RAYDOSE must then perform a post-processing summation of the 3D dose rate maps corresponding to each slice as the source of activity. Another Geant4 dosimetry application for internal dosimetry GRNT (McKay 2011) uses the command line interface to define all necessary simulation components including phantom geometry, physics options, simulation materials, and the radionuclide emission spectrum. Although this approach may offer increased flexibility, it also demands significant effort from the user to create a working simulation.

3D Kinetics Processing

Patient kinetics modeling is performed by the exponential fitting module in VIDA. This module (see Figure III.4) consists of a MATLAB-based GUI for curve fitting by iterative least squares estimation (Statistics Toolbox, Release 2012a). Non-linear regression is performed using the Levenberg-Marquardt nonlinear least squares algorithm. The user has a choice of fit functions depending on uptake kinetics and number of sequential scans. Instantaneous activity

uptake, resulting in exponentially decaying dose rates, can be fit to a mono-exponential or bi-exponential function of the general form:

$$\dot{D}(t) = \dot{D}_1 e^{-\lambda_1 t} + \dot{D}_2 e^{-\lambda_2 t}.$$

Initial guesses for the rate components ($\dot{D}_1$ and $\dot{D}_2$) are derived from the time-sequence data and elimination constants (λ_1 and λ_2) from the physical half-life of the radionuclide of interest. The fitting algorithm automatically detects voxels with non-instantaneous uptake (i.e. tumor) and fits these data to a bi-exponential including the (0, 0) point of the form:

$$\dot{D}(t) = \dot{D}_0 (e^{-\lambda_1 t} - e^{-\lambda_2 t}).$$

The voxel dose is computed by integration of the fitted function based on a time interval supplied by the user, with a default range of zero to infinity. Non-physical clearance (e.g. increased activity at later time points) may arise at body and organ boundaries due to errors in image registration across sequential scans. The application checks for these occurrences during the fit routine and attempts to fit an exponential curve with this time point omitted.

The exponential fitting tool in VIDA provides the user with several options. The user may choose to fit the entire body in the image field of view or select specific organs and tumors based on the organ map. Also, the user may specify the resolution of the resulting dose map. A scaled map with voxel dimensions twice as large in the transverse plane is created by fitting a voxel dose curve to the data in the corresponding 2×2×1 cell in the original array. This option decreases the overall processing time and may facilitate regression convergence when data are only available for a limited number of time points.

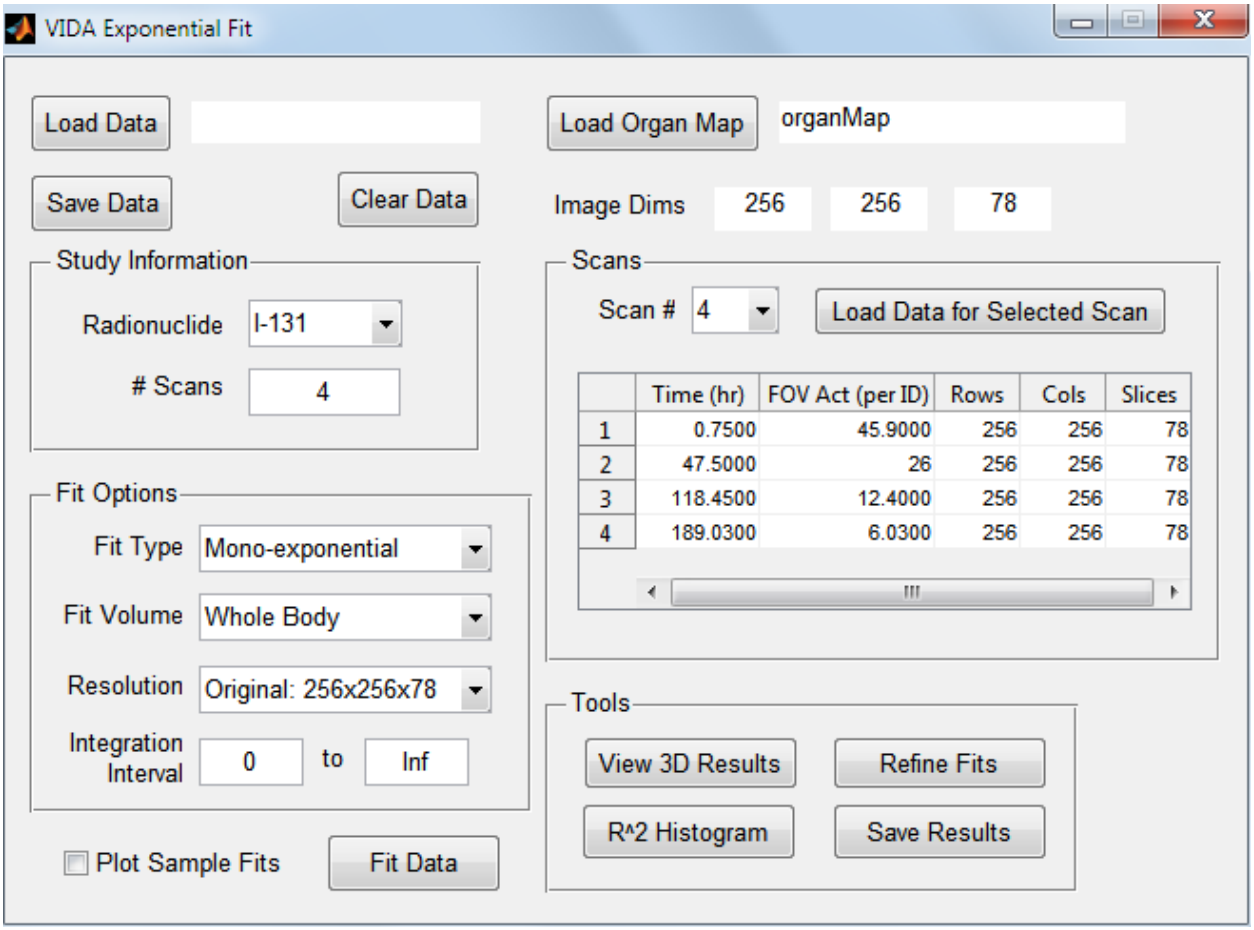

Figure III.4: Graphical user interface of the MATLAB-based exponential fitting tool in VIDA.

Evaluation tools are provided by the exponential fitting module to assess the results. The user can plot a histogram of the coefficients of determination (R^2) for fitted voxels. If necessary, voxels with R^2 values below a user-defined threshold may be refined by re-running the regression using an array of different initial coefficient values to improve the fit. In addition, the VIDA exponential fitting module provides a three-plane viewer to evaluate the results and plot the raw data and fitted curve for a selected voxel (see Figure III.5).

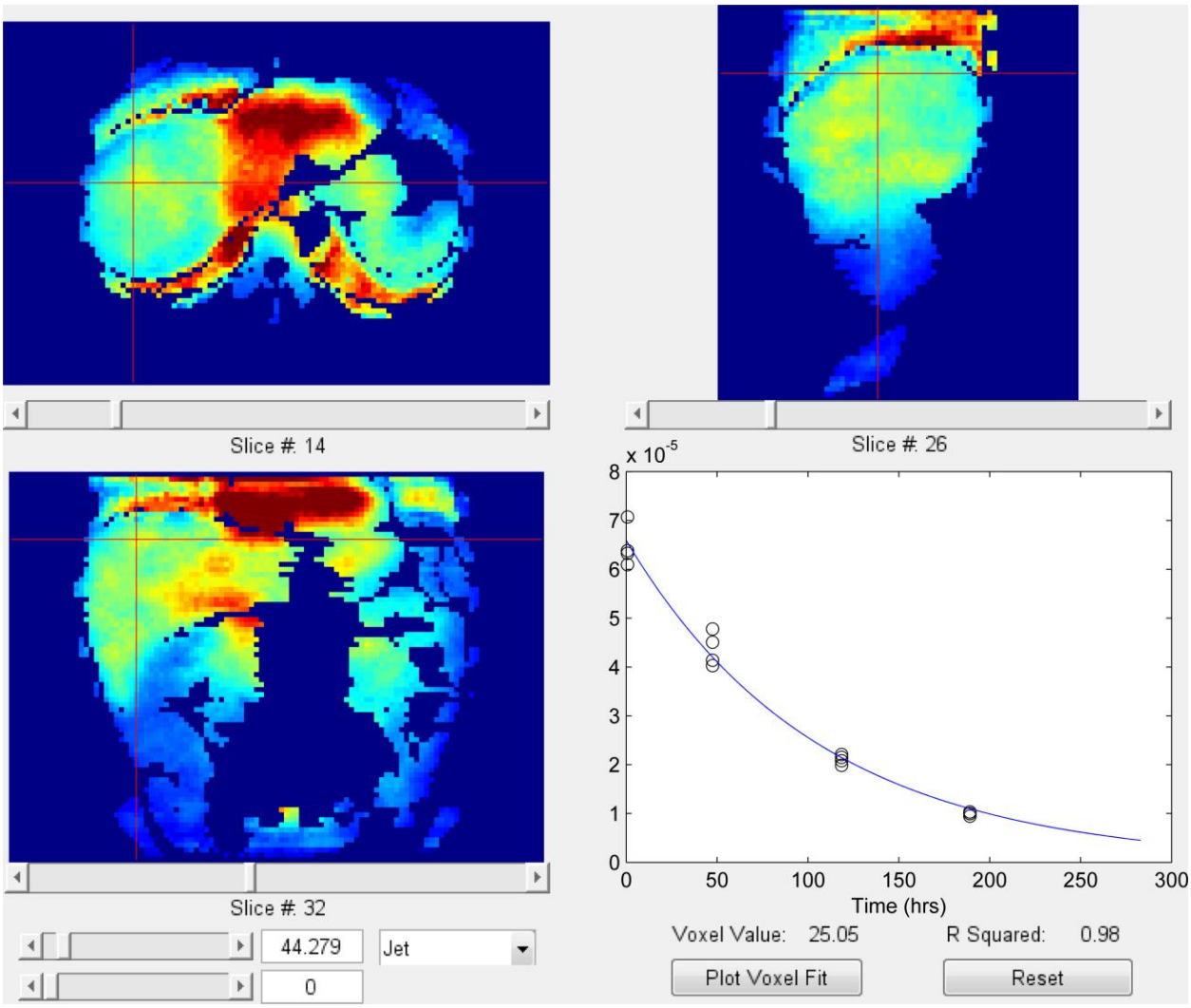

Figure III.5: 3D viewer in VIDA exponential fitting tool to evaluate integrated dose map and voxel fits.

VIDA was designed to generate dose rate maps at each time point and perform curve fitting and integration of dose at the voxel. Although this technique requires additional simulations, the rational for this approach is twofold. The determination of instantaneous dose rates permits inclusion of tumor regression over scan times in the absorbed dose estimates. Also, incorporation of radiobiological models requires 3D absorbed dose rate images at each time point rather than the simulation of absorbed dose from a single map of cumulated activity. A similar approach of generating multiple dose rate maps has been implemented in other dosimetry studies (Dewaraja

et al. 2009, Howard et al. 2011, Senthamizhchelvan et al. 2012, Sgouros et al. 2011). However, if desired, the user can use the exponential fitting tool in VIDA to create a map of cumulated activity for input in the MC simulation to determine the integrated dose in each voxel with only one run.

Validation

Due to the inherent flexibility of MC simulation tools such as Geant4, verification of the results is of the utmost importance. Monte Carlo results in VIDA were validated using two independent techniques. The first method applies a simple geometry of a spherical source in a semi-infinite scattering medium. The self-dose to spheres of various volumes was determined assuming a uniformly distributed activity. The second approach compared dose factors for selected target organs in a standard male reference phantom assuming uniform activity in the source organs.

Methods

Simulations were performed to determine absorbed fractions for self-absorption in unit-density spheres ranging in size from 10 to 1000 grams. For consistency with the way a patient is modeled, each sphere was "voxelized" into an array of cells large enough to include the surrounding scattering medium. The spatial resolution of the voxelized map was chosen to limit the error in sphere mass due to the digitized approximation of the surface to less than 0.5%. The spheres were modeled as a tissue-equivalent material surrounded by a semi-infinite scattering medium of water. The tissue composition of the sphere was taken from MIRD Pamphlets 3 and 8 (Brownell et al. 1968, Ellett & Humes 1972), chosen to facilitate comparison to previously published results.

Uniform activity was simulated for common radionuclides used in TRT including ^{90}Y, ^{131}I, ^{111}In and ^{177}Lu. For each radionuclide of interest, one million events were tracked resulting in absorbed energies within the sphere with relative errors of less than 0.5%. Relative error is defined as the 1σ standard deviation of the average tally (energy deposited) divided by the average tally (Sweezy et al. 2003). Self-dose factors were calculated and compared the unit density sphere model in OLINDA/EXM (Stabin et al. 2005). The OLINDA/EXM program calculates dose factors from self-irradiation of unit density spheres of discrete masses ranging from 0.01 to 6000 grams. These doses factors are based on the most currently published absorbed fractions of photon and electron emitters in spheres of various sizes (Stabin & Konijnenberg 2000)

In order to validate VIDA in a more complex geometry with different tissue types, dose factors for several organs of interest were determined using the RADAR reference adult male phantom (see Figure III.6) (Stabin et al. 2012). Cross-organ dose factors were included to confirm dose contributions from far-reaching photons. Phantom anatomy is represented by NURBS surfaces adapted from the 4D NCAT/XCAT phantom (Segars et al. 2001, Segars et al. 2010) to have reference organ masses for the adult male defined by ICRP publication 89 (ICRP 2002). The phantom was rendered in voxel format with a resolution of 1.5 x 1.5 x 5.0 mm to create an organ map for simulation. Any voxels in the array outside of the phantom were defined as air. Instead of using the default materials defined in Table III.1, simulation materials were changed to the densities and compositions of soft tissue, lungs and bone (see Table III.3) used to generate new specific absorbed fractions (SAFs) for the RADAR reference data.

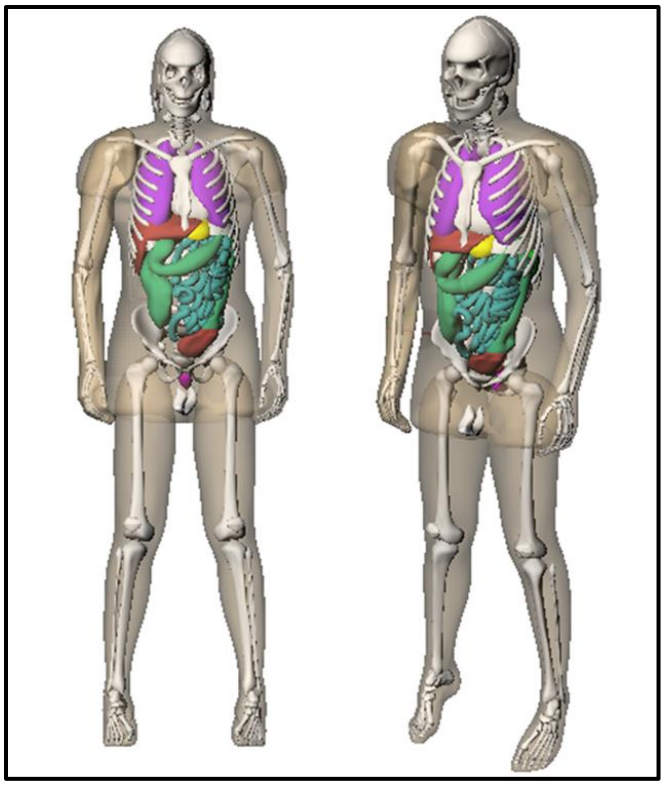

Figure III.6: Anterior views of the RADAR adult male NURBS phantom.

Simulations were performed for the same radionuclides as the uniform spheres (^{90}Y, ^{131}I, ^{111}In, and ^{177}Lu) with three different organs designated as the source of radioactivity (liver, spleen, and pancreas). These organs were chosen as representative sources centrally located in the body with varying shape. Each run generated 5 million decay events uniformly throughout the source organ, resulting in relative errors of less than 2% in the total energy deposited in each target volume. Dose factors were determined using the average dose deposited in each target organ and compared to reference data. Target volumes included the three source organs and also the lungs and kidneys to evaluate self-dose and cross-organ doses to distant structures that may be of interest in TRT dosimetry.

Table III.3: Materials used in the simulation of dose factors for the reference adult male phantom. Tissue definitions taken from Oak Ridge National Lab Report ORNL/TM-8381/V1, Table A-1 (Cristy & Eckerman 1987).

Material	Density (g/cm^3)	Chemical Composition (% by mass)											
		H	C	N	O	Na	Mg	Si	P	S	Cl	K	Other
Air	1.21×10^{-3}		0.01	75.5	23.2								1.3 (Ar)
Soft Tissue*	1.03	10.45	25.66	2.49	63.53	0.11	0.01	0.03	0.13	0.20	0.13	0.21	0.02 (Ca)
Lung Tissue†	0.296	10.13	10.24	2.87	75.75	0.18	0.01	0.01	0.08	0.23	0.27	0.19	0.01 (Ca), 0.04 (Fe)
Whole Bone‡	1.40	7.34	25.48	3.06	47.89	0.33	0.11		5.10	0.17	0.14	0.15	0.03 (F), 0.01 (Fe), 10.19 (Ca)

*Also contains 0.005% or less of Fe, Zn, Rb and Zr
†Also contains 0.005% or less of Zn and Rb
‡Also contains 0.005% or less of Si, Zn, Rb, Sr, and Pb

Results

Dose factors for self-dose to uniform activity spheres are shown in Figure III.7. The differences between VIDA and OLINDA/EXM (Stabin et al. 2005) ranged from 0.4% to 5%, with the largest deviations occurring in the smallest sphere (see Table III.4). Dose factors for ^{90}Y show the largest difference between the two models with a range of 2–5%.

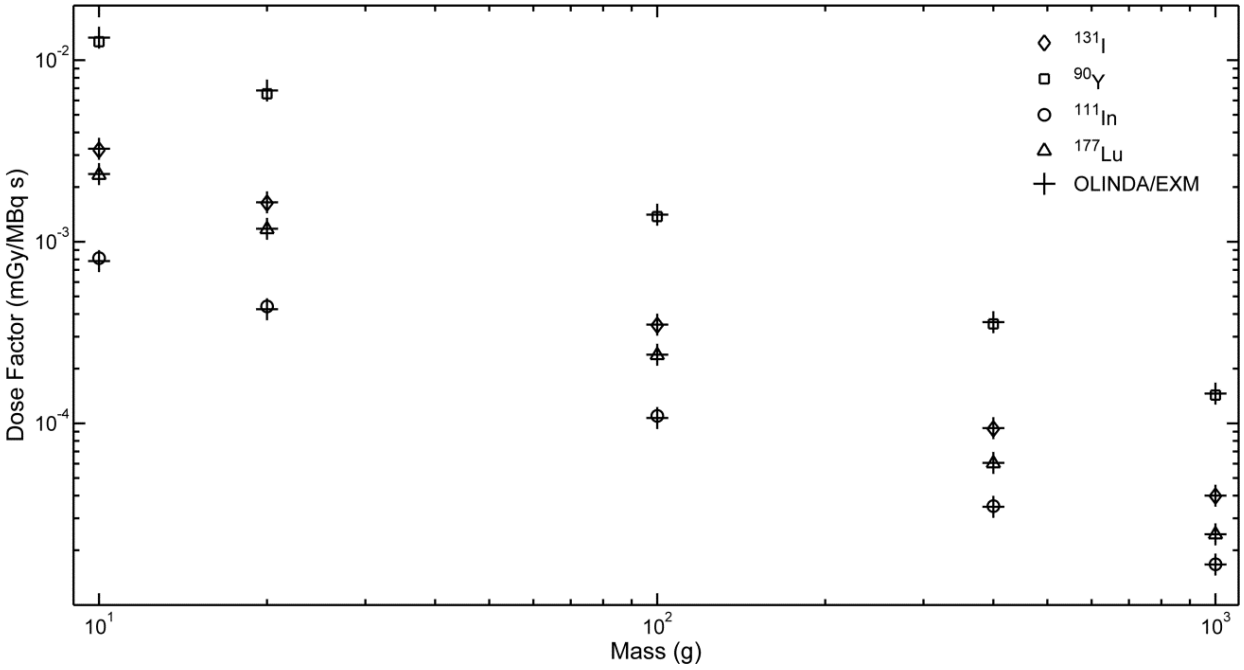

Figure III.7: DF comparison between VIDA and OLINDA/EXM for unit density soft tissue spheres of different masses.

Table III.4: Relative percent differences in VIDA and OLINDA/EXM sphere dose factors

Mass (g)	Diameter (cm)	^{131}I	^{90}Y	^{111}In	^{177}Lu
10	2.7	-1.4	-5.0	3.8	-1.3
20	3.4	-0.9	-4.1	3.8	-0.9
100	5.8	-0.9	-2.5	2.8	-0.7
400	9.1	-0.9	-2.3	0.9	-0.7
1000	12.4	-0.5	-2.1	0.4	-0.4

Relative % difference defined as $100 \times (DF_{VIDA} - DF_{OLINDA}) / DF_{OLINDA}$.

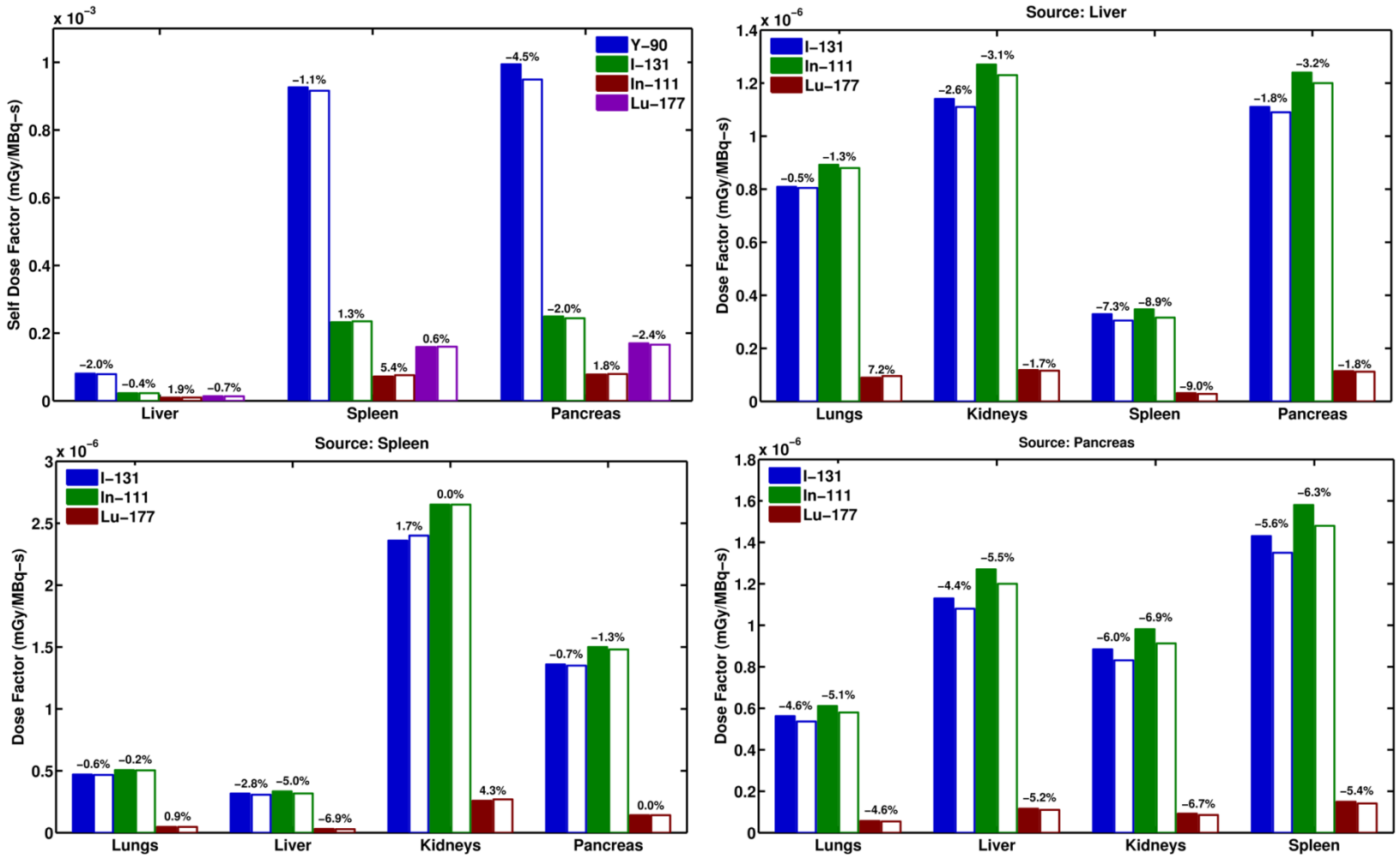

Figure III.8: Self and cross organ dose factors for liver, spleen, and pancreas in the RADAR adult male phantom. Solid bars are reference values (Stabin et al. 2012) and outlined bars are from VIDA. Percent differences are listed above each pair, defined as 100 × (DF_{VIDA} – DF_{RADAR}) / DF_{RADAR}.

Results for the reference phantom study are presented in Figure III.8. Cross-organ dose factors are omitted for ^{90}Y because beta-emission energy is mostly absorbed locally. Any dose deposited in target regions far from the source organ is mainly due to contributions of bremsstrahlung radiation, with low scoring statistics. Deviations in the dose factors for organ self-dose ranged between 0.6% and 5%. The difference in cross-organ dose factors spanned from 0% to 9% with VIDA results being lower than OLINDA/EXM values for almost all source-target organ pairs.

Discussion

The agreement in dose factors for the spheres was within 5% and improved with increasing mass, due to the decreased likelihood of an electron escaping the source volume before complete energy absorption. For all sphere sizes, the largest differences occurred for ^{90}Y, a nearly pure beta emitter. The discrepancy is most likely due to different methods used to sample the beta energy spectrum. OLINDA/EXM applies a single SAF for the average energy of the beta emission spectrum, whereas beta particles created from a decay event in Geant4 are assigned energies by sampling the β-Fermi-function (Hauf et al. 2013a). Beta emissions with energy higher than the spectrum mean have a longer range in tissue and higher interaction likelihood; however there is also an increased possibility of these electrons exiting the sphere without being scored, which results in less total energy absorbed reflected by the lower dose factors from VIDA.

For radionuclides that undergo beta decay (^{131}I, ^{90}Y and ^{177}Lu), dose factors calculated by VIDA for spheres and the majority of source/target pairs in the reference phantom are slightly lower compared to OLINDA/EXM. However, all self-dose factors from VIDA are higher for ^{111}In. ^{111}In decays by electron capture and dose is locally deposited by low energy Auger

electrons and small yield internal conversion electrons. The difference in ^{111}In self-dose factors may be due to error in the interpolation of SAFs for the very low energy Auger electrons by OLINDA/EXM and improved low energy electron transport models in Geant4 compared to MNCP4B; nonetheless, the differences are small.

Several other groups have performed simulations of internal radioactive sources using Geant4. Amato et al. (Amato, Amato) reported absorbed fractions for monoenergetic photons and electrons in ellipsoids. Using these data, they specified the average energy deposited per disintegration of ^{131}I as a function of the generalized radius. The energy deposited per disintegration of ^{131}I by VIDA for the two smallest spheres (10 and 20 g) was 201 keV and 205 keV respectively. These energies are in excellent agreement with Amato et al. (Amato) for ellipsoidal sources with generalized radii of 1.34 cm (201 keV) and 1.68 cm (206 keV). The dosimetry application RAYDOSE (Marcatili et al. 2013) was validated using dose factors for water spheres based on imaging a phantom containing activity-filled spheres of various sizes. For ^{131}I and ^{177}Lu, RAYDOSE dose factors were within 1–3% of OLINDA/EXM and agree with the evaluation of VIDA and OLINDA/EXM for spheres of comparable sizes. The radionuclide therapy code GRNT (McKay 2011) was validated by comparing organ dose factors from the MIRD-5 phantom to RADAR reference data. The relative differences found using GRNT for liver as the source organ were approximately 5% for self-dose factors and 1-10% for cross-organ dose factors to the kidneys, lungs, pancreas, and spleen for ^{131}I and ^{90}Y, which are similar to those from VIDA.

Summary

We have developed VIDA, an application for patient-specific dosimetry in targeted therapy using the Geant4 Monte Carlo toolkit to model radiation absorption in tissue from

internal emitters. The simulation generates voxel-level dose rate maps based on anatomical and quantitative functional imaging. It has been benchmarked with results using the RADAR formalism including self-dose factors for uniform activity spheres and organ self-dose and cross-organ doses in a standard phantom. Validation results were compared to published results from other Geant4-based dosimetry methods with excellent concordance. VIDA also includes a useful curve fitting tool to automate voxel-level dose rate fitting and integration over time to create a 3D absorbed dose map. It is our aim to employ this dosimetry technique in conjunction with patient-specific organ maps created from a deformable NURBS anatomical model. The method for creating an individualized patient model from a standard NURBS model is the topic of Chapter IV. VIDA, combined with the ability to define patient anatomy from a deformable phantom, offers a novel method for patient-specific dosimetry in TRT that can be completed in a short time-frame more favorable with the clinical treatment schedule.

CHAPTER IV

PATIENT-SPECIFIC ANATOMICAL MODELING USING DEFORMABLE NURBS PHANTOMS

Introduction

Patient-specific dose assessment requires three distinct components. Anatomical images enable the definition of volumes of interest (VOIs) and provide tissue density information. Time-sequential voxel-based quantitative activity distributions reveal the radiopharmaceutical kinetics in the patient. A computational method, such as MC simulation, calculates the absorbed dose in the patient-specific model. Much of the progress in patient-specific dosimetry in TRT focuses on the latter two elements. Definition of VOIs is still primarily limited to manual or semi-automatic segmentation, which is a time consuming and labor-intensive endeavor. Often, this step is a major bottleneck in the overall dosimetry process and full-scale patient segmentation is avoided. Dosimetry studies have restricted their focus solely on tumor dose (Dewaraja et al. 2014, Senthamizhchelvan et al. 2012), alleviating the need to define healthy organs. In some cases, such as RIT for lymphoma, this approach is permissible because the doses are low and do not pose a risk for organ toxicity. Other studies have employed simple segmentation methods to define dose limiting volumes for treatment planning, such as using an activity threshold to separate lung tissue from thyroid cancer metastases (Sgouros et al. 2011). Newly-developed molecular-based therapies (i.e. PRRT) have a much lower therapeutic window and the risk to normal tissues, especially kidneys, is high. This necessitates calculation of dose to not only tumor volumes but also to radiosensitive organs, and performing satisfactory dosimetry for these treatments requires delineating multiple volumes from anatomical patient data. To date, PRRT

dosimetry studies have used manually drawn VOIs (Baechler et al. 2012) or mean activity concentrations of spherical volumes inside organs of interest (Sandström et al. 2013) to obtain dose estimates to organs such as liver, kidney and spleen. Compared to manual segmentation, the approach by Sandström et al. is simple and efficient, but limits organ doses to mean values assuming a uniform activity distribution in the organ.

There has been growing interest in constructing NURBS-based patient-specific phantoms for use in dosimetry. Numerous patient-specific NURBS-based XCAT models have been developed by Duke University to assess CT dose in pediatric patients (Norris et al. 2014, Norris et al. 2014a) and adults (Segars et al. 2013). These models were constructed based on manually-segmented patient CT data. The bones and major organs were segmented from the CT data to define a framework for each phantom. The multichannel large deformation diffeomorphic metric mapping (MC-LDDMM) algorithm (Segars et al. 2009, Tward et al. 2011) was used to calculate a high-level transform from a given XCAT template (male or female) to the segmented framework for each patient. The transform was then applied to the XCAT phantom template (Segars et al. 2010) to define the additional organs and structures, not segmented from the CT data, into the patient-specific model, creating a new patient-specific XCAT phantom.

The MC-LDDMM algorithm relies on the manually-segmented patient organs as landmarks to deform the entire phantom. This approach provides accurate results, with structures in agreement within a few voxels and organ dose estimates within 10%. However, the computational time to produce a patient-specific model is considerable, and significantly varies depending on the number of processors and patient size (less than an hour for a small patient using 24 processors up to 28 hours for a large patient using a single processor). This method of patient-specific NURBS modeling does not completely eliminate manual segmentation and may

require excessive computational processing power and time for it to be viable for clinical treatment planning for TRT. Moreover, the conversion of the segmented structures to 3D NURBS surfaces requires the use of commercial NURBS modeling software such as Rhinoceros 3D (McNeel North America, Seattle, WA).

Here, we describe a more efficient method for creating patient-specific models by deforming a NURBS reference phantom. In order to complete this task, we have developed custom software with a collection of tools and algorithms that can be used to manipulate the NURBS surfaces that define the reference organs to match the patient anatomy. The software loads patient CT images and overlays the outline of phantom in each viewing plane. Following a specified work-flow, the user modifies the body contour, skeleton, and individual organs to reflect the anatomical data in the CT. This chapter is organized into three main sections. The first section introduces the reader to NURBS and provides a formal definition of their mathematical form. The second section outlines the development of the software, including descriptions of the implemented algorithms and the procedure to construct a patient-specific NURBS model. The chapter concludes with the validation of the method using manually-segmented PET/CT images.

Overview of NURBS

Non-Uniform Rational B-Splines (NURBS) are mathematical representations of arbitrary 3D geometries using polynomial basis functions. A NURBS model is defined by its degree and contains control points, corresponding weights, knot vectors, and a set of evaluation rules for the polynomial basis functions that determine how the control points influence the geometry. Surfaces are defined by a bi-directional NURBS model with parametric variables u in longitude and v in latitude. Points on the surface $\mathbf{S}(u, v)$ are defined by the following equation (Piegl & Tiller 1997):

$$\mathbf{S}(u,v) = \frac{\sum_{i=0}^{n}\sum_{j=0}^{m} N_{i,p}(u)N_{j,q}(v)w_{i,j}\boldsymbol{P}_{i,j}}{\sum_{i=0}^{n}\sum_{j=0}^{m} N_{i,p}(u)N_{j,q}(v)\,w_{i,j}} \qquad \text{IV.1}$$

where $\mathbf{P}_{i,j}$ is a control point weighted by the scalar value $w_{i,j}$, and $N_{i,p}(u)$ and $N_{j.q}(v)$ are polynomial (B-spline) basis functions of degree p and q respectively. The surface points of $\mathbf{S}(u,v)$ and the $(n + 1)$ by $(m + 1)$ matrix of control points **P** in equation IV.1 are expressed in homogeneous coordinates $(x, y, z, 1)$.

The basic shape of the surface geometry is governed by the control points that may, but typically do not, lie on the surface. Instead, control points fall on a grid defined by the knot vectors **U** and **V**:

$$\mathbf{U} = \left(\underbrace{0,\ldots,0}_{p+1}, u_{p+1}, \ldots u_{r-p-1}, \underbrace{1,\ldots,1}_{p+1}\right)$$
$$\mathbf{V} = \left(\underbrace{0,\ldots,0}_{q+1}, v_{q+1}, \ldots v_{s-q-1}, \underbrace{1,\ldots,1}_{q+1}\right) \qquad \text{IV.2}$$

where $r = n + p + 1$ and $s = m + q + 1$. The knot vectors partition the surface into piecewise components in the parametric directions u and v (see Figure IV.1). Knot intervals are not restricted to uniform spacing, hence "non-uniform" in the name NURBS. Control over the spacing and multiplicity of the knots provides the ability to define complex geometries, including sharp edges, without discontinuities.

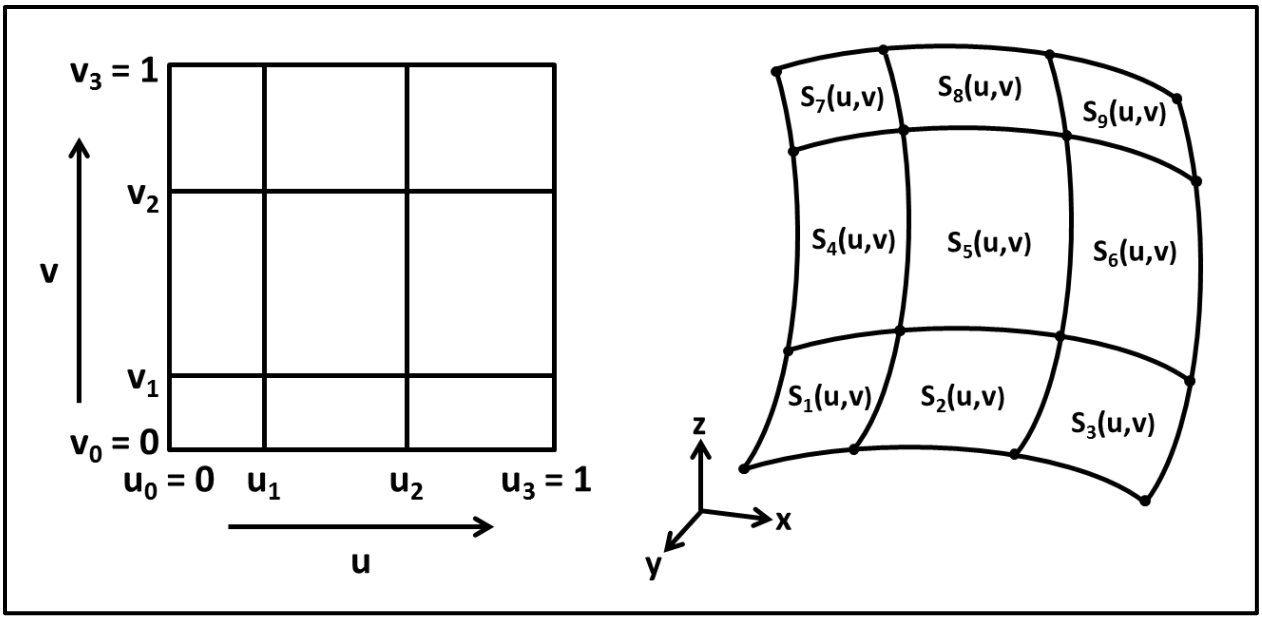

Figure IV.1: Schematic representation of knot vectors that divide the NURBS surface into piecewise segments. Surface degree of $p = 3$ and $q = 3$ with knot vectors given by $\mathbf{U} = (0, 0, 0, 0, u_1, u_2, 1, 1, 1, 1)$ and $\mathbf{V} = (0, 0, 0, 0, v_1, v_2, 1, 1, 1, 1)$. Note that the spacing is not uniform in each parametric direction.

Each piecewise component of the surface has a set of unique basis functions that weight the control points. Basis functions $N_{i,p}(u)$ and $N_{j,q}(v)$ are defined by equation IV.3. For each point on the surface $\mathbf{S}(u,v)$, basis functions are only non-zero over the knot interval $[u_i,u_{i+p+1})$ and $[v_j,v_{j+q+1})$ of $\mathbf{U}$ and $\mathbf{V}$ respectively, where $u_i \leq u < u_{i+1}$ and $v_j \leq v < v_{j+1}$. The weighting coefficient of control point $\mathbf{P}_{i,j}$ is the product of $N_{i,p}(u)$, $N_{j,q}(v)$ and $w_{i,j}$, and is therefore only non-zero if at least one basis function is non-zero over the knot interval. This property creates local control of the surface shape, and altering the position of a control point only influences the $p + 1$ (or $q + 1$) neighboring surface patches (see Figure IV.2).

$$N_{i,0}(u) = \begin{cases} 1, if\ u_i \leq u \leq u_{i+1} \\ 0, otherwise \end{cases}$$

$$N_{i,p}(u) = \frac{u - u_i}{u_{i+p} - u_i} N_{i,p-1}(u) + \frac{u_{i+p+1} - u}{u_{i+p+1} - u_{i-1}} N_{i+1,p-1}(u) \qquad \text{IV.3}$$

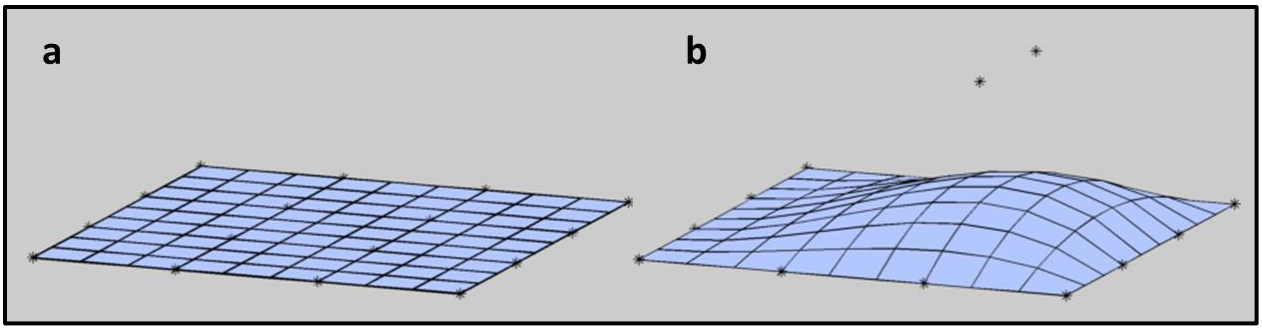

Figure IV.2: Modification of NURBS surface by moving control points. (a) NURBS representation of a plane with controls points (*) aligned on the surface. (b) Surface with shaped altered by translating two of the center control points in the z-axis.

As shown in equation IV.3, the area of the surface impacted by the control points depends on the degree of the NURBS model. Thus increasing the degree of the model, in turn increasing the degree of the basis polynomials, will result in control points influencing a larger area of the surface. Although higher degree polynomials provide increased flexibility, they may also affect the smoothness of the surface and create unwanted bumps. Typically, cubic polynomial basis functions (degree = 3) provide an adequate compromise between elasticity and constraint. The degree of all NURBS models used in this work is three in both parametric directions.

Although NURBS are complex mathematical models, they have many properties that make them a desirable primitive for modeling patient anatomy. NURBS surfaces have affine invariance, meaning that applying a transformation to the surface is equivalent to applying the same transformation to the control net that defines the surface. A surface is easily translated, rotated or scaled by multiplying the matrix of control points ($\mathbf{P}_{i,j}$) by the appropriate transformation matrix ($\boldsymbol{T}$):

$$\mathbf{P}_{i,j}^{\ transformed} = \boldsymbol{T}\mathbf{P}_{i,j} \qquad \text{IV.4}$$

The local morphology of a surface can also be altered by manipulating individual control points. If the location a control point changes, only the piecewise surface patches influenced by that

specific point (through non-zero basis functions) are modified. The local modification property of NURBS allows specific areas on the surface to be deformed by the altering the positions of the control points. Thus, organs in the phantom template can be modified to match patient anatomy as if they were made of clay. Additionally, NURBS surfaces are continuous and surface points can be expressed at any resolution. This permits the creation of a 3D image map of the anatomical NURBS phantom to be generated with arbitrary spatial resolution. Thus, patient-specific NURBS phantom can be transformed or "voxelized" to create an organ map that matches the spatial resolution of the quantitative activity images.

Development of the Phantom Morphus Software

Introduction

The Phantom Morphus software is based on an existing interactive application to model patient populations using the NCAT Phantom (Segars et al. 2000, Segars et al. 2001). The focused use of this software was to study patient anatomy in myocardial SPECT and was limited to anatomical modifications to the original NCAT phantom using SPECT images as a reference. The transformations included translation and scaling of the diaphragm, heart, lungs, rib cage, and body outline as well as rotations of the rib cage and heart. The remaining organs (liver, spleen, stomach and kidneys) were not deformed.

We have expanded this software to perform interactive modification of anatomical structures guided by high-resolution CT as a method to create full body patient-specific models for dosimetry in TRT. The NCAT phantom, initially limited to torso anatomy including the heart, lungs, liver, stomach, spleen, kidneys and surrounding skeleton (sternum, ribs, and thoracic vertebrae), has been extended to the entire body resulting in the XCAT phantom (Segars et al. 2010). The Phantom Morphus software employs the extended full-body XCAT phantom to

create individualized anatomical models that include all organs at risk for TRT and a complete skeleton for bone marrow dosimetry. Ten small spherical surfaces were added to the reference phantom used in Phantom Morphus for definition of tumor volumes. In addition to applying simple affine transformations to the control points, the software includes new algorithms that enable non-rigid transformations of the organ models. This section contains descriptions of these algorithms as well as a detailed summary of the overall software design. Guidance is given on how to use Phantom Morphus to construct a patient-specific model.

Software Design

Phantom Morphus is written in Visual C++ using the OpenGL application programming interface for rendering 3D graphics. The main GUI (see Figure IV.3) consists of two display windows, one for the 3D NURBS phantom and the other containing a 2D display of the CT image, with transverse, sagittal and coronal view options. The user loads a patient CT by selecting "Load Patient Data" from the "Patient Data" drop down menu. The phantom is rendered as an overlay to the CT image using triangulated surfaces that match the voxel dimensions of the CT image.

The CT data must be in raw image format to load into Phantom Morphus. Because raw data lacks header information, the user must specify the image dimensions (number of rows, columns, and slices) and the data type and storage order (e.g. unsigned short, big-endian) before the software can load the data into memory. The user must also set the voxel dimensions of the image in the "Image View Tools" GUI (see Figure IV.4) so that the NURBS surfaces are triangulated and displayed over the 2D CT image at the matching resolution. The Image View Tools panel also contains other image display options including zoom, brightness and contrast adjustment and toggles between the three image planes (transverse, coronal, and sagittal).

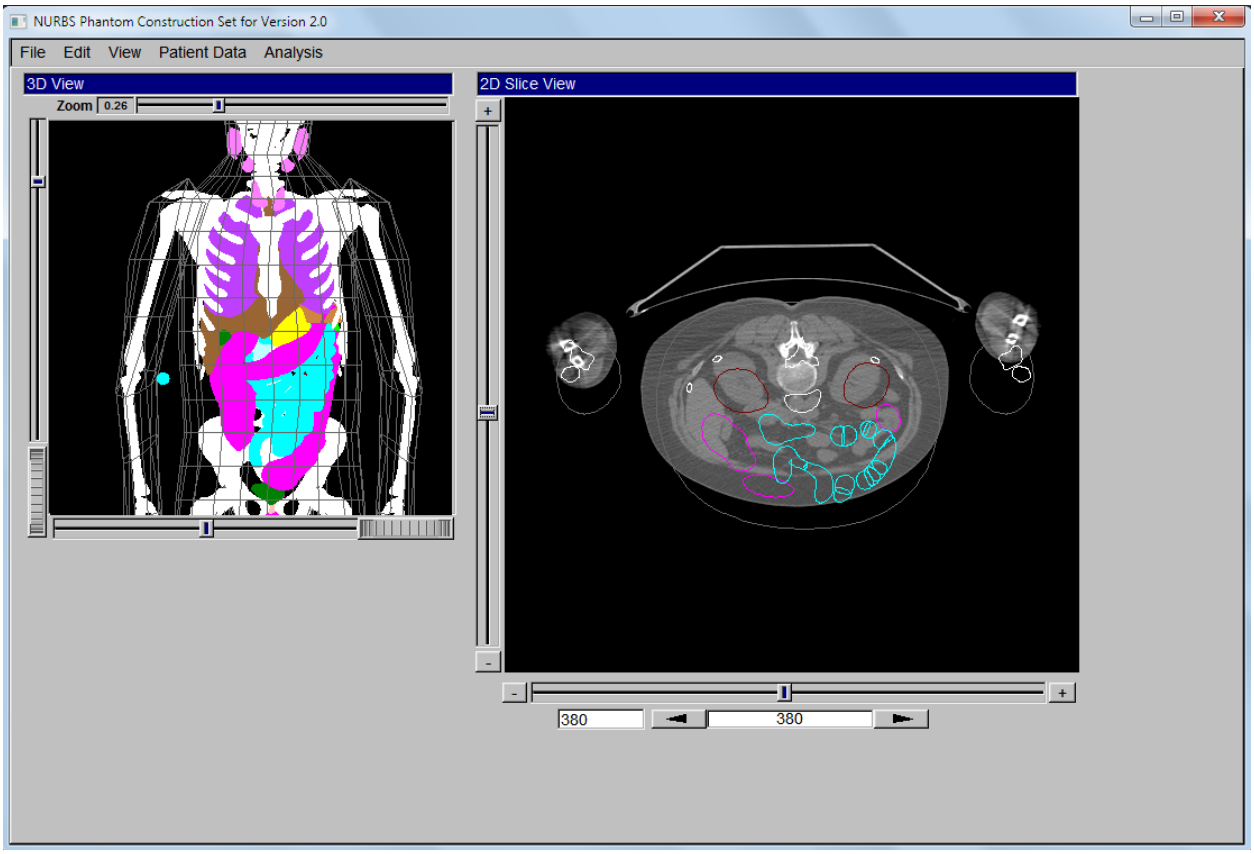

Figure IV.3: 3D and 2D views of the Phantom Morphus software main graphical user interface.

Selection of phantom structures for transformation is handled by the “Phantom Structures” window (see Figure IV.5). The user is permitted to select a single organ or a set of organs for manipulation. Options to display or hide selected and unselected objects in the CT image window are available. The organ models in the 3D phantom view window can be rendered as wireframe (default for body contour) or solid objects (default for organs and skeleton). The control points of the selected structures can also be shown in the 2D image view.

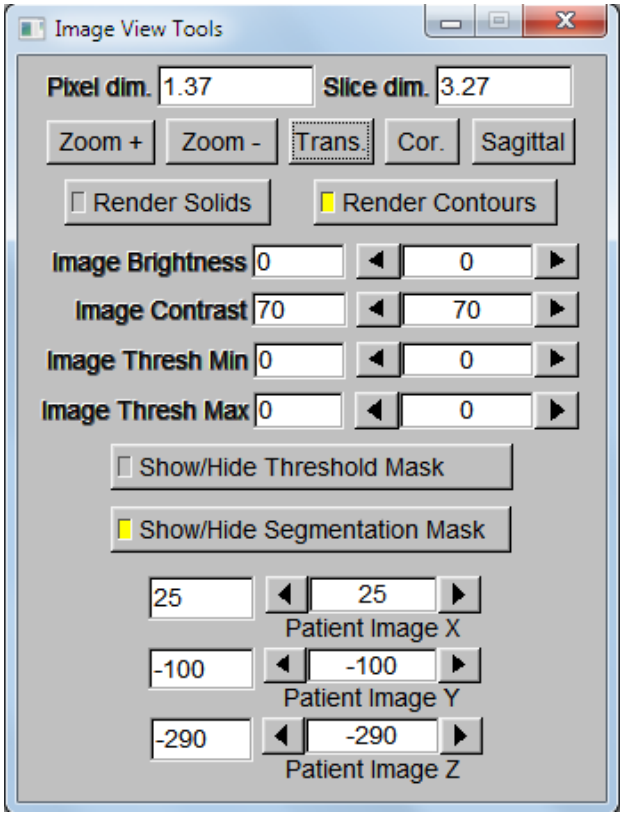

Figure IV.4: GUI of image view tools for CT image display.

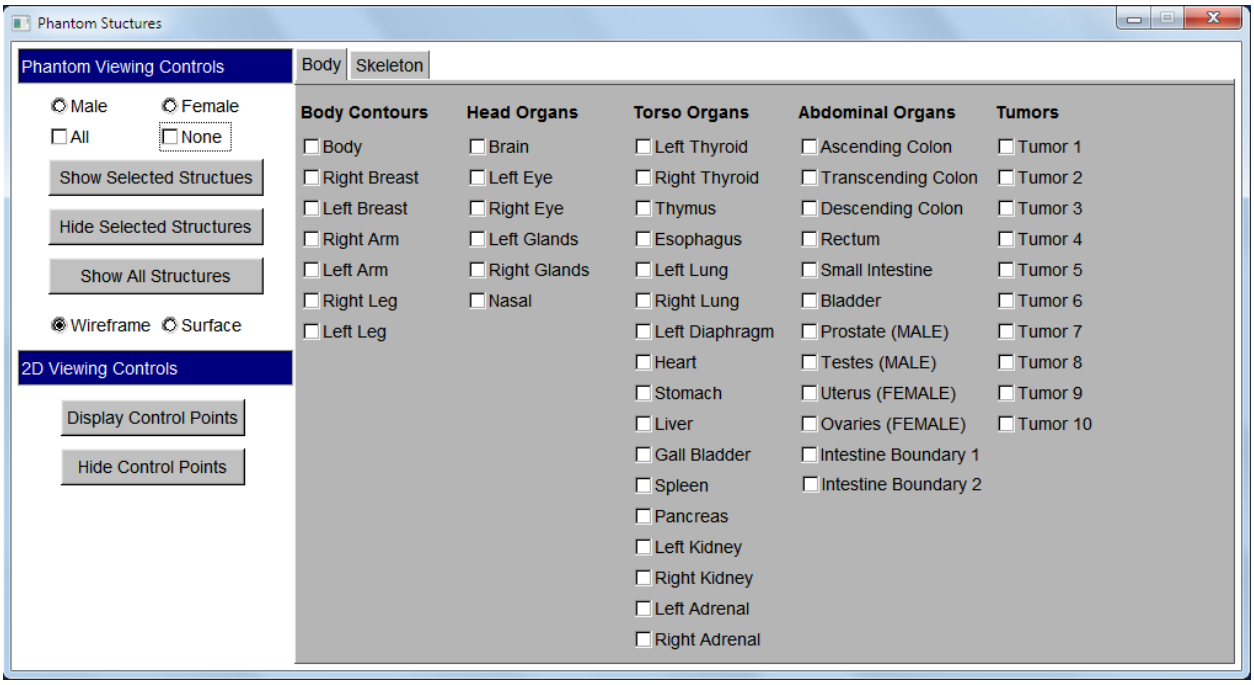

Figure IV.5: GUI for NURBS phantom viewing options and selection of structures.

A screen capture of the "Tools" window is show in Figure IV.6. This GUI contains all the tools provided to the user to deform the template organ. The window is divided into three main sub-panels. One sub-panel includes the available options for modifying the surface(s) using affine transformations. Another sub-panel contains a set of standard segmentation tools to manually define volumes of interest from the CT image. The third sub-panel includes special transformation tools for surface modification. Details of these custom deformation algorithms are given in the following section.

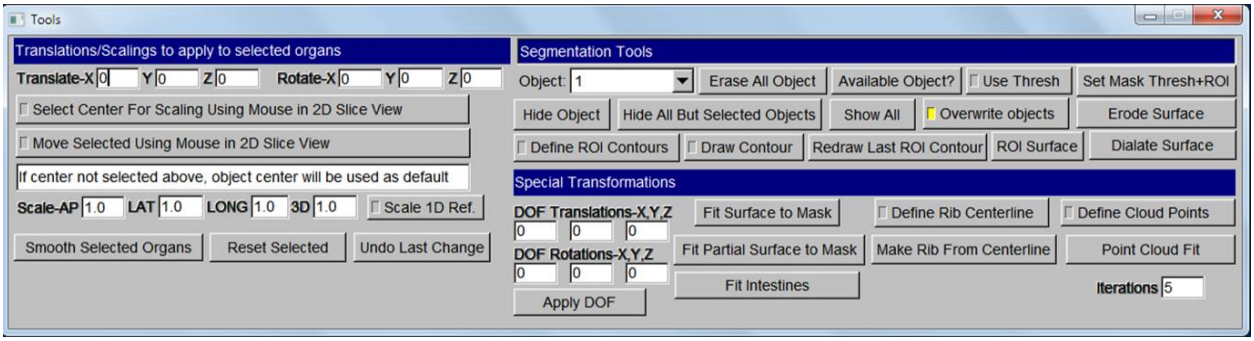

Figure IV.6: GUI of surface transformation tools.

Transformation Algorithms

Affine Transformations

Modification of organ models by affine transformation is performed by applying a transformation matrix to the control points (see equation IV.4). The affine transformations available in Phantom Morphus include translation, rotation and scaling. These transformations can be applied to multiple structures at the same time by selecting them in the "Phantom Structures" window. Translation of surfaces in a specific direction, denoted as *x*, *y*, and *z* in the "Tools" window, is performed by simply translating the coordinates of the control points by a user-specified amount. Selected surfaces can also be translated in the 2D slice view using the mouse by clicking and dragging the selected surface overlays to the desired position. Rotation of selected structures is performed about the center each object. The coordinates of the control

points are rotated in the selected plane about this center point. The anterior-posterior plane is designated as the *x* direction, the lateral plane as the *y* direction, and the longitudinal plane as the *z* direction. Models can be scaled in several different ways. Scaling can be performed in only one dimension about the center of the selected object based on a user-specified scale factor. Scale factors larger than one will dilate the surface in the selected dimension and factors less than one will shrink the surface. The surface may also be scaled in 3D by the scale factor about the center point of the model or a selected center point defined by click the mouse in the 2D image view.

A first order approximation of patient-specific organ anatomy can be achieved by applying affine transformations to the reference organs. Figure IV.7 shows an example of the original left kidney and the modified organ shape using only affine transformations. The kidney was scaled by a factor of 1.1 in the longitudinal direction, rotated -15° about the lateral plane and centered on the patient CT by translation using the mouse in the 2D view.

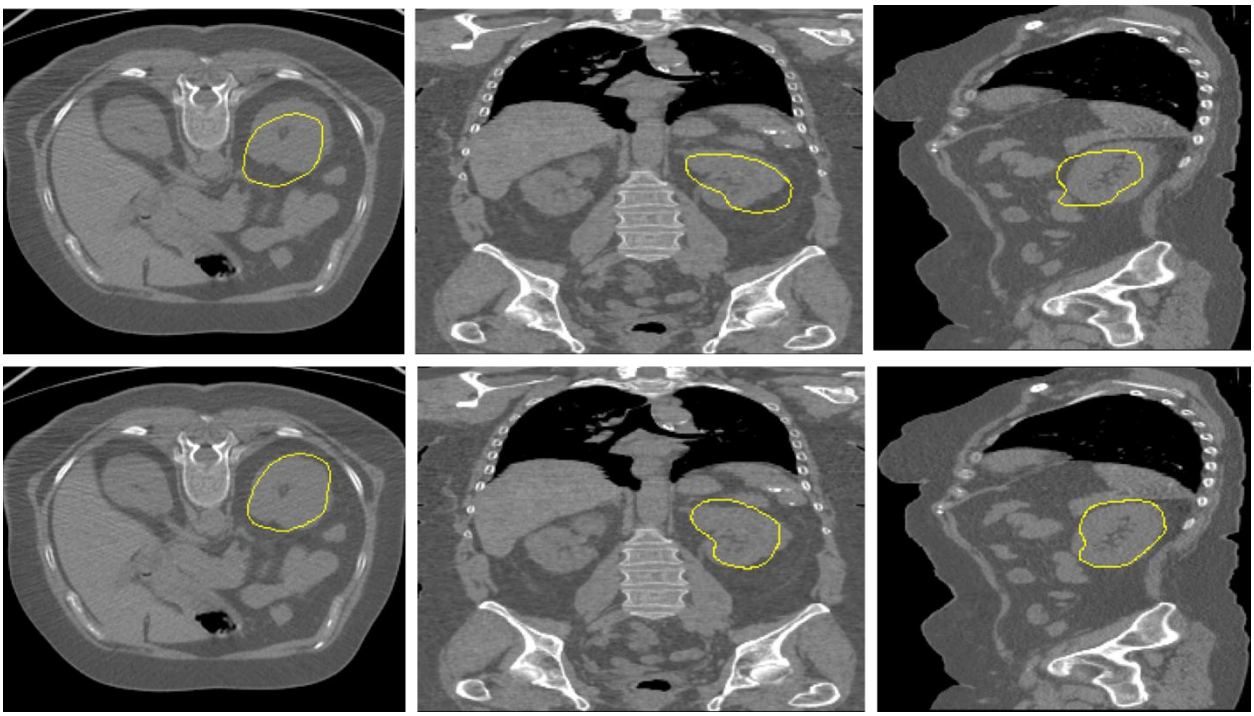

Figure IV.7: Result of organ modification using affine transformation of the left kidney. The top panel shows the original position of left kidney. The bottom panel shows the organ after scaling, rotation and translation. The phantom kidney is shown as a yellow contour in the images.

Surface Fitting to Threshold Mask

Phantom Morphus has the capability of fitting an existing surface to a defined mask. Although this is not different from conventional methods of manual segmentation, it does offer an efficient way to deform surfaces of high contrast with surrounding tissue such as the lungs and body contour. The user first defines ROI contours using the mouse in the 2D image view. The software has the ability to interpolate the contours in the longitudinal plane so the user is not required to manually define the ROI on each image slice. Once the contours are complete, the ROI surface is created using a minimum and maximum threshold of CT intensities set in the "Image View Tools" window. If necessary, the defined ROI can be dilated or eroded to refine its shape. The user then has the option of fitting the entire NURBS surface to the threshold mask or the partial surface that spans the mask. The latter option is especially useful for fitting incomplete body contours or lung volumes to CT images spanning a partial field of view of the patient anatomy commonly encountered in imaging data available in TRT (see Chapter 5 for examples).

Surface Fitting to a Point Cloud

Many methods to fit NURBS curves and surfaces to a set of measured data points have been developed (Brujic et al. 2011, Brujic et al. 2002, Cheng et al. 2004, Flöry & Hofer 2010, Pottmann & Leopoldseder 2003, Ristic et al. 2004, Wang et al. 2006). This process, known as reverse engineering, is especially important in computer-aided design. Most approaches employ least-squares optimization of a defined function relating the distance between each measured point and the closest point on the NURBS surface, denoted as the "foot point". The algorithm developed to fit a surface to a point cloud for the Phantom Morphus software utilizes point distance minimization (PDM) that essentially solves a set of generalized normal equations to

minimize the sum of the squares of the distance between the base surface and the measured data (Brujic et al. 2011, Brujic et al. 2002). The surface fitting algorithm consists of three main steps: point inversion to determine the corresponding surface parameter values (u, v) of the foot point for each point in the point cloud, setting up the system of linear equations including the introduction of additional criteria to regularize the system and ensure the overall minimization problem is well posed, and solving the linear system using an iterative least squares algorithm. These steps are iterated using the updated surface until a tolerance or iteration limit is reached.

Point inversion is performed using a second order geometrical algorithm (Hu & Wallner 2005). The iterative algorithm projects the point onto a curvature circle using an initial guess for the foot point (see Figure IV.8). This projection is used to update the surface parameter values (u, v) of the foot point until convergence is reached. The point projection requires a good initial guess of surface parameter values. We have implemented the method of surface patch elimination in Ma and Hewitt (Ma & Hewitt 2003) to obtain the initial guess. This approach exploits the convex hull property of NURBS surfaces to excluded surface regions. The surface is first subdivided into Bézier patches (defined below). Using the geometrical relationship between the cloud point and the control point net of each Bézier patch, candidate patches are identified and used to obtain the initial surface parameters (u, v) of the foot point.

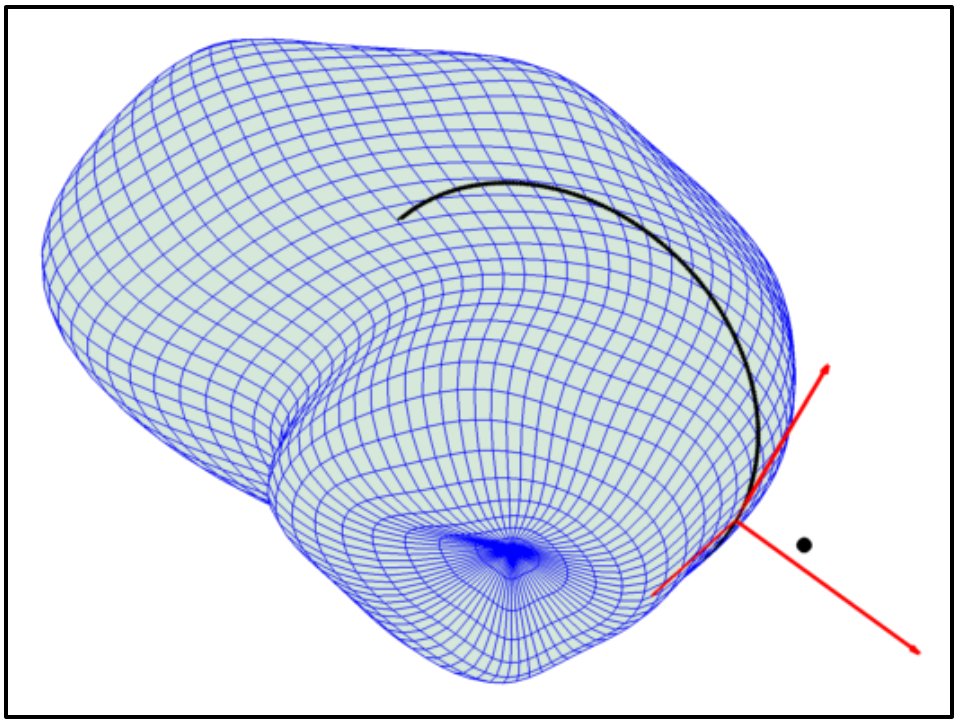

Figure IV.8: Example iteration of point inversion algorithm. The cloud point (black dot) is projected onto the curvature circle (black curve) to update the surface parameters corresponding to the foot point. The red arrows indicate the tangent and normal vectors at the current surface point.

A Bézier patch is similar to a NURBS surface, defined by a set of control points weighted by Bezier basis functions:

$$\boldsymbol{Q}(u,v) = \sum_{i=0}^{n}\sum_{j=0}^{m} \boldsymbol{P_{ij}} B_{i,n}(u) B_{j,m}(v) \qquad \text{IV.5}$$

The basis functions, or Bernstein polynomials, are defined by:

$$B_{i,n}(u) = \frac{n!}{i!\,(n-i)!} u^i (1-u)^{n-i}$$
$$B_{j,m}(v) = \frac{m!}{j!\,(m-j)!} v^j (1-v)^{m-j} \qquad \text{IV.6}$$

with n and m the degrees of the polynomials in the u and v directions, respectively. The main difference between a Bézier patch and a NURBS surface is that the control point net of Bézier patch has only $(n + 1)(m + 1)$ control points. For a cubic Bézier patch, there are a total of 16

control points. The surface of the Bézier patch ***Q*** passes through the control points at the four corners, with $\mathbf{Q}(0,0) = \mathbf{P}_{00}$, $\mathbf{Q}(0,1) = \mathbf{P}_{01}$, $\mathbf{Q}(1,0) = \mathbf{P}_{10}$, and $\mathbf{Q}(0,0) = \mathbf{P}_{11}$.

NURBS surfaces can be subdivided into multiple Bézier patches using knot insertion (Piegl & Tiller 1997). Given a NURBS surface of degree p and q (see equation IV.1), the Bézier patches are obtained by inserting interior knots in until each knot in **U** has multiplicity p and then until each knot in **V** has multiplicity q. Once the surface is subdivided, each Bézier patch can be tested to determine if the foot point is located within the patch, by discarding any patches which the closest surface point to the cloud point is on one of the four boundary curves (see Figure IV.9). Once the closest Bézier patch is located, the midpoint of the (u, v) span for this patch is used as the initial guess in the point inversion algorithm.

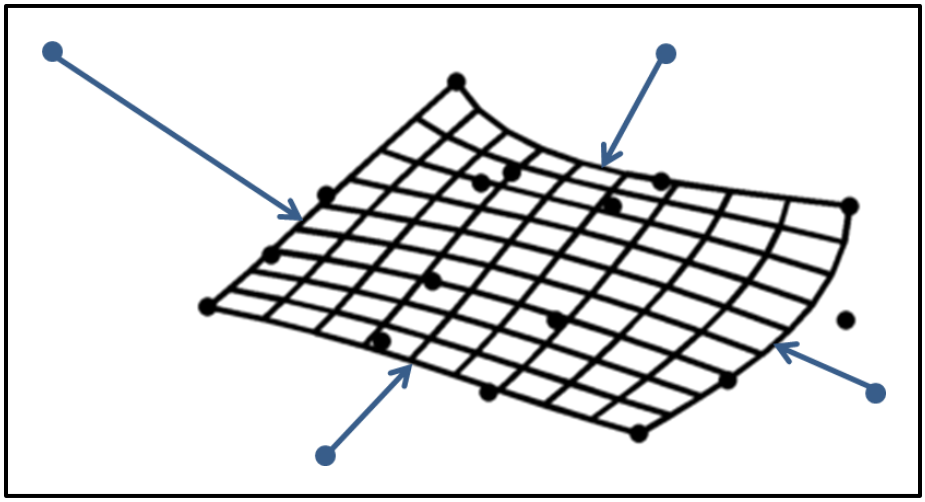

Figure IV.9: Eliminated Bézier patch. Closest surface points lay on the boundary curves.

Fitting a NURBS surface to a series of points becomes a linear optimization problem under the assumption that the weights and knot vectors are fixed and only the control points are unknown. The function for minimization is defined by equation IV.7 with $\mathbf{Q}_k$ representing each cloud point with the corresponding closest surface point given by $\mathbf{S}(u_k,v_k)$ and f_s is a

regularization term to prohibit rank-deficiency or an ill-conditioned system and ensure a smooth surface.

$$f = \frac{1}{2}\sum_{k=1}^{M} \|\boldsymbol{Q_k} - \boldsymbol{S}(\boldsymbol{u_k}, \boldsymbol{v_k})\|^2 + \lambda f_s \qquad \text{IV.7}$$

The point cloud minimization algorithm in Phantom Morphus includes two regularization terms modulated by separate weights (α and β). The first regularization term is generated by the assumption that control points approximate the shape of the surface by the convex hull property and should stay close to the surface (Brujic et al 2011). Mathematically this term is expressed as:

$$f_1 = \sum_{i=0}^{n}\sum_{j=0}^{m} \left\|\boldsymbol{P_{i,j}} - \boldsymbol{S}(\boldsymbol{u_{i,j}}, \boldsymbol{v_{i,j}})\right\|^2 \qquad \text{IV.8}$$

where $\boldsymbol{P_{i,j}}$ are the control points and $\mathbf{S}(u_{i,j},v_{i,j})$ are the corresponding surface points. The parametrization points $u_{i,j}$ and $v_{i,j}$ are determined using Greville abscissae (Milroy et al. 1995). The second term regularizes the surface curvature by applying a discretized version of the Laplacian to the control points in both parametric directions (u and v) (see equation IV.9).

$$P_{i,j} = \frac{1}{4}\left(P_{i-1,j} + P_{i+1,j} + P_{i,j-1} + P_{i,j+1}\right) \qquad \text{IV.9}$$

The linear system of equations determined by evaluating the basis functions of $\mathbf{S}(u_k,v_k)$ and $\mathbf{S}(u_{i,j},v_{i,j})$, and the discretized Laplacian is sparse. The software solves for a new set of control point positions using the LSMR algorithm for sparse least squares problems (Fong & Saunders 2011) using modulation weights α and β of 0.5 and 0.1 respectively. The surface model is then updated and these steps are repeated until the system converges or a maximum number of iterations are completed.

One of the key factors in the success of the PDM algorithm is the ability to choose an initial surface that is a good approximation to the point cloud of measured data. The anatomy of the

reference phantom provides a template for organ geometry that makes surface fitting using PDM an efficient method for patient-specific anatomical modeling. Although this approach still relies on user interaction, defining organ and tumor volumes via point cloud fitting only requires the user to only select a set of surface points that are representative of the overall shape compared to time-intensive slice-by-slice contouring.

Fit Intestines with Vector Field Transform

Digestive organs are complex in morphology, with many twists and turns, and change temporally during the course of a patient's treatment. The complexity of their shape makes them difficult to deform to match the patient anatomy. We have implemented a method to fit reference organs to the general shape of the small intestines, colon, and rectum of the patient using a vector field transform. The NURBS template model includes two boundary surfaces that completely enclose the bowel. Using the methods described above, the user deforms one of these surfaces to match the complete boundary of the intestines and rectum using the CT image as a reference. The differences between the two boundary surfaces are used to calculate field motion vectors that represent the necessary transformation from a point on the original boundary to the correspond point on the patient-specific boundary. These motion vectors are then applied to each of organ models to shift the control point locations to fit the intestines inside the patient abdomen. Although this approach does not account for exact differences between the surfaces of reference phantom and patient bowel, it does provide an estimate of where the small intestines, colon and rectum are positioned relative to the other organs in the abdominal cavity of the patient.

Construction of Patient-Specific Models

The workflow to construct patient-specific models using the Phantom Morphus software is a top down approach. The process begins with coarse alignment of the entire phantom to the body, first in the transverse plane and then in the coronal and sagittal views, using the base of the lungs as a reference landmark. Once general alignment is achieved, the next step is to scale the body trunk in each dimension. It is important to not scale the body based on the external body contour, especially if the patient is overweight or obese, but with respect to the internal organs. This can be achieved by using the rib cage as a reference in the anterior-posterior and lateral directions and the length of the spinal column in the longitudinal plane.

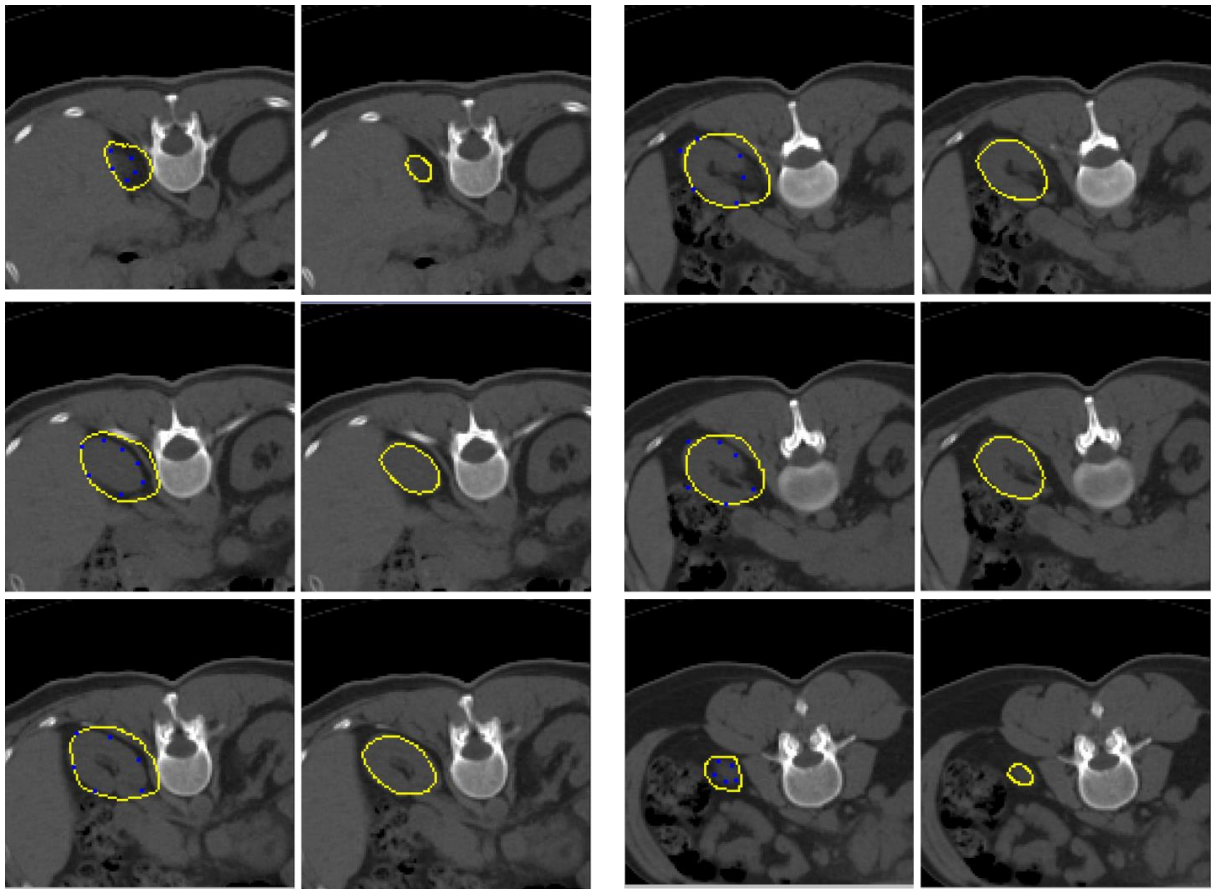

Figure IV.10: Example of data point selection and results for surface fitting to a point cloud. Each pair of images represents one set of results. The left image in each pair shows the original phantom kidney contour along with the point cloud to fit. The right image in each pair shows the resulting contour of the fitted phantom kidney.

The next step is to modify each organ to match the patient anatomy. The NURBS surface can be centered by over the organ using the "click and drag" function. Once centered, the user can scale and rotate the surface in each dimension to improve the alignment. Often, using these affine transformations may result in a suitable organ volume. If refinement is required, the point cloud surface fit algorithm can be applied. The user selects points along the organ boundary on the CT. This should be done at each end of the organ and on a subset of slices between the ends (see Figure IV.10). Areas of high curvature require more densely defined points. The user specifies the number of times the least squares fitting is performed (default = 5). Larger and complex surfaces require more iterations to achieve acceptable results.

The right and left lungs can be matched to the patient anatomy by fitting the NURBS surfaces to a masked defined by a threshold or by using the point cloud surface fitting algorithm. Because all NURBS surfaces in the reference phantom are closed at both end points, both lung surfaces actually extend down past the base in order include the area in the base of the lungs at the position of the diaphragm (see Figure IV.11a). In the transverse view, the right lung will have significant overlap with the liver and the left lung will continue down into the spleen and stomach. These overlaps will be handled during the voxelization process as the organs are converted in a specific order. Thus, the liver surface will replace the areas of right lung that coincide. Because there is significant mediastinum between the base of the left lung and the top of the spleen and stomach, the excess lung surface is corrected by placement of a NURBS surface representing the left diaphragm. Once the left lung is deformed to match the patient, the left diaphragm should be adjusted at the lung base. During voxelization, the left diaphragm is voxelized as body and then areas that overlap with the spleen and stomach replace those voxels (see Figure IV.11b).

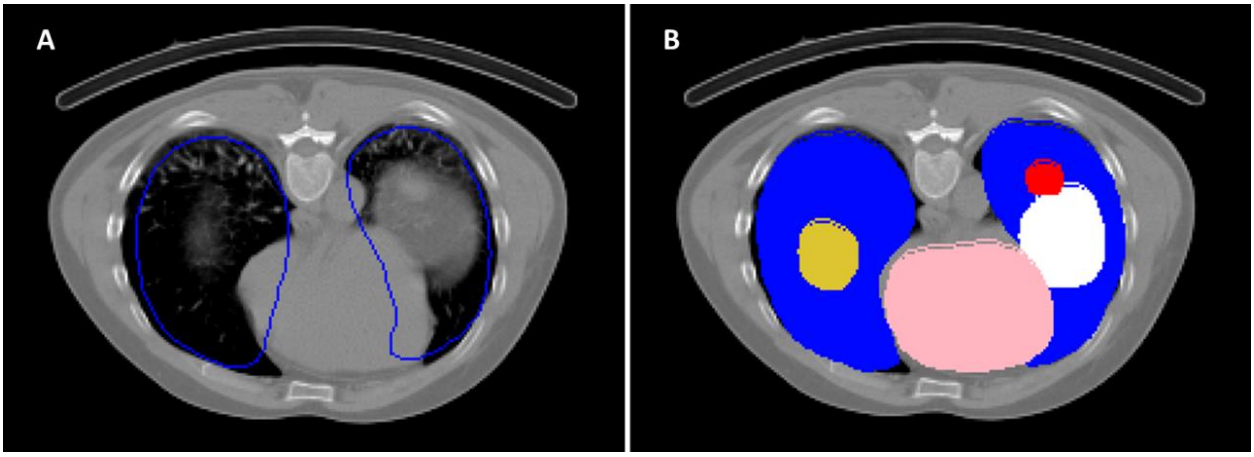

Figure IV.11: Overlap of the lungs at the base before deforming structures to match the patient (a) and after modification (b). The white area is the left diaphragm that is voxelized as body and replaced by other organs including the spleen (red), stomach and heart (pink).

The small and large intestines cannot be deformed with the point cloud surface fit algorithm. In order to accurately represent the bowel loops and avoid self-intersection of the surface, the small intestine is comprised of a series of NURBS surfaces. Likewise, parts of the large intestines, namely the transcending and sigmoid colon, consist of more than one NURBS surface. The abdominal anatomy of the patient can be approximated in one of two ways. The user can apply a vector field transform to these organs by first delineating a boundary surface around the entire bowel. This algorithm requires the entire bowel to be visible in the patient CT. The alternate method for creating patient-specific abdominal organs is to use affine transformations to estimate the size and position of the small and large intestines.

Definition of the patient's skeleton is achieved by applying affine transformations to individual or groups of bones in the phantom. Additionally, the user can create patient-specific ribs by using an algorithm that fits a NURBS surface to a center line through each rib defined by the user on the image. Depending on the image size, the task of modifying each bone to match the patient may be tedious and lengthy. If this process is time-prohibited, the skeleton can be added to the 3D organ map after voxelization by identifying voxels containing bone using a

threshold mask. The bone voxels can then be modeled as whole bone during MC simulation. The definition of each bone surface using the NURBS model has one advantage. The voxelization process can be modified to insert marrow cavities inside each bone. Using a few anatomical measurements on the patient CT, patient-specific active marrow mass in each bone can be estimated (Pichardo et al. 2007) and used to populate voxels in the cavity as red marrow. Then dosimetry can be performed using VIDA with a skeleton that contains separate cortical bone, yellow and marrow voxels. This approach provides a method to estimate red marrow dose that is not easily performed when the skeleton is modeled as whole bone. Often, red marrow toxicity is a concern in TRT and the ability to measure energy deposition in voxels specified as red marrow during MC simulation may offer improved dose estimates to this radiosensitive organ compared to currently available approaches such as fixed geometry dosimetry based on measuring radioactivity levels in blood after treatment (Forrer et al. 2009).

The final step in creating a patient-specific NURBS model is to fit the body contour. The reference NURBS phantom has separate surfaces representing the trunk, right and left arms, and right and left legs. The fastest way to deform these surfaces to match the patient is to fit either the whole surface or partial NURBS to a mask. The body contour mask can be quickly created by applying a threshold to user-defined ROI contours. These contours are drawn on a subset of the CT slices, with interpolation performed between each one to achieve a continuous mask (see Figure IV.12).

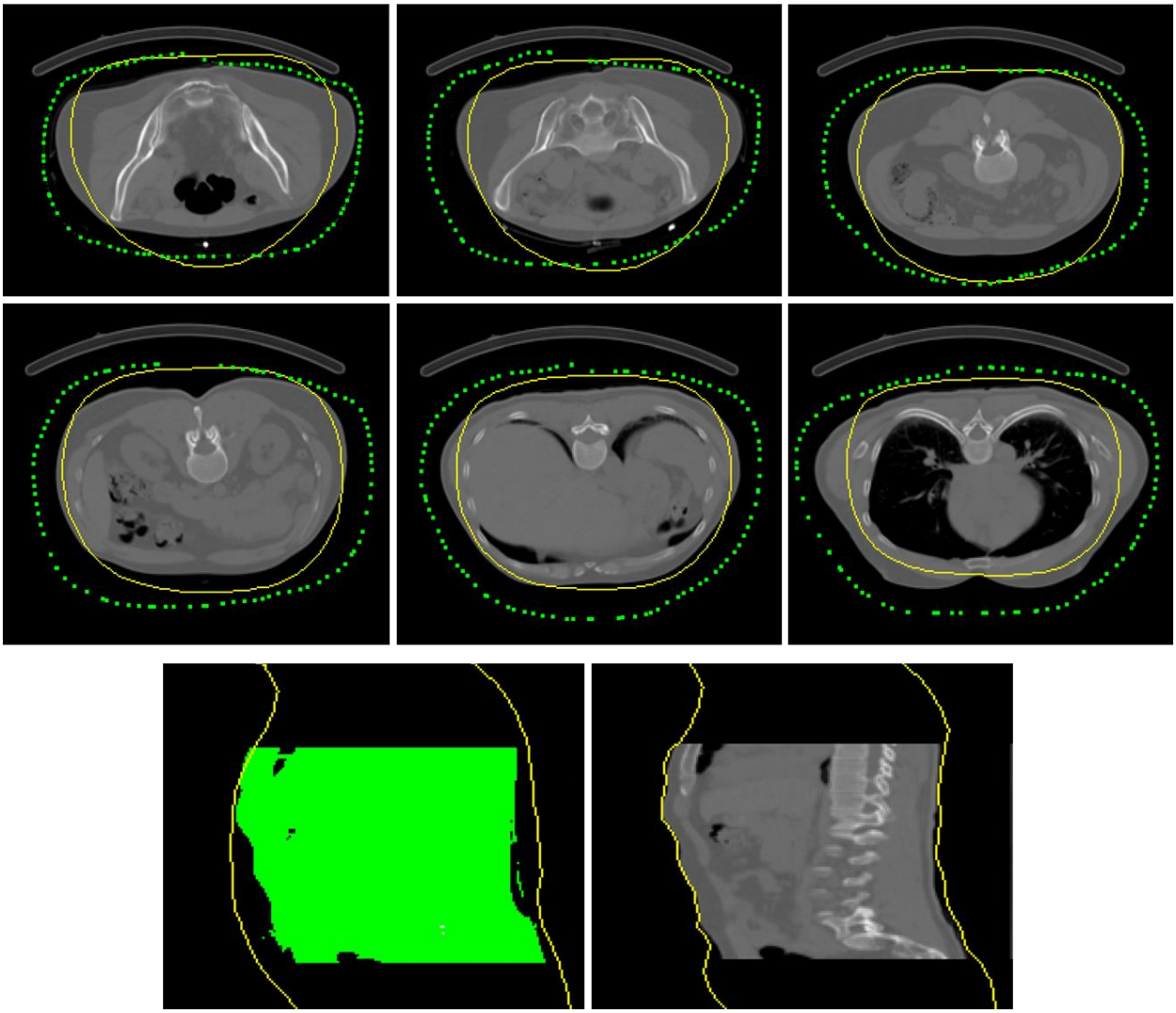

Figure IV.12: Example of fitting the body contour to the patient. The ROI contours are defined approximately every 20 slices in the axial view (top). The surface mask is created using a threshold range of CT intensities and interpolated in the longitudinal direction (lower left). The partial NURBS surface is fit to the mask (lower right).

Validation

Introduction

Techniques for image segmentation require appropriate validation, especially if the results will be used in patient treatment. There is a long history of the use of standard test images for image validation, dating as far back as 1974 with the development of the Shepp-Logan head phantom for testing of CT image reconstruction algorithms (Shepp & Logan 1974).

Segmentation standards have been created for various regions of the body including the brain (Aubert-Broche et al. 2006, Collins et al. 1998) and lung (Armato III et al. 2004) to validate interactive, semi-automatic and automatic segmentation methods. Typically these standards are generated using high-resolution images of individual patients or realistic simulated anatomical volumes.

The primary difficulty in quantifying the performance of medical image segmentation techniques is the lack of ground truth for *in vivo* data. Interactive drawing of volumes of interest by experts is often the gold standard for segmentation in clinical practice, as in the case for TRT. Therefore, we chose to validate the construction of patient-specific deformable models using a set of manually-segmented high-resolution CT images. PET/CT data was selected because the large field of view included all organs of interest to TRT. Additionally, the inclusion of the PET data facilitated the investigation of how patient-anatomy defined by deformable NURBS impacts the dosimetry.

In this section, we present the validation of patient-specific NURBS models constructed using the methods described previously in this chapter. Patient-specific models were built and compared to manually-segmented organs verified by a radiologist with experience in body CT. Several evaluation metrics were applied, including volume differences, set similarity coefficients of spatial overlap, and Euclidean distance between surfaces. 3D imaged-based dosimetry was also performed using VIDA to assess the relevance of volume misfits between deformable models and patient anatomy to organ dose.

Methods

Patient Data

Four adult patients, two male and two female, who had undergone an ^{18}F-FPEB dosimetry study for a new radioligand that binds to the metabotropic glutamate receptor subtype 5 (Kessler et al. 2014) were chosen from our archives. The ^{18}F-FPEB study received approval from our institutional review boards and all subjects the provided written informed consent before enrollment. All images were anonymized prior to use in accordance with the Health Insurance Portability and Accountability Act (HIPPA). Patient demographics and anthropometry are presented in Table IV.1.

Table IV.1: Description of patients used in deformable model validation

Patient	Sex	Age (yr)	Height (m)	Weight (kg)
1	F	19	1.65	72
2	F	52	1.68	84
3	M	23	1.65	77
4	M	22	1.80	72

The PET/CT studies include high resolution CT images ($1.37\times1.37\times3.27$ mm^3) with a field of view spanning from the top of the skull down to the mid-femur. Patient anatomy was defined using a combination of manual and semi-automatic segmentation techniques included in the ITK-SNAP toolkit (Yushkevich et al. 2006). Organ volumes were verified by a subspecialty radiologist with experience in both body CT and nuclear medicine. Likewise, patient-specific NURBS models were created using the CT image as a template for deformation using the process described in the previous section. The manually-segmented standards and deformable models included all trunk organs, ranging from the heart and lungs in the upper chest to the reproductive organs in the lower pelvis.

Evaluation Metrics

Three evaluation metrics often used to assess image segmentation results of the same structure were chosen to evaluate the organ volumes in the patient-specific NURBS models (Van Ginneken et al. 2007). The organs volumes from manual segmentation using were set at the reference or "ground truth" for this analysis. First, the volumetric error of each organ was calculated as the relative percent difference between the total target and reference volumes. Over-definition of the NURBS organ is indicated by a positive difference and under-definition is given by a negative value. The Jaccard similarity metric (Jaccard 1912) was used to determine the percent volumetric overlap. The Jaccard similarity coefficient (J) is defined as the size of the intersection divided by the size of the union of the sample sets (A and B) (see equation IV.10).

$$J(A,B) = \frac{|A \cap B|}{|A \cup B|} \qquad \text{IV.10}$$

The average surface distance between the two organs was calculated using Euclidean distance mapping (Danielsson 1980, Mishchenko 2015). Surface boundaries of the reference and target volumes were delineated and for each voxel in the target the distance to closest voxel to the reference boundary was determined. The average of all these distances was tallied to produce a metric of the average symmetric absolute surface distance between the segmented and NURBS organ. These evaluation metrics were applied to the entire body contour and skeleton to assess the global accuracy of the patient-specific NURBS models. Individual organs of importance to dosimetry in TRT were evaluated including lungs, heart, liver, spleen, kidneys, and gall bladder.

Dosimetry

To assess the impact of discrepancies in the patient-specific model anatomy on dosimetry, organ maps were generated from the individualized phantoms and used as input into VIDA to obtain dose rate maps. NURBS models were voxelized at resolution of the PET images

(5.47×5.47×3.27 mm^3). The voxelization program assigns organ ID numbers to each voxel as specified in an input parameter file. The integer IDs were assigned to organs to match those used in VIDA (see Appendix D). Overlapping surfaces (e.g. liver and right lung) are handled based on a priority value assigned to each organ. For voxels corresponding to surface overlap, the voxel is assigned the ID number of the organ with the highest priority. These results were compared to dose rate maps generated by VIDA for the reference anatomy using manually-segmented organ maps. In order to match the resolution of the PET images, the organ maps created using manual segmentation methods were down-sampled from 512×512 pixels to 128×128 pixels in the transverse plane with nearest neighbor interpolation of the organ identification numbers.

VIDA was run using ^{131}I as the radionuclide to assess the locally-deposited dose from charged beta particles and dose due to penetrating radiation from gamma emission. Approximately 10 million primary decay events were simulated, distributed non-uniformly specific to voxel-level PET activity for the patient. The simulated field of view covered the complete torso from above the apex of the lung to the bottom of the ischium in order to estimate dose to most radiosensitive organs. The skeleton was modeled as whole bone (see Table III.1).

Results

Patient-specific NURBS models and the corresponding manually-segmented reference models are shown in shown in Figure IV.13. The results from applying the evaluation metrics to individual volumes of interest are summarized in Table IV.2. Mean and standard deviations of the evaluation metrics for each organ across all patients are presented in Table IV.3. With the exception of the gall bladder and the distributed skeleton, most NURBS organ volumes differ less than 10% on average compared to the manually-segmented structures. The average

Euclidean distance between surface boundaries ranged from 1.3 to 3.8 mm, corresponding to a separation of approximately 1 to 3 voxels.

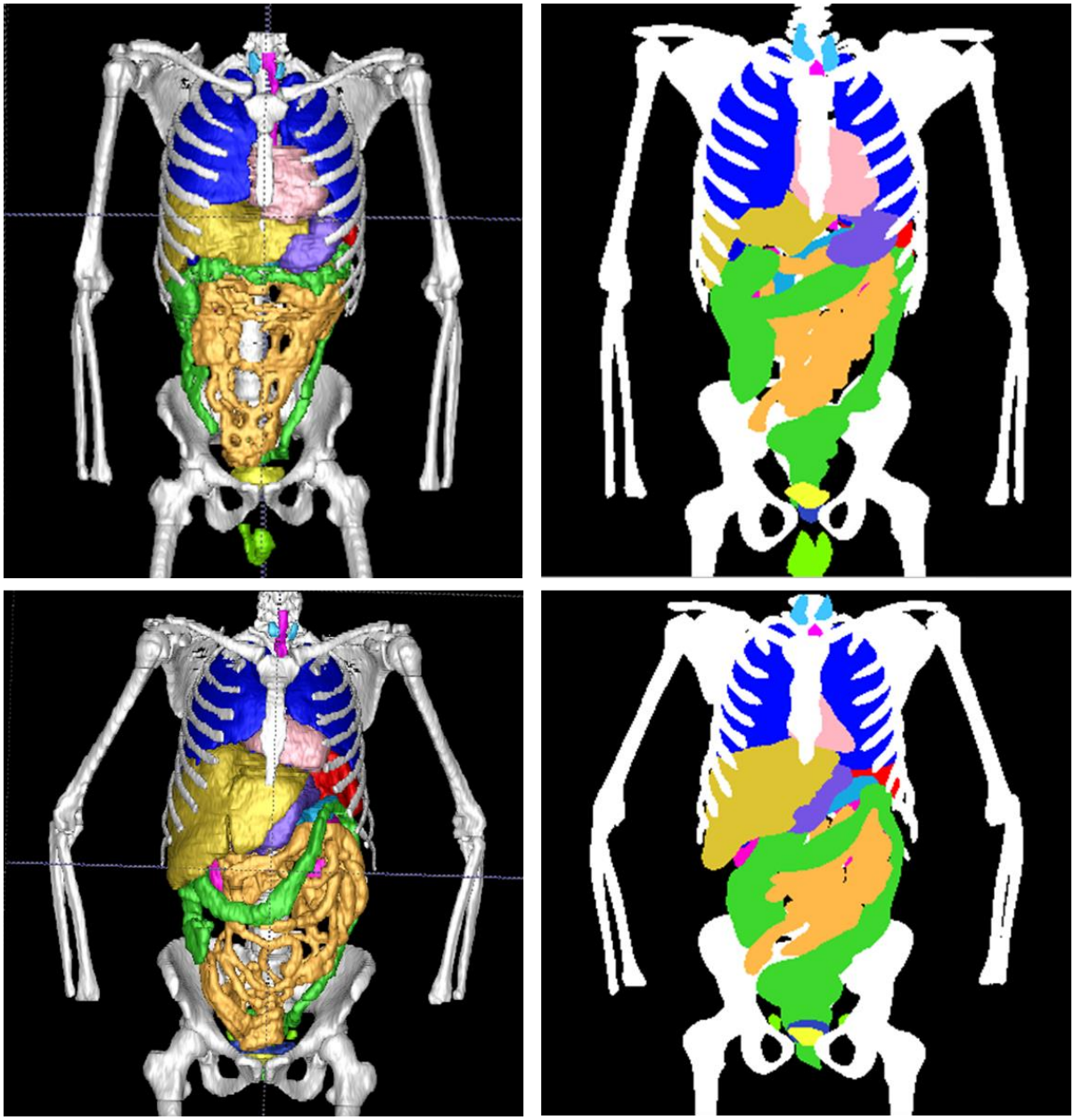

Figure IV.13: Example patient-specific NURBS model and reference manual segmentation for (b) male and (b) female patients. The opaque body contours and breasts are not shown.

Table IV.2: Evaluation metrics for patient-specific deformable models

Organ	Volume Diff. (%)	Volume Overlap (%)	Avg. Distance Error (mm)	Volume Diff. (%)	Volume Overlap (%)	Avg. Distance Error (mm)
	Patient 1			Patient 2		
Body	2.7	94.6	2.0	2.4	94.4	2.6
Skeleton	28.0	53.1	2.4	12.0	47.6	3.6
Gall Bladder	56.0	58.8	2.7	71.5	54.4	2.6
Heart	-10.7	74.3	1.9	9.2	78.3	2.7
Kidneys	5.2	82.7	1.3	0.0	82.6	1.5
Liver	1.7	88.6	1.5	1.5	86.9	1.9
Lungs	13.1	80.3	1.9	5.9	84.6	1.9
Spleen	7.0	79.4	1.8	7.0	81.5	1.7
	Patient 3			Patient 4		
Body	5.5	90.4	3.8	0.0	93.7	2.2
Skeleton	12.0	53.4	2.1	21.5	49.9	2.5
Gall Bladder	3.4	45.8	2.9	39.5	62.4	1.8
Heart	10.0	78.9	2.3	-1.6	78.9	2.1
Kidneys	0.8	83.2	1.3	8.8	79.4	1.5
Liver	-15.5	71.2	3.7	4.7	82.5	2.2
Lungs	6.6	83.6	2.1	9.7	85.4	1.8
Spleen	-4.9	68.6	2.2	-9.9	82.6	1.6

Table IV.3: Mean evaluation metrics for each organ

	Volume Diff. (%)	Vol. Overlap (%)	Avg. Distance Error (mm)
Body	2.7 ± 2.2	93.3 ± 2.0	2.6 ± 0.8
Skeleton	18.4 ± 7.8	51.0 ± 2.8	2.7 ± 0.6
Gall Bladder	42.6 ± 29.2	55.3 ± 7.2	2.4 ± 0.4
Heart	7.9 ± 4.2	77.6 ± 2.2	2.2 ± 0.3
Kidneys	3.7 ± 4.1	81.7 ± 1.7	1.4 ± 0.1
Liver	5.8 ± 6.6	82.3 ± 7.8	2.3 ± 1.0
Lungs	8.8 ± 3.3	83.5 ± 2.2	1.9 ± 0.1
Spleen	7.2 ± 2.0	78.0 ± 6.4	1.8 ± 0.3

Relative percent differences in organ doses using the patient-specific NURBS model compared to manually-segmented organ volumes are given in Table IV.4. With the exception of lung, the mean absorbed doses calculated from the NURBS models agree with results from manually segmented volumes to within 10%.

Table IV.4: Comparison of organ absorbed doses calculated from patient-specific NURBS models and manually segmented CT data expressed in relative percent differences

Patient	Heart	Lung	Liver	Kidney	Spleen	Skeleton
1	5.7	20.3	-1.1	3.2	-0.6	-2.0
2	1.1	3.4	-1.0	1.4	-2.4	-4.1
3	0.2	18.2	6.8	-0.4	0.1	0.7
4	-5.7	8.0	-3.8	1.2	1.0	-2.7

Relative difference defined as $100 \times (D_{NURBS} - D_{Manual}) / D_{Manual}$.

Discussion

The creation of patient-specific NURBS models was evaluated using a set of manually segmented patient CTs. Whole body patient models were created in a few hours, resulting in a marked reduction of time compared to user-guided manual and semi-automatic segmentation of the CT. The ability to convert the NURBS surfaces to a 3D array of voxels at any resolution allows these models to be used in image-based dosimetry applications.

Overall, the organ volumes from the patient-specific NURBS models agree with manually segmented structures on average to within 10%. Two exceptions are the gall bladder and lungs. The gall bladder is a small organ that is susceptible to large percent volume differences; however, the gall bladder is rarely a concern as an organ at risk in TRT. In all the patients, the lung volumes in the NURBS models are larger. The over-definition of the lungs is most likely due to the inclusion of the bronchi within the NURBS surface. These were excluded from the manual segmentation but the NURBS surfaces for the lungs are smooth and do not have the level

of complexity required to shape the surface around the bronchi. Previous studies (e.g. Hermoye et al. 2005) have reported that variation in organ volumes manually segmented by experts can differ by upwards of 20%, and that these volumes differ with truth by an average of 12%. The difference in organ volumes using a deformable NURBS phantom compared to manually segmented organs are consistent with differences that may occur between slice-by-slice segmentations performed by two different experts.

Comparison of organ volumes does not provide any information about the position of the NURBS surfaces in relation to the manually-segmented structures. The Jaccard coefficient is a statistic used to assess similarity between samples and was used to determine the percentage of volume overlap between NURBS surfaces and manually-segmented organs. With the exception of the gall bladder and skeleton, the NURBS organs overlap with manually defined organs by 78% or more. The dissimilarity in gall bladder overlap is related to the large volumes in the NURBS models, which is on average almost 50% larger than manually-segmented volumes. The NURBS skeleton also showed poor alignment compared to bones that were defined semi-automatically using the snake evolution in ITK-SNAP. There are two factors that may contribute to the variation in skeletons. One, only affine transformations were applied to the NURBS bones to create a patient-specific skeleton. Bone shape and curvature may vary between the reference phantom and the patient. One notable example is the pelvis, which is larger and broader in women. Using a hermaphroditic reference phantom generated from male anatomy may contribute to the inaccuracy of modeling the female pelvis. Also, some of the bones in the NURBS phantoms fail to adequately represent the complex skeletal anatomy, including the scapulae and sacrum. The NURBS model of the sacrum does not include space for the sacral canal and foramina. Similarly, the surface representing the scapula does not model the curvature

of the coracoid process and acromion and overestimates the thickness of the infraspinous fossa. These differences may explain the volume of the NURBS skeleton is 10-25% larger compared to manually-segmented bones and percent volume overlap is less than 50%.

The average Euclidean distance from each NURBS organ boundary to the manually-segmented volume was determined. Overall average distance errors for the organs analyzed in this study ranged from 1 to 3 mm. These distances are similar to those calculated for a NURBS-based pediatric phantom created using the automated MC-LDDMM mapping method (Segars et al. 2009). For the high resolution CT images ($1.37\times1.37\times3.27$ mm^3), these distances correspond to differences of 1 to 3 voxels; however they are well contained within a voxel in the activity image ($5.47\times5.47\times3.27$ mm^3). Thus, errors in the position of organs created using deformable NURBS phantoms may not impact the dosimetry results significantly depending on the resolution of the available SPECT or PET images.

Other studies have evaluated CT-based automatic and semi-automatic organ segmentation methods using metrics of percent volume overlap and surface distance error. A survey of image processing techniques for liver segmentation (Campadelli et al. 2009) summarizes results from the literature. Average percent volume overlap compared to manually-segmented livers ranged from 78% to 95% for various methods including model fitting, gray-level based thresholds, and probabilistic atlases. Average surface distances reported ranged from 2 to 2.3 mm. The average percent volume overlap for NURBS-based livers was 84% with average surface distances to manual-volumes of 2.0 mm. Both metrics fall within the ranges reported for other liver segmentation studies. Automatic kidney segmentation using m-rep models was compared to manual segmentation by experts (Rao et al. 2005). For 12 target images, the average volume overlap was 82% with a mean surface separation of 1.8 mm. Our results are similar with an

average percent volume overlap of 82% and distance error of 1.4 mm. One reason for the difference between the NURBS kidneys and manually-segmented volumes is the inclusion of parts of the renal vein, artery, and pelvis in the NURBS structure that were not identified in the kidney volumes during manual segmentation. Nonetheless, the results of evaluating organ volumes of patient-specific NURBS compared to slice-by-slice manual definition are similar to outcomes from other automatic and semi-automatic CT-based segmentation methods.

The impact of using patient-specific NURBS models on organ doses from internal emitters was also assessed. The patient-specific NURBS models created in this study were voxelized at the resolution of the PET activity data and used to define anatomy during MC simulation using VIDA. Although this activity represents the uptake of ^{18}F, organ doses were estimated by MC simulation assuming ^{131}I, a radionuclide commonly used in TRT. The rational of using ^{131}I instead of ^{18}F was to assess dose to organs from a radionuclide that emits both short-ranged beta particles and gamma rays that deposit dose at larger distances. ^{18}F decays mainly through positron emission and the high energy annihilation photons do not deposit as much dose compared to the beta-emitting radionuclides used in TRT. In general, the organ doses from the NURBS models are within 10% of those generated using manually-segmented organ maps with the exception of lung dose in patients 1 and 3. The lungs have low uptake of ^{18}F-FPEB and the increased lung doses in the patient-specific NURBS models could be due to the erroneous inclusion of high-activity pulmonary veins and arteries and liver in the NURBS surfaces defining the lungs. We conclude that using deformable NURBS to define patient anatomy does not contribute to the uncertainty in dose estimates to a greater extent than other factors such as accuracy in activity quantification and statistical error from MC simulation.

Summary

We have developed a new method for creating patient-specific models by deforming a NURBS-based anthropomorphic reference phantom. The software creates an interactive environment for the user to easily transform organ models using patient CT data as a guide. Models of patient anatomy ranging from the shoulders down to the bottom of the pelvis can be created in a few hours. Using deformable models significantly reduces the time required to outline patient anatomy compared to conventional manual and semi-automatic segmentation. This chapter has demonstrated a preliminary method for creating NURBS-based patient-specific models for use in dose optimization for TRT.

Currently, the software employs a single reference phantom representing a 50^{th} percentile person. Substantial modifications to the reference anatomy may be required depending on the height and weight of the patient. NURBS-based reference phantoms of larger and smaller normal stature (Marine et al. 2010) and different levels of obesity (Clark et al. 2010) have been developed. The process of creating patient-specific NURBS models described in this chapter may be expedited by matching the patient to a reference phantom using patient information including height, weight and body-mass index.

Phantom Morphus includes a novel algorithm to fit a reference surface to a point cloud outlining the boundary of the patient organ. This non-rigid transformation exploits the local surface modification property of the model's control points to create an accurate representation of the patient organ. The current algorithm performs a least squares minimization of the distance between cloud points and the surface point. It has been shown that using different minimization schemes such as tangent distance minimization (TDM) and surface distance minimization (SDM) yield faster convergence and prevent the system from becoming trapped in a local

minimum that may create surfaces with self-intersections (Cheng et al. 2004, Wang et al. 2006). Employing SDM in the Phantom Morphus surface fitting algorithm may increase efficiency and produce more accurate surfaces.

CHAPTER V

APPLICATION TO PATIENT STUDIES

Introduction

Understanding tumor response and normal tissue toxicity are vital for successful treatment using TRT. Each patient has different pharmacokinetics and fixed activity protocols result in vastly different doses to both healthy and malignant tissue. Treatment optimization in TRT using image-based3D patient-specific dosimetry requires measuring the spatial distribution of radioactivity over time to obtain an absorbed dose calculation based on administration of a small tracer amount of radioactivity. Measurement of temporally-dependent spatial distributions of radioactivity involves acquisition a set of SPECT/CT or PET/CT images at several time points after administration of the tracer dose. 3D dose rate maps are generated from the time-sequence activity information, which are then integrated to determine the absorbed dose. Predicted organ and tumor doses, along with dose limits to organs at risk and knowledge of tumor-dose response, are used to optimize the therapeutic administered activity.

In this chapter we present results of patient-specific dose calculations two follicular NHL patients treated with ^{131}I-labeled tositumomab (Bexxar®). VIDA was used to predict dose from a tracer study and also determine the actual administered absorbed dose from treatment based on post-therapy imaging. 3D dose maps were obtained using both manually-segmented patient anatomy and from a patient-specific NURBS phantom generated using the techniques described in chapter 4. Results were compared to standard reference doses from RADAR adult phantom and tumor doses from the Dose Planning Method (DPM) MC software (Dewaraja et al. 2009,

Howard et al. 2011, Wilderman & Dewaraja 2007) using the same tumor VOIs in order to minimize error due to differences in segmentation between institutions. The content presented in this chapter is an extension of a paper by S. D. Kost, Y. K Dewaraja, R. G. Abramson and M. G. Stabin, "VIDA: A voxel-based dosimetry method for targeted radionuclide therapy using Geant4", © Mary Ann Liebert, Inc., reprinted with permission, from Cancer Biotherapy and Radiopharmaceuticals, vol. 30, pp. 16-26, 2015 (Kost et al. 2015).

Methods

Patient Data

Individualized dosimetry was performed for two NHL patients treated with ^{131}I-labeled tositumomab (Bexxar®) using multiple SPECT/CT scans. The treatment protocol is summarized here; additional details are described in Dewaraja et al. (Dewaraja). All patients participating in the study provided written informed consent for the additional SPECT/CT scans not included in the clinical protocol.

SPECT/CT images were acquired using a Symbia TruePoint system (Hoffman Esta, IL). Each patient was imaged at three time points after administration of a diagnostic tracer of approximately 185 MBq. Therapeutic doses were administered to deliver a nominal whole-body absorbed dose of 75 cGy based on post-tracer imaging (see Table V.1). Patients were imaged again at three time points post-therapy, with a delay for the first scan of approximately 48 hours due to dead time and exposure considerations (Patient 1, 47.5 hours; Patient 2, 48.58 hours).

Table V.1: Administered tracer and therapy activity and whole body pharmacokinetics.

	Patient 1	Patient 2
Administered tracer activity (MBq)	189	196
Tracer effective half-life (hours)	60	48
Tracer residence time (hours)	40	38
Administered therapy activity (GBq)	3.74	3.43
Therapy effective half-life (hours)	61	46
Therapy residence time (hours)	41	38

SPECT/CT images were acquired with a 128×128 matrix and a pixel size of 4.8 mm using a high-energy parallel-hole collimator. Scatter correction was performed using the triple-energy-window technique. The CT data were reconstructed to an image size of 512×512×196 using commercial software. Quantitative SPECT with an array size 512×512×78 was obtained with a custom 3D OSEM reconstruction algorithm using 35 iterations and 6 subsets. The reconstruction algorithm includes 3D depth-dependent detector-response compensation, attenuation and scatter correction, and dead-time correction for the post-therapy projection data.

Image counts were converted to activity using a calibration factor specific to the SPECT/CT scanner and radionuclide. The calibration factor was obtained from measurement of a 100 ml plastic sphere filled with a known amount of ^{131}I activity placed in an elliptical water phantom. Recovery coefficients for partial volume correction were not applied as tumor and organ volumes were large and there is no widely accepted, well-validated method for voxel-by-voxel compensation. Additional details of image acquisition, reconstruction and activity quantification for this dosimetry study are included elsewhere (Dewaraja et al. 2009, Dewaraja et al. 2005, Dewaraja et al. 2010).

Patient-Specific Anatomical Models

Patient anatomy was defined using two methods. Tumors and normal tissue organs were segmented on the high resolution first post-tracer CT image (512×512×196 matrix, 0.98×0.98×2.0 mm voxel size) using a combination of manual and semi-automatic segmentation techniques included in the ITK/SNAP toolkit (Yushkevich et al. 2006). Organ volumes were verified and tumors were identified by a subspecialty radiologist with experience in both body CT and nuclear medicine. Additionally, patient-specific NURBS models were created using the CT scan from first post-tracer SPECT/CT study following the methods described in Chapter 4. The NURBS phantoms were only used to model patient organs and not to define tumor volumes.

Voxel-based Dosimetry

Dose rate maps at each time point were obtained using VIDA (see Chapter 3). An organ ID map defining different materials for simulation (see Table C.1) was automatically generated from the CT images in a pre-processing step using MATLAB. First, CT images were converted to density maps using a bi-linear fit calibration curve relating HU to material density based on data from Schneider et al. (Schneider). Air was defined for voxel densities less than 0.15 g/cm^3, lung by a range of 0.15 g/cm^3 to 0.61 g/cm^3, soft tissue between 0.61 g/cm^3 and 1.17 g/cm^{3}and whole bone greater than 1.17 g/cm^3. Activity maps were sampled to simulate 20 million events, resulting in relative errors in the deposited energy of less than 1% in whole organs and a maximum of 10% for individual voxels in the tumor and organs of interest. The voxel-tallied energy deposited was converted to absorbed dose using voxel masses derived from the simulation tissue densities (see Table III.1). Instantaneous dose-rate maps per administered activity were generated by scaling the dose deposited in each voxel by the ratio of actual field-of-view activity to simulated activity.

Conversion to 3D Absorbed Dose

Each 3D deposited energy map from the MC simulation was converted to an instantaneous dose-rate map using voxel masses calculated from the materials in Table III.1. CT-based registration of serial dose-rate images was performed with an affine rigid registration algorithm based on maximizing mutual information (Viola & Wells III 1997) developed by the Vanderbilt University Institute of Imaging Science. The CT images were down-sampled to a resolution of 256×256×78 (1.95×1.95×5.0 mm) to match the slice thickness of the SPECT data and to expedite registration. The CT image set of the first post-tracer scan was assigned to be the reference image in the registration algorithm. All other time points were registered to the reference image by first performing CT–CT registration and applying the transformation matrices to the corresponding dose-rate maps.

Voxel-level dose-rate curves were fit to a mono-exponential decay function for both the pre-therapy tracer data and the post-therapy scans using the exponential fitting tool in VIDA. An absorbed dose map with voxel dimensions of 3.9×3.9×5.0 mm^3 (128×128×78 array) was generated using the option to fit a voxel dose curve to all data in the corresponding 2×2×1 cell array of the higher resolution dose-rate maps. This resolution was chosen to improve fit results, decrease processing time, and estimate voxel doses at the resolution of the SPECT camera (full width at half maximum $\leq$ 3.9 mm).

Tumor and Organ Dosimetry

Malignant lymphomas can be highly sensitive to radiation, leading to measurable changes in volume within the first few days of treatment (DeNardo et al. 1998). The effect of tumor regression on absorbed tumor dose was investigated by defining tumor VOIs on the CT at each time point. The average absorbed tumor dose was calculated by fitting the volume-adjusted dose

rate curve. A comparison was made to mean absorbed tumor doses from the DPM MC software (Dewaraja et al. 2009, Howard et al. 2011, Wilderman & Dewaraja 2007) using the same tumor VOIs in order to minimize error due to differences in segmentation between institutions.

Organ dosimetry was performed based on both the manually-segmented images and patient-specific NURBS phantoms. Manually-segmented organ maps were down-sampled to same size of the dose map (128×128×78). Organ maps were also created by voxelizing the NURBS phantoms this resolution. Because tumors were not explicitly modeled in the patient-specific NURBS models, the manually-segmented tumor volumes were added to the voxelized data in a post-processing step. Mean absorbed organ doses were compared to reference doses calculated for the RADAR phantom, with correction for differences in organ mass between patient and reference phantom. Tumor dose-volume histograms were also generated for both the predicted dose using the tracer study results and the actual delivered dose assuming a static initial tumor volume.

Results

SPECT/CT images with tumor outlines and resulting dose maps for each patient are shown in Figure V.1. Between the initial tracer study and the last imaging point post-therapy, significant decreases in both tumor volumes occurred (see Table V.2). When accounting for shrinkage, the tumor dose differed as much as 16% compared to the mean absorbed dose to a static volume. Table V.2 also lists the mean tumor doses with decreasing mass calculated using the DPM MC software. Mean tumor doses from VIDA and DPM agree within 12% or less.

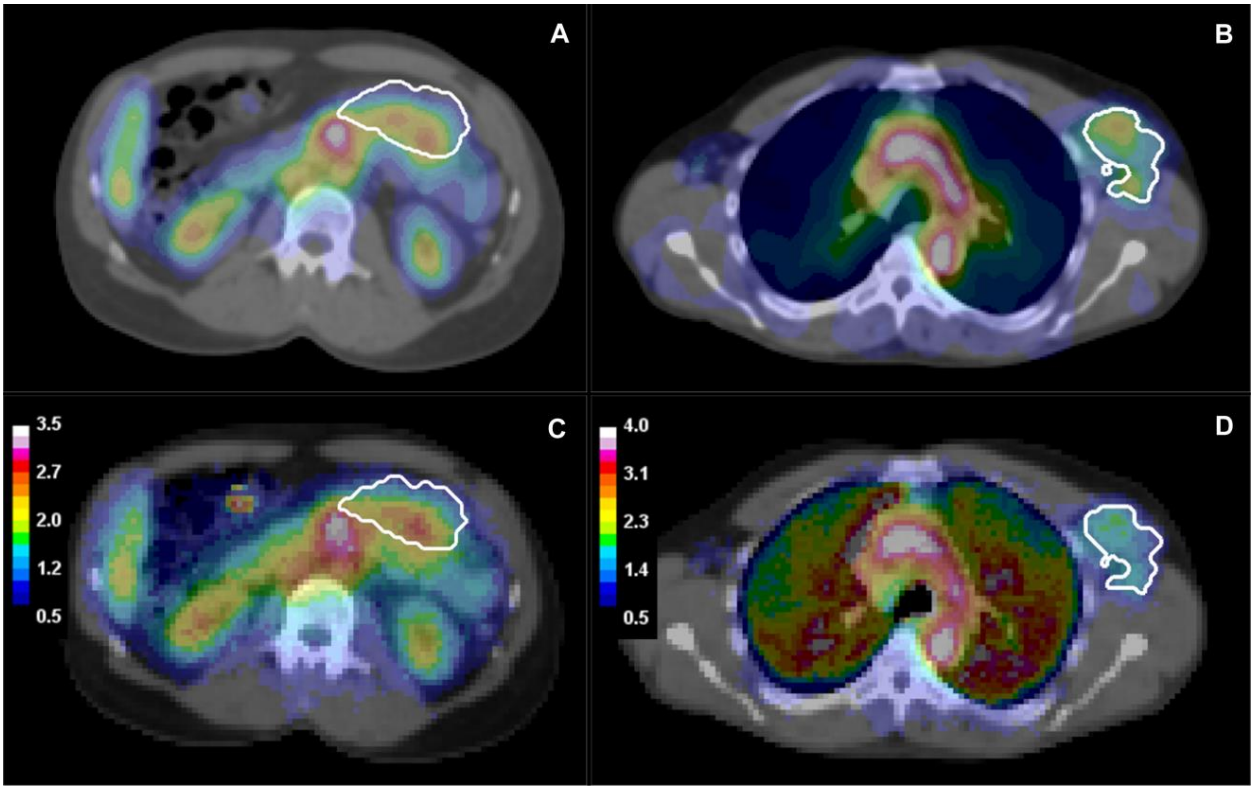

Figure V.1: Fused SPECT/CT images for (a) Patient 1 and (b) Patient 2 with matching 3D dose maps overlaid on CT for (c) Patient 1 and (d) Patient 2. Dose maps are displayed in Gy.

Table V.2: Comparison of mean absorbed tumor doses between VIDA and DPM.

	Patient 1: Abdominal Tumor		Patient 2: Lt. Axillary Tumor	
Initial tumor volume (ml)	269		226	
Total tumor shrinkage	53%		23%	
	VIDA	DPM	VIDA	DPM
Predicted dose, static vol. (cGy)	291	—	153	—
Predicted dose, changing vol. (cGy)	292	261 (12%)	154	164 (-6.1%)
Delivered dose, static vol. (cGy)	196	—	150	—
Delivered dose, changing vol. (cGy)	252	266 (-5.3%)	151	162 (-6.8%)

Relative difference defined as $100 \times (D_{VIDA} - D_{DPM}) / D_{DPM}$.

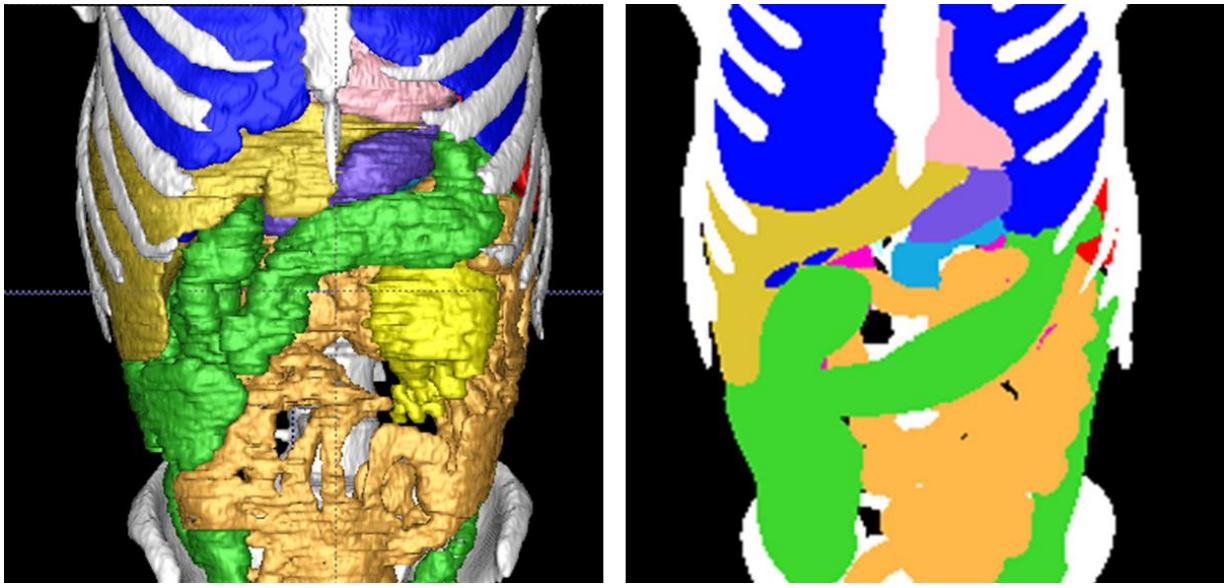

Figure V.2: Patient anatomy defined by (a) manual segmentation and (b) deformable NURBS.

Patient-specific anatomy was defined using two different methods, by manually-segmented organ volumes and a deformable NURBS model (see Figure V.2). Mean absorbed doses to tumor and organs were calculated for both types of patient models and compared to results from dose factors derived from the RADAR adult male reference phantom (Stabin et al. 2012) and the unity density sphere model (Stabin & Konijnenberg 2000). Organ doses are reported only if the entire volume was included in the field of view. With the exception of heart dose in patient 1, the organ doses from the patient-specific NURBS models agrees with manually segmented organs within 10%. In all cases, the mean absorbed doses to organs in NURBS model were larger. Compared to the reference phantom, patient organ doses differed by 3 to 19%.

Table V.3: Mean absorbed doses to organs and tumors from post-therapy dosimetry.

	Patient 1			Patient 2		
Organ	VIDA Dose (cGy) Segmented Model	VIDA Dose (cGy) NURBS Model	RADAR Dose (cGy)	VIDA Dose (cGy) Segmented Model	VIDA Dose (cGy) NURBS Model	RADAR Dose (cGy)
Lungs	—	—	—	221	224 [1%]	254 (-13%)
Heart	411	504 [23%]	438 (-6%)	311	322 [7%]	380 (-18%)
Spleen	186	207 [11%]	191 (-3%)	183	189 [3%]	160 (14%)
Liver	223	246 [10%]	210 (6%)	—	—	—
Kidneys	190	194 [2%]	160 (19%)	—	—	—
Tumor	196	—	187 (5%)	150	—	135 (11%)

Relative percent differences (in brackets) defined as $100 \times (D_{NURBS} - D_{Manual}) / D_{Manual}$
Relative percent differences (in parentheses) defined as $100 \times (D_{VIDA} - D_{RADAR}) / D_{RADAR}$

Additionally, tumor DVHs (see Figure V.3) were generated using volumes from the first post-tracer scan for both the predicted dose from the tracer study and the delivered dose from treatment. The first post-tracer time point, scaled by the ratio of activity administered for the therapy and tracer studies, was included in the therapy data set due to the lack of an early imaging time point.

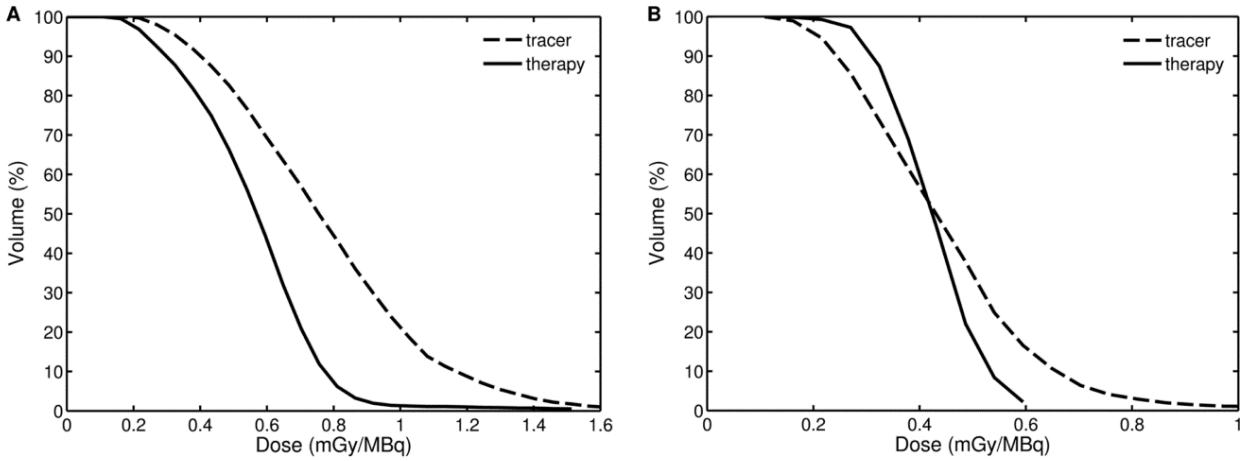

Figure V.3: Tumor DVHs from tracer and therapy scans for (a) Patient 1 and (b) Patient 2. The tumor volumes were taken from the first post-tracer scan.

Discussion

We have performed SPECT-based tumor and organ dosimetry for patients receiving ^{131}I RIT using VIDA and patient-specific anatomical models created from a deformable NURBS phantom using the Phantom Morphus software. This study investigated VIDA's treatment of non-uniform activity distributions and clinical utility of using deformable phantoms in TRT dose assessment. Tumor doses, accounting for volume changes over the scan times, were compared to DPM MC, offering an additional validation of VIDA for application to patient dosimetry.

Tumor volumes were manually segmented from the CT for each time point by a radiologist with expertise in body CT. When we account for changes in tumor volumes, the tracer-predicted tumor doses concur with the delivered therapeutic dose within 16%. For both patients, the tracer scans over-predict the delivered dose, although the difference for patient 2 is very small. This trend is consistent with a previously reported study (Dewaraja et al. 2009). The therapy-delivered mean absorbed doses were compared to results from DPM MC using the same tumor volumes. With the exception of the tracer study for Patient 1, the tumor doses from VIDA are lower by 5–7% compared to DPM. Our dose rates for the changing tumor volumes were derived from mean values from the 3D energy deposited maps for the tumor VOI defined at each time point. These volume-averaged dose rates were fit to a bi-exponential curve and directly integrated to determine the mean tumor dose. In comparison, the calculation of the mean tumor-absorbed dose using DPM involves a piecewise integration of the absorbed dose rates over three time periods using a mixed model fit (Schipper et al. 2012). These varying approaches may account for the discrepancies in tumor dose, even though the differences in instantaneous tumor absorbed-dose rates between the two simulations were less than 2%.

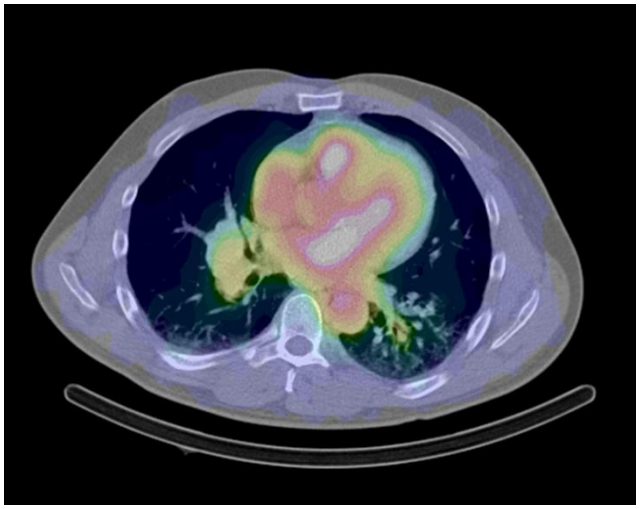

Figure V.4 Overlay of high heart activity uptake in patient 1 on CT image

Mean absorbed organ doses from the patient-specific NURBS models were compared to manually-segmented data with relative differences of 1% to 23%. That largest difference occurs in the heart dose for patient 1. This could be due to the high activity in blood (see Figure V.4) in conjunction with the smaller heart volume in the NURBS model (-8.3%) compared to the manually-defined heart VOI. The smaller NURBS surface may fail to encompass regions of the outer heart wall that received lower doses, skewing the mean absorbed dose higher. All other NURBS organs showed good agreement with doses from the manually-segmented patient model with organ doses higher in the NURBS models in all patients. The bias towards higher doses in the NURBS organs may be due to their larger organ volumes, with differences ranging from 1% to 15%. However, this trend was not observed in the validation study of patient-specific NURBS models and no correlation between volume differences and the over- or underestimation of organ dose is indicated (see Chapter 4). One possible explanation for the higher doses may be the way the NURBS surfaces are voxelized, leading to a systematic difference in absorbed dose. Another contributing factor to the differences in organ doses may be slight errors in the registration between the NURBS model and 3D absorbed dose map. As this study consisted of only two

patients, further investigation must be performed in order to fully quantify any effect organ doses calculated using patient-specific NURBS models in 3D image-based time-sequenced TRT dosimetry.

Patient mean absorbed organ doses from the manually-defined volumes and patient-specific NURBS model were compared to doses from a reference phantom with relative differences less than 20% (see Table V.3). The differences could be caused by several different factors. The reference dose calculations were performed based on activity in user-specified source organs. Activity in the rest of the field of view was assigned to the body remainder. The dose to target organs from the body remainder activity is calculated based on a uniform distribution of this activity spread across the entire volume in the phantom (including arms and legs). Thus, we would expect the reference organ doses to be lower compared to VIDA where dose is deposited in target organs from activity solely from the available field of view. Also, there are slight differences in the material densities and compositions in VIDA compared to those used to generate the SAFs for the RADAR reference phantom. The lung density is lower in VIDA by more than 10%, which may account for the underestimation of lung dose for Patient 2. Additionally, tumor doses were also compared to self-irradiation doses using the uniform sphere model in OLINDA/EXM. As expected, the tumor doses from VIDA are larger by 5-11% due to the contribution from the remaining body.

Tumor DVHs were generated based on the predicted and delivered dose maps (see Figure V.3). Tumor volumes were defined based on segmentation of CT from the first post tracer scan. It is difficult to assess the impact of tumor regression on 3D dose heterogeneities, and mass changes across the imaging time period were not incorporated in the DVHs. Both patients exhibit more conformal dose distributions for the delivered tumor dose compared to the tracer-predicted

distribution. The maximum delivered dose is also lower compared to the predicted DVH. One possible explanation for these differences is an increased antibody clearance in tumor cells after treatment due to radiobiological damage caused by the tracer dose, as previously suggested by Eary et al. (Eary).

Many contributing factors make estimating the uncertainty in organ and tumor doses for patient studies difficult. When performing voxel-based patient dosimetry using MC, there are multiple sources of error, including the quantification of the activity distribution, the fidelity of the registration process between the serial SPECT/CT scans, and the ability to properly define organ and tumor volumes. Also, fitting voxel dose rates with a limited number of time points may introduce additional uncertainty. Acquisition of more than 3 sequential SPECT scans post-tracer or post-therapy administration would reduce uncertainty in the 3D dose from the fitting process but may be prohibitive in the clinical environment.

The 3D OSEM reconstruction methods used for the patient studies in this work have produced quantitative results within 10% for volumes 16 ml and larger without partial volume correction (Dewaraja et al. 2005). Furthermore, the organ and tumor volumes in the patient studies presented here are sufficiently large, preventing partial volume effects from being a significant source of error in the average absorbed doses. MIRD Pamphlet 23 recommends PVC for objects less than dimensions of 3 × Full Width at Half Maximum (FWHM) of the spatial resolution of reconstructed images, but a well-validated method for voxel based corrections for SPECT has yet to be developed (Dewaraja et al. 2012). Therefore, voxel-level PVC was not applied prior to using the activity distributions in VIDA. In order to mitigate the uncertainty in reported doses due to partial volume effects, we limited the voxel resolution of the 3D dose map

to 3.908×3.908×5 mm^3, a factor of four larger than the original reconstructed image resolution and on the order of the intrinsic FWHM of the SPECT system used to acquire the data.

Image registration accuracy for 3D internal dosimetry has been discussed previously (He & Frey 2010, Papavasileiou et al. 2007, Sjögreen-Gleisner et al. 2009). Availability of high resolution co-registered SPECT/CT images in our patient studies permitted CT based registration. Thus, possible errors in SPECT-SPECT registration from poor spatial resolution and temporal variability in the activity distributions were avoided. A mutual information rigid registration algorithm was used in this study. Non-rigid techniques have been shown to provide the most robust results; however only small differences in doses for volumes of interest were found between rigid and non-rigid registration (Sjögreen-Gleisner et al. 2009). Nonetheless, rigid registration may affect the accuracy of the 3D dose to the axillary tumor in Patient 2, as non-rigid movements are more likely to occur in the neck and shoulder region of the body. An effort to quantify the effects of mis-registration on 3D patient dose was beyond the scope of the present study.

Organ segmentation may also contribute to the uncertainty in reported doses. Errors in structure are typically small compared to those from image registration; however erosion or dilation of the volume by only one voxel can contribute as much of 7% difference in activity (He & Frey 2010). Because volume of interest definition is typically a subjective task reliant on human observation, it is difficult to predict the true magnitude of the error. The tumor volumes were identical in VIDA and DPM to avoid segmentation uncertainties in our relative dose comparisons, but no assessment was done to determine the error in the defined volumes outlined by the radiologist compared to the true physical volumes. Additionally, tumor volumes were not created in the NURBS models, although there are tumor surfaces included in the reference

NURBS phantom. It is possible to outline the tumor and fit these structures to NURBS surface. The accuracy of this method and its impact on tumor dosimetry is an area of future investigation.

Summary

Evidence of correlation between patient outcomes and dosimetric quantities including tumor absorbed dose and equivalent biological effect (Dewaraja et al. 2014), and between organ dose and toxicity (Bodei et al. 2008, Stillebroer et al. 2012) exemplifies the benefit of performing patient-specific treatment planning in TRT. In this chapter, we have shown how VIDA can be used to predict 3D tumor and organ doses from time-sequenced SPECT/CT scans acquired after tracer administration of radioactivity. Despite requiring time-intensive Monte Carlo simulations, dosimetry results from VIDA can be obtained within 24-48 hours of obtaining the final image set of the study. Thus, VIDA is capable of performing treatment planning with a similar timeline as accepted clinical procedures for dose optimization and quality assurance in external bean radiation therapy.

In this clinical study, we also reported organ doses using patient-specific anatomy derived from a deformable NURBS model. Our results show that dosimetry using organ volumes from NURBS-based phantoms agree within 1–23% of doses obtained from manually-segmented volumes of interest. The reduction in time required to create a patient-specific NURBS model compared to conventional segmentation techniques (i.e. 2–3 hours versus 8–12 hours depending on field of view, organs at risk and inclusion of individual bone surfaces) resolves one of the major impediments to performing dosimetry in TRT clinically.

CHAPTER VI

DISCUSSION AND CONCLUSIONS

Summary of Results

Recent advancements in health care have ushered in the era of personalized medicine with the goal of tailoring medical treatment to the individual. Targeted radionuclide therapies offer the prospect of highly individualized cancer treatments. However, the necessary dose assessment required to optimize patient treatment is not routinely employed as a clinical tool. The objective of this work was to develop a clinical application to perform patient-specific dosimetry in targeted radionuclide therapy with the use of deformable anthropomorphic phantoms. The developed dosimetry method includes two separate applications, VIDA to perform 3D dose estimation using the Geant4 toolkit and the Phantom Morphus software to create patient-specific models from a NURBS-based reference phantom using CT images as a template for the transformation. The utility of these applications was evaluated with two studies. Manually segmented PET/CT images were compared to the patient-specific NURBS model to investigate the ability to construct an accurate representation of a patient using the Phantom Morphus software. Application of the dosimetry code to ^{131}I RIT patient studies demonstrated the clinical feasibility of this method (time, work-flow etc.) and comparison to another dosimetry code validated the accuracy of the dose results.

The first goal of this work was to develop VIDA, a 3D dosimetry application based on Monte Carlo simulations performed by the Geant4 toolkit. The application consists of three major components, the Geant4 simulation code performs particle transport and tallies energy

deposition in each voxel based on user-supplied organ and activity maps, the fitting tool fits exponential functions to the time-sequenced dose rate maps and integrates the fit to calculate voxel-based absorbed doses, and evaluation of the dosimetry results is performed by computing tumor and organ mean absorbed doses and dose-volume histograms.

Studies have indicated that dosimetric factors, including tumor absorbed dose and equivalent biologic effect, are predictive of patient outcomes (Dewaraja et al. 2014). Additionally, our application of VIDA to RIT patient studies indicates that tracer dosimetry is a good predictor of therapeutic tumor doses (see Chapter 5). Given the importance of accurate dose estimates to predictive outcomes, VIDA can be used for patient-specific treatment planning in a clinical setting. VIDA's workflow is designed to calculate voxel-level dose rate maps from a set nuclear medicine studies acquired at several time points after the administration of a tracer amount of radioactivity and integrate these over time. Although this approach requires multiple MC simulations, it does not impose additional time to perform the dosimetry as each simulation commences soon after the completion of each scan, exploiting the time interval between image acquisitions. The time-limiting step is the dose-rate simulation of the last scan and the voxel-by-voxel integration of dose rates. Simulation of dose-rate maps with relative uncertainties of less than 10% in each voxel by VIDA require approximately 20 hours to complete without parallel computing; these times are on the order with other 3D dosimetry codes (Furhang et al. 1997, Marcatili et al. 2013). Therefore, patient-specific dose estimates can be completed within 48 hours of the last tracer scan. This time frame is comparable to the treatment planning timetable for external beam therapy, as the completion of intensity-modulated radiation therapy planning and quality assurance requires at least two days after acquisition of the patient CT. We conclude that VIDA is a viable method for prospective image-based treatment planning for patients

receiving TRT. The ability to predict tumor and organ doses and optimize delivered dose lends to improved treatment outcomes and minimizes toxicity and harmful side-effects.

The second and third objectives of this work were the development of a software application to create NURBS-based patient-specific anatomical models using patient CT as a template and the evaluation of these models compared to manually-segmented volumes, the current gold standard in TRT. The Phantom Morphus software developed as a part of this dissertation provides an interactive platform for a user to deform a reference NURBS model based on patient anatomy from CT imaging. This approach significantly reduces the time required to define volumes of interest for dose assessment. Additionally, the use of the NURBS XCAT phantom offers a new method of modeling bone marrow in the skeleton as each bone surface contains a marrow cavity that can be populated with red marrow voxels. Bone marrow is often the dose-limiting organ when radiolabeled antibodies are employed (i.e. RIT) and the ability to measure dose to red marrow regions of the skeleton when MC simulation is employed may provide an alternative method for estimating dose compared to analysis of activity in blood. The ability to accurately model patient anatomy using deformable models was assessed using PET/CT studies of four patients. Evaluation metrics including total volume difference, percent volume overlap and average surface distance error were used to compare the NURBS models to careful slice-by-slice manual segmentations. Overall, the NURBS organs were in good agreement with manually-segmented volumes and the differences observed were similar to results by controlled observer studies of other automatic and semi-automatic segmentation methods (Campadelli et al. 2009, Rao et al. 2005, Segars et al. 2009).

NURBS-based patient-specific anatomical models may have applications other than tissue and organ definition in dose assessment. One notable example is tracking tumor motion during

treatment with external beam therapy. The XCAT phantom includes 4D models of respiratory and cardiac cycles (Segars et al. 2010) that can be used to track the position of the lung lesions during treatment. The XCAT phantom contains thousands of anatomical structures. Given this complexity, the use of patient-specific NURBS models may expand into other medical applications beside cancer radiation therapy as personalized medicine grows.

The final goal of this work was to apply VIDA and Phantom Morphus to perform 3D dosimetry in patients receiving ^{131}I RIT for NHL. This study demonstrated the clinical viability of these applications and also provided additional validation of the dose results by comparing tumor doses obtained using VIDA to another established MC dosimetry method (DPM). The tumor doses from VIDA were in agreement with those from DPM within 12%. Likewise, differences in organ doses between manually-segmented volumes and NURBS-based models were small, with differences being typically 10% or lower. We conclude that the dosimetry methods described in this work provide a novel and accurate approach to dose assessment in TRT and form a practicable solution to performing clinic patient-specific dosimetry prior to therapeutic treatment, which is currently not widely available. This will permit optimized treatment for each patient, hopefully leading to better outcomes and longer survival.

Future Work

Currently, the methods for performing patient-specific dosimetry described in this work are contained in individual applications. The Phantom Morphus software is a stand-alone application used to create patient-specific NURBS models. The resulting model is then converted to a voxel format by a command line voxelization program and must be registered to the activity data. Prior to running VIDA Monte Carlo, additional processing steps are necessary to create an activity map with the desired number of decay events and to ensure the model is registered to the activity

data. These steps are completed in MATLAB. Once 3D energy deposited maps are generated from the MC simulations, these time-sequenced maps are converted o dose-rate maps and co-registered using custom MATLAB scripts. The voxel-by-voxel exponential fitting is performed using VIDA's fitting tool, and the resulting 3D integrated dose map is used to generate tumor and organ DVHs and mean absorbed dose values. The future direction of this project will focus on integrating these processes, with the exception of the MC simulation typically performed on a computing cluster, into a single comprehensive software package.

Future work will also emphasize optimization of MC simulations to increase computational efficiency. Beginning with the release of Geant4 version 10.0 (December 2013), multi-threaded processing is possible to allow for efficient execution of simulations using parallel computing architectures (Cosmo, G. (). Multi-threading occurs at the event level, and the generation of events in parallel leads to a linear speed up of processing time with the number of threads used. Running VIDA on a computing cluster using the multi-threading capabilities of Geant4 10.0 would result in decreased simulation time, greatly reducing the overall time required to perform patient-specific treatment planning in TRT in a clinical setting. Furthermore, it is possible to decrease simulation run times by altering the way Geant4 navigates voxel boundaries. We plan on investigating modification of the voxel search algorithm for parametrized volumes to increase simulation efficiency (Jiang & Paganetti 2004). Others groups, who have performed voxelized dose calculations with this customized geometry navigation library, have seen run time improvement of two orders of magnitude (Sutherland et al. 2007). If the impact on VIDA's simulation time is similar, the particle transport can be performed in a matter of minutes compared to around 20–30 hours.

The method for creating patient-specific NURBS models can be advanced and improved. We aim to optimize the point cloud surface fitting algorithm using surface distance minimization instead of the current point distance method. The addition of different reference phantoms sizes as a starting point for creating patient-specific models may shorten the overall time required to deform the reference organs to match the patient. As mentioned earlier, more and more XCAT phantoms are being produced which may form a library of reference phantoms. Other NURBS phantom libraries may also be used. The inclusion of an atlas of NURBS organs representing a variety of morphologies and anatomical orientations that can be interchanged with reference anatomies may also facilitate the process and further reduce the fitting time.

The scope of this work was limited to the assessment of absorbed dose, namely the amount of energy deposited per unit of mass. Because TRT involves the use of open source radioactivity, the temporal change in dose rate as the radionuclide decay may play a significant role in the biological response to treatment. Studies have shown that incorporation of radiobiological modeling in dosimetric analysis may better elucidate tumor-dose response and correlate with therapy endpoints (Dewaraja et al. 2014, Dewaraja et al. 2010). Thus, including radiobiological modeling in VIDA is a logical extension of this work.

The study of molecular-based targets is growing and many new radiopharmaceuticals for use in TRT have been developed. As the ability to treat disease with targeted radiolabel agents grows, so does the necessity for fast and accurate dose assessment. With the ability to quickly create anatomical models and perform MC simulation of decay of any radionuclide, the methods described in this work provide a foundation for a clinical dosimetry application that can be widely distributed with a broad use in many types of targeted radionuclide treatments.

APPENDIX A

PHYSICAL PRINCIPLES OF INTERNAL DOSIMETRY

Several fundamental physical principles shape the field of nuclear medicine and the methodology behind internal dosimetry. Outlined in this appendix, these principles include the modes of radioactive decay and how particles emitted through these mechanisms interact with matter. Absorbed dose, the primary measure of the biological effects caused by ionizing radiation is formally defined and radiobiological considerations in internal dosimetry are briefly described. More in-depth discussions of the physics of nuclear medicine and radiobiology are found in textbooks on these subjects (Bushberg et al. 2011, Cherry et al. 2012, Hall & Giaccia 2006, Stabin 2007, Stabin 2008a).

Radioactive Decay Mechanisms

Nuclear medicine involves the use of substances in the form of a drug, chemical, or compound labeled with a radioactive isotope to diagnosis or treat disease. Radioactive decay is the transition of an unstable atomic nucleus to a lower energy level, producing ionizing radiation in the process. Three types of radioactive decay, alpha, beta, and gamma emission, provide the physical mechanism for detecting malignant tissue and depositing dose in radionuclide therapy.

Alpha (α) decay occurs in heavy nuclei with the ejection of an alpha particle consisting of two protons and two neutrons (a helium nucleus, ${}_2^4He$). Radium decay into the inert gas radon is an example of α-decay (see equation A.1). Although not traditionally used in targeted therapy, alpha-particle emitters provide high potency and specificity and have been a focus of investigation for cancer therapies. The first and only alpha-emitting radiopharmaceutical for use

in humans, ^{223}Ra dichloride (Xofigo, Bayer Healthcare) for treatment of metastatic castration-resistant prostate cancer, received FDA approval in 2013 (Parker et al. 2013).

$$^{226}_{88}Ra \rightarrow {}^{222}_{86}Rn + {}^{4}_{2}He \quad \text{A.1}$$

Atomic nuclei with a ratio of neutrons to protons that is either too high or too low for stability undergo radioactive decay with the emission of a beta (β) particle. Two types of beta decay occur. In the case when the nucleus has an excess neutron, the neutron transforms into a proton and an electron (β^- particle) is ejected from the nucleus. The generalized formula for β^- decay is given by equation A.2.

$$^{1}_{0}n \rightarrow {}^{1}_{1}p + e^- + \bar{\nu} \quad \text{A.2}$$

Positron (β^+) decay results in a nuclear transition for a nucleus with an excess proton. The proton transforms into a neutron and a positron and neutrino are ejected from the nucleus (see equation A.3). The emission of the neutrino or antineutrino conserves lepton number in the transition.

$$^{1}_{1}p \rightarrow {}^{1}_{0}n + e^+ + \nu \quad \text{A.3}$$

Beta decay is characterized by the maximum energy of the emitted particle. However, many particles are ejected with energies less than the maximum with the remaining energy carried away by the neutrino or antineutrino. This results in a spectrum of beta energies with a mean value of approximately one-third of the maximum.

Beta decay plays a vital role in internal dosimetry. Targeted therapy relies on β^- emission to deliver dose to diseased tissue through electron interactions with matter. PET provides 3D functional imaging by coincidence detection of annihilation photons created as secondary products of β^+ decay. The positron emitted through β^+ decay will quickly interact with an electron creating an annihilation event and the detection of these photons pinpoints the uptake of the radiopharmaceutical.

A competing process to β^+ decay is electron capture (see equation A.4), in which the number of neutrons in the nuclide increases by capturing an orbital electron. Electron capture does not directly produce ionizing particles but characteristic x-rays or one or more Auger electrons are released to fill the vacancy of the inner shell electron.

$$ {}_{1}^{1}p + e^{-} \rightarrow {}_{0}^{1}n + \nu \qquad \text{A.4} $$

Radioactive decay events often leave the progeny nucleus in an excited energy state. The nucleus returns to the ground state via isometric decay producing one or more gamma rays with characteristic energies based on transition probabilities. SPECT detects these gamma emissions and provides a method to quantify the activity distribution within the patient.

In some cases, an isomeric transition occurs by internal conversion where an electron interacts with the nucleus and the energy contained in the excited nuclear state transfers to the electron. The electron is ejected from the atom with kinetic energy equal to the energy released by the nucleus reduced by the binding energy of the electron. In addition to the ejected electron, characteristic x-rays or one or more Auger electrons are created when the vacancy of the inner shell electron is filled.

Radioactive decay is a stochastic event and the momentary prediction of which radioactive atoms will decay is not achievable. However, given a large sample of radioactive atoms, the average rate of decay is an exponential process where the amount of nuclear transformations is proportional to the number of unstable atoms present. The mathematical expression for the number of radioactive atoms as a function of time is derived from the relationship in equation A.5.

$$ -\frac{dN}{dt} = \lambda N \qquad \text{A.5} $$

The minus sign represents that the rate of decaying atoms decreases with time and λ is a proportionality constant is known as the decay constant. The left-hand side of equation A.5, the number of radioactive atoms undergoing nuclear transformations per unit time, is called the activity (A).

The solution to the differential equation A.5 defines the number of atoms remaining after time t given an initial quantity of N_0 atoms, given by:

$$N(t) = N_0 e^{-\lambda t} \quad \text{A.6}$$

Equation A.6 can be expressed in terms of activity by multiplying both sides by the decay constant. Activity behaves exponentially and decreases by a constant fraction in a given time interval.

$$A(t) = A_0 e^{-\lambda t} \quad \text{A.7}$$

The half-life ($T_{1/2}$) of a radionuclide is defined as the time required for half of the unstable atoms to undergo nuclear transformation, resulting in a residual of 50% of the initial activity. Half-life is inversely proportional to the decay constant with the following relation:

$$T_{1/2} = \frac{\ln 2}{\lambda} \quad \text{A.8}$$

Half-life and the decay constant are characteristic of each radionuclide and can vary from less than a picosecond to more than billions of years.

Particle Interactions in Matter

Particles created during radioactive decay interact with the environment in different manners depending on their mass and electric charge. Electrons and positrons interact with other charge particles, such as electrons and nuclei in the medium, primarily through the electromagnetic force and may produce secondary charged particles capable of their own interactions. Neutral particles, such as photons, randomly interact with matter depending on the probability cross-

sections that are specific to a material. The energy loss from particle absorption, attenuation, and scattering is the source of the biological effect of ionizing radiation. Figures in this section were adapted from Bushberg et al. (Bushberg).

Charged Particle Interactions

Charged particles, including electrons and alpha particles of decay events, continuously interact through the Coulomb force with atoms present in matter and lose kinetic energy through excitation, ionization, and radiative losses. Electromagnetic interactions occur between a free electron and atomic nuclei as well as other electrons in the medium. Heavy charged particles, such as an alpha particle, primarily lose energy though coulombic interactions between their positive charge and the negative electrons of the absorber atoms.

Inelastic collision with atomic electrons is the principal process of charged particle energy transfer, resulting in the excitation or ionization of orbital electrons in the interaction medium. Excitation occurs when some of the energy of the incident particle is transferred to an electron in the absorbing material causing promotion to a higher orbital level (see Figure A.1a). The excited orbital electron will return to a lower energy level and emit characteristic x-rays or Auger electrons (see Figure A.1b). If the energy transferred exceeds the binding energy of the orbital electron, the electron is ionized and ejected from the atom. When the impulse of the charge particle is large enough, the ionized electron may have sufficient kinetic energy to undergo its own interactions as shown in Figure A.2. These electrons are called delta rays and represent an indirect method for transferring the charged particle energy to the absorbing medium.

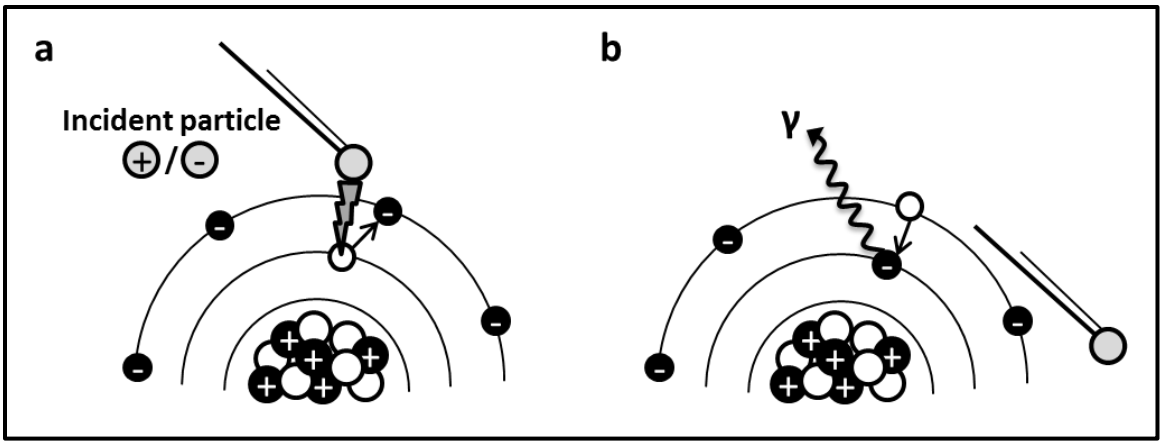

Figure A.1: (a) Excitation of orbital electron due to inelastic collision with a charged particle. (b) Characteristic x-ray emission from relaxation of excited electron.

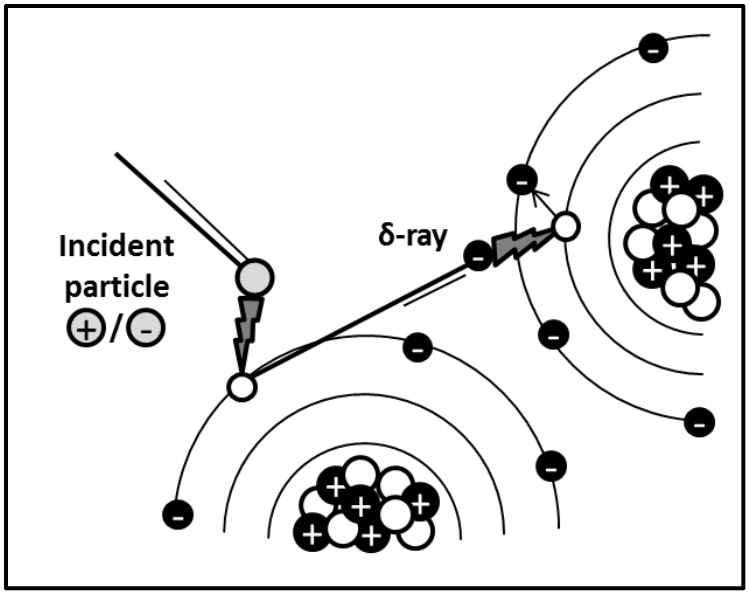

Figure A.2: Ionization of orbital electron and subsequent excitation by the δ-ray electron.

Charged particles are scattered through interactions with atomic electrons in the form of elastic collisions. In an elastic scattering event, the total kinetic energy of the colliding particles is unchanged. This process is only significant for low-energy electrons and results in small energy transfers.

Electrons also interact with the nucleus in the form of elastic or inelastic collisions. The elastic collision of an electron with a nucleus, known as Rutherford scattering, does not produce

radiation nor excite the nucleus. The charged particle only loses energy through the recoil of the nucleus. The inelastic collision of an electron with a nucleus results in a loss of kinetic energy through the deflection of the electron path by the positively charged nucleus. The energy lost is carried away by electromagnetic radiation called bremsstrahlung (see Figure A.3). If the electron has sufficient kinetic energy, the inelastic collision may excite the nucleus to a higher energy level and result in gamma emission through isomeric transition.

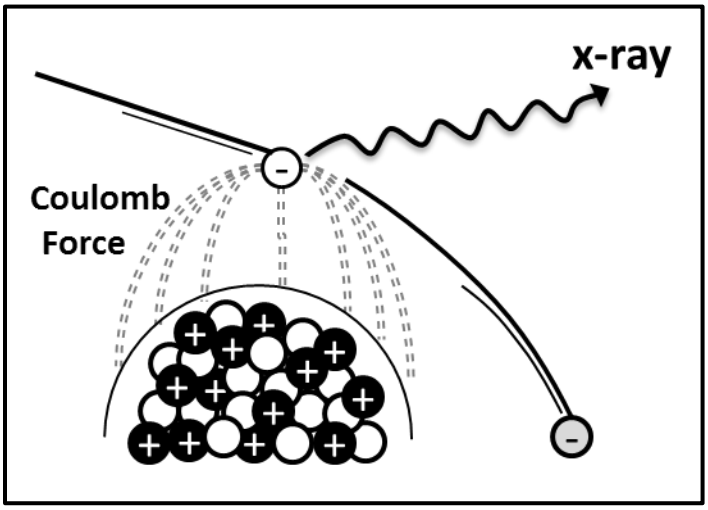

Figure A.3: Bremsstrahlung emission due to coulombic interaction between a free electron and the nucleus of an atom.

Positrons, positively charged anti-electrons produced in β^+ decay, lose kinetic energy in the same way as electrons by excitation, ionization, and radiative interactions. Once at rest, a positron interacts with a negatively charged electron and the pair is annihilated. The rest masses of the positron and electron are converted to electromagnetic radiation in the form of two annihilation photons, each with energy of 0.511 MeV.

The distance a charged particle travels in matter is dependent on the rate of energy loss, which is a function of the type of charged particle and the density of the medium. The amount of energy deposited *locally* along the path length of a charged particle is defined as the linear energy transfer and is proportional to the square of the charge and inversely proportional to the

kinetic energy. The total energy loss rate is called the linear stopping power and includes radiative losses through bremsstrahlung photons, which may deposit energy at some distance from the particle track.

The range of a charged particle is defined as the distance the particle penetrates the interaction medium. Heavy charged particles (α particles) lose energy in a continuous process with only slight deflections caused by collisions with atoms and orbital electrons. Thus, the range of an α particle is essentially equal to its path length. Electrons may undergo sharp deflections as they travel through the interaction medium and follow a tortuous path that is longer than the range. Electron ranges are variable even for particles with the same kinetic energy due to interaction probabilities. Maximum and mean ranges are calculated by measuring the relative number of particles transmitted as a function of the absorbed thickness.

Photon Interactions

Photons are electromagnetic radiation with no mass and no charge and because they are electrically neutral, they do not interact via the Coulomb force progressively along their path length. Instead, the interaction between photons and matter is a stochastic process governed by interaction probabilities, resulting in scattering or absorption of the photon. The four major types of interactions between photons and matter are coherent (Rayleigh) scattering, the photoelectric effect, Compton scattering, and pair production. The most important photon interactions in internal dosimetry include photoelectric absorption and Compton scattering due to the creation of free electrons that in turn cause ionization effects. Photon interactions via pair production are limited to photon energies greater than twice the rest mass of an electron, which exceeds the energies typical for gamma emissions of common radionuclides.

Coherent scattering is an elastic collision between a photon and a bound electron in an atom, resulting in the deflection of the photon without the loss of energy (see Figure A.4). Coherent scattering occurs with low energy radiation that is less than the binding energy of the interacting orbital electron. Because the photon loses no energy, coherent scattering does not contribute to patient dose.

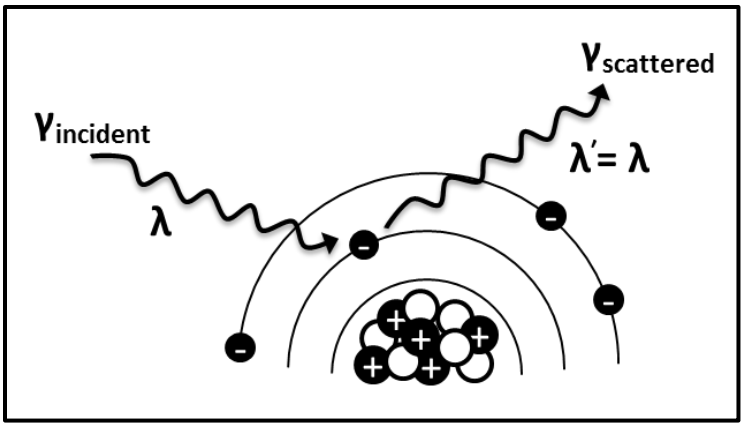

Figure A.4: Coherent scattering of photon from interaction with orbital electron.

The photoelectric effect is an interaction in which the photon is completely absorbed by an atom. The energy absorbed transfers to an orbital electron and causes the electron to be ejected from the atom with a kinetic energy equal to the difference between the incident photon and the binding energy (see Figure A.5). Photoelectric absorption occurs only when the energy of the photon exceeds the binding energy of the shell of the interacting electron. If sufficient energy exists, the innermost shell is the most probable electron orbital to participate in the photoelectric effect. In low-Z materials such as soft tissue, the binding energies are less than a few keV and rarely limit photoelectric interactions.

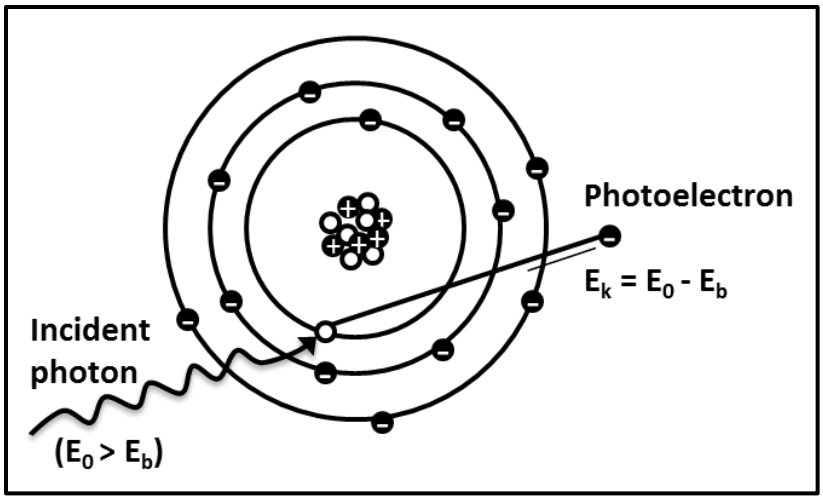

Figure A.5: The photoelectric effect.

The probability of a photoelectric event is approximately proportional to Z^3/E^3, where Z is the atomic number of the interaction medium and E is the incident photon energy. For low photon energies and high-Z materials, photoelectric absorption is the predominant mechanism for photon interaction.

Compton scattering results when an incident photon interacts with an outer shell electron imparting some of its energy to the electron and causing a re-emission of a photon at an angle with respect to the original path (see Figure A.6). The electron, initially assumed to be at rest, gains kinetic energy and is ejected from the atom. The energy of the scattered photon (E') depends on both the initial photon energy (E_0) and the scattering angles (θ) (see equation A.9). The amount of energy transferred to the electron ranges from zero to a maximum for a scattering angle of 180°.

$$E' = \frac{E_0}{1 + \frac{E_0}{m_e c^2}(1 - \cos\theta)} \qquad \text{A.9}$$

Unlike the photoelectric effect, Compton scattering is most likely to occur between photons and valence shell electrons. The probability is almost independent of the atomic number of the

scattering medium and instead is directly proportional to the electron density of the material and decreases with increasing photon energy. The maximum amount of energy transferred to the Compton electron is very small for low energy photons and is independent of the interaction probability. As the photon energy increases, the ratio between photon energy and electron rest mass increases and the maximum fractional energy transferred approaches unity for energies above 10 MeV.

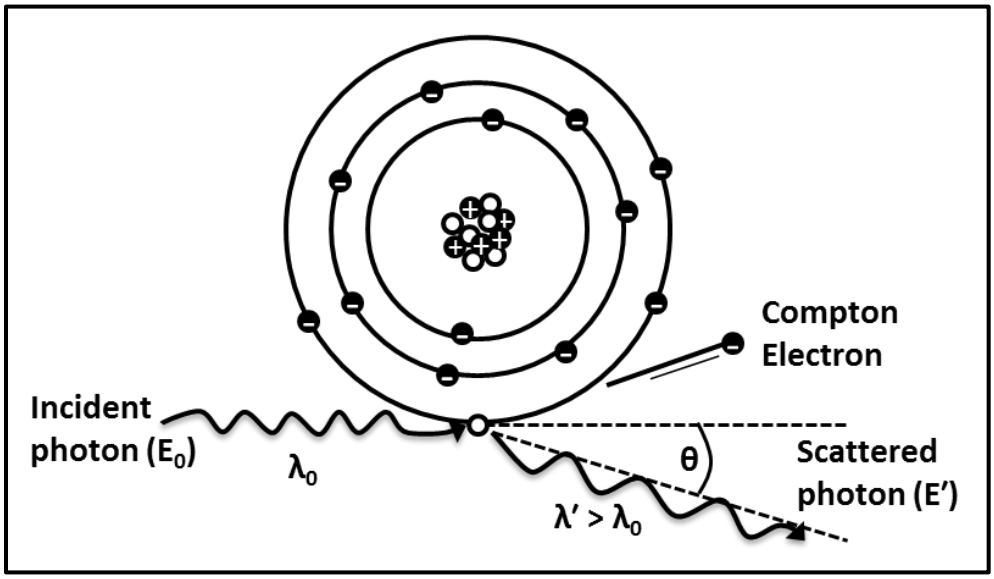

Figure A.6: Compton scattering of an incident photon.

Compton scattering is the predominant interaction for gamma ray energies typically produced by radionuclides used in nuclear medicine. The ejected electron will interact with the absorbing medium and lose energy via excitation and ionization of other atoms. The scattered photon may or may not interact again as it traverses the medium.

Absorbed Dose

The fundamental metric relating to biological response in radionuclide therapy is absorbed dose, the energy absorbed per unit mass of tissue. Absorbed dose is applicable to all types of ionizing radiation, both directly and indirectly ionizing sources and can be measured for sources

external to the absorbing medium or for radiation distributed within. The absorbed dose (D) is expressed in terms of the stochastic quantity energy imparted (ε) and is defined in equation A.10 as the expectation value of the energy imparted to matter per unit mass (m) at a point (Attix 1986). The unit of absorbed dose is called a gray (1 Gy = 1 J/kg).

$$D = \frac{d\varepsilon}{dm} \qquad \text{A.10}$$

The energy imparted is the difference between the radiant energy of charged and uncharged particles entering the volume and the radiant energy leaving the volume, accounting for net energy derived from rest mass within the volume (i.e. electron-positron annihilation). For indirectly ionizing radiation, as in the case of photons, the energy is imparted to the absorbing medium in two steps. First, kinetic energy is transferred from the ionizing radiation to secondary charged particles (i.e. electrons and positrons). These charged particles then lose kinetic energy to the medium resulting in absorbed dose. The secondary charged particles may also experience bremsstrahlung losses that do not contribute to locally imparted energy.

Radiobiological Considerations

Although simple and straightforward, absorbed dose calculations do not always predict the response of living tissue to ionizing radiation. Factors such as the type of radiation, the radiation energy and the rate of energy deposition can influence the biological effects. In nuclear medicine, the dose rate varies temporally with the physical and biological decay of the radioisotope. The dose rate rises from zero after administration of the activity to a peak value and then drops back to zero after many effective half-lives of the source. One method used to quantify the effect on response due to dose rate is the Biologically Effective Dose (BED). BED is an adjustment of the measured absorbed dose to reflect the expected biological effect as

delivered at a reference dose rate. The reference value is chosen to approach zero when the total dose is delivered in an infinite number of infinitesimally small fractions (Sgouros et al. 2008).

BED is based on the linear-quadratic (LQ) model of radiobiological effect that emphasizes two distinct types of DNA damage leading to cell death (see Figure A.7). The first type of damage occurs when adjacent DNA strands break from a single ionizing event and is proportional to the dose. The second type of damage results from two proximal single-strand breaks due to separate ionizing events and is proportional to the square of the dose. If only one single-strand break occurs, damage may be potentially repairable and is categorized as sub-lethal.

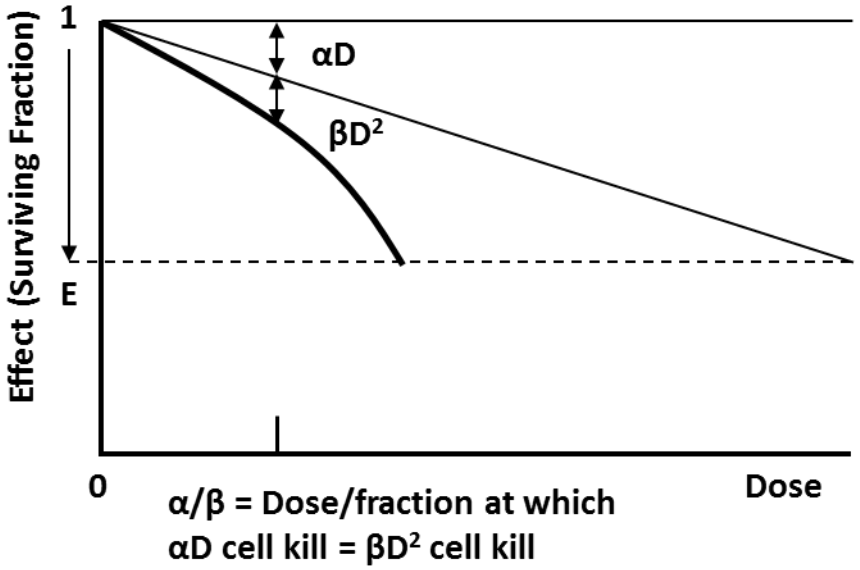

Figure A.7: The linear-quadratic model of the radiation effect on biological tissue with α the number of logs of cell kill per Gy and β the number of logs of cell kill per Gy^2.

BED is expressed as the product of the total physical dose and a relative effectiveness (RE) factor that accounts for radiobiological parameters and the dose delivery method (Dale & Carabe-Fernandez 2005). The RE factor depends on two principal radiobiological parameters: the tissue α/β ratio and the sub-lethal damage recovery constant (μ). The α/β ratio measures the

relative importance of the two processes that result in DNA double strand breaks in the LQ model (Dale 1985). For therapy with an exponentially decreasing dose rate, the BED is expressed in equation A.11 where $\dot{D}_0$ is the initial dose rate and λ is the rate constant describing exponential loss of activity.

$$BED = \frac{\dot{D}_0}{\lambda}\left(1 + \frac{\dot{D}_0}{(\mu + \lambda)(\alpha/\beta)}\right) \quad \text{A.11}$$

An alternative method has been proposed for tissue volumes with dose rates that are not well fitted with a single decreasing exponential but is rarely implemented clinically as dosimetry studies often lack sufficient time points to resolve uptake and clearance-related dose-rate differences (Sgouros et al. 2008).

The relevance of BED to target radionuclide therapy is twofold. One, BED is a useful way to compare the effectiveness of targeted therapy to other radiation therapy delivery methods including external beam and brachytherapy. Two, absorbed dose values may not be indicative of tumor and normal tissue response to certain lower molecular weight targeting agents. The biokinetics of these agents differ greatly and pre-clinical and clinical evidence (Wessels et al. 2008) suggest that the dose rate may be a significant factor in tumor response and normal organ toxicity.

Another radiobiological quantity, equivalent uniform dose (EUD), has potential use in assessing tumor response and comparing different tumor absorbed dose distributions across a patient population. Accounting for cell kill parameters α and β, EUD is defined as the uniform dose that would produce the same biological response as the original spatially-varying absorbed dose. EUD is derived by equating the surviving fraction from a uniform absorbed dose to the surviving fraction from the probability distribution of normalized BED values (Amro et al. 2010, Niemierko 1997, Sgouros et al. 2008).

APPENDIX B

FUNDAMENTALS OF NUCLEAR MEDICINE IMAGING

Dosimetry requires knowledge of the spatial distribution of radioactivity within the body. Due to the inability to directly measure activity *in vivo,* tomographic imaging techniques that detect emitted particles from radioactive decay have been developed to estimate the 3D distribution. Nuclear medicine imaging modalities are characterized by the types of particles detected. SPECT imaging relies on the detection of single photons, either x-rays or gamma rays, emitted during radioactive decay. PET is an indirect method of imaging radionuclides that decay via β^+ emission by the detection of pairs of photons produced during an annihilation event between the emitted positron and an electron in the body. The basic procedures for SPECT and PET imaging are described below; additional details may be found in textbooks on medical imaging (Bushberg et al. 2011, Cherry et al. 2012)

Single Photon Emission Computed Tomography (SPECT)

SPECT imaging of a radiolabeled pharmaceutical is performed by detecting single photons emitted through the radioactive decay process that travel through the body by a scintillation camera. The camera rotates around the patient and projection images are taken at different angles (see Figure B.1). The camera consists of a collimator, scintillation crystal, photomultiplier tubes, and positioning electronics. The collimator serves to focus the camera towards direct emissions and minimizes the detection of scattered photons. Photons that pass through the collimator interact with the scintillation crystal, typically sodium iodide (NaI). This interaction converts the photon energy to visible light that is then collected by an array of photomultiplier tubes (PMTs).

The photocathode in the PMT converts the visible light to electrons. The electronic signal is amplified as it travels through the PMT array and is processed by the computer electronics to determine the position and energy of the event. The number of events collected is proportional to the activity at each point.

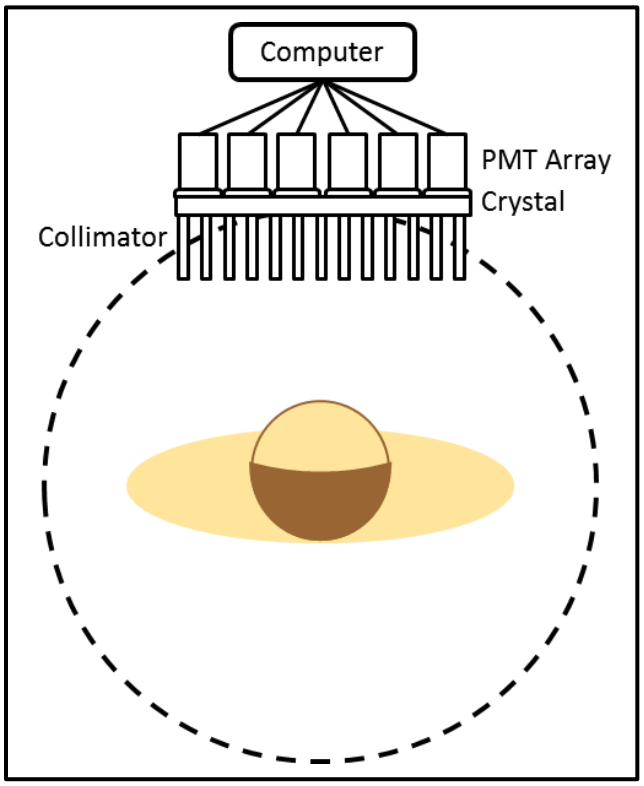

Figure B.1: SPECT camera and image acquisition.

One factor that limits the detection sensitivity of SPECT is photon attenuation. As photons travel through the body, they interact with tissue and may be scattered or absorbed. This non-uniform attenuation is dependent on both the distance the photon travels through the body and tissue densities along its path (see Figure B.2). The camera cannot distinguish between increased counts originating from a point of increased activity or reduced attenuation from photons traversing low density tissue (i.e. lungs). Without correction, artifacts of increased counts in areas of low attenuation (body periphery and low tissue density) and reduced counts in areas of high attenuation (body center and high tissue density) may occur. Correction for attenuation

effects requires knowledge of the attenuation coefficient distribution in the patient. Thus, the SPECT camera system is coupled to CT to provide co-registered attenuation maps for correction during image reconstruction.

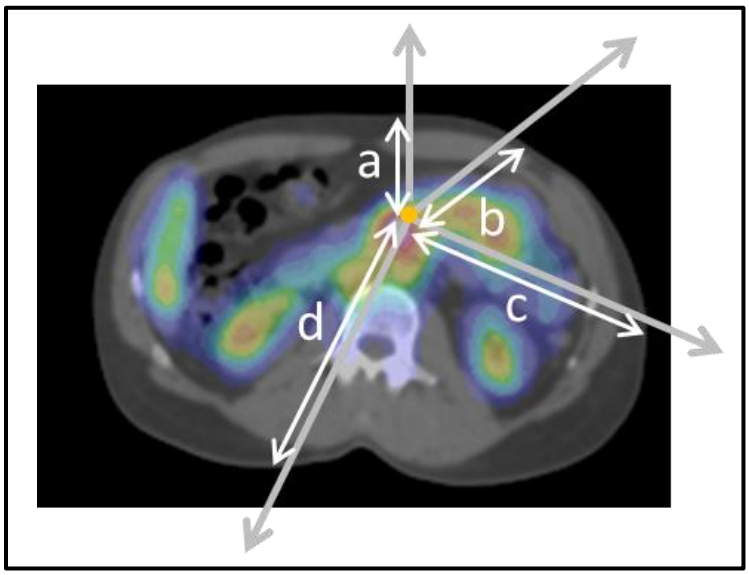

Figure B.2: Non-uniform attenuation in SPECT.

Gamma rays also interact with tissue through Compton scattering causing deflection from their original path and a loss in energy. These scattered photons may be detected within the photopeak window (see Figure B.3), resulting in reduced image contrast. One approach to reducing scatter is to improve the energy resolution of the scintillator as NaI has relatively poor energy resolution (e.g. 10% FWHM at 140 keV) and requires a large acquisition window to achieve good signal. Semiconductor detectors such as cadmium telluride and cadmium zinc telluride offer improved energy resolution between 2–5% for 140 keV gamma rays (Madsen 2007). Compensation for the reduction in image contrast from scatter may also be achieved using energy-distribution-based methods. One example of energy-distribution-based scatter correction is the TEW method. Scatter in the photopeak window is estimated by acquiring counts in narrow

energy windows on each side of the photopeak and determining the area under the trapezoid formed by the signal in each of these windows.

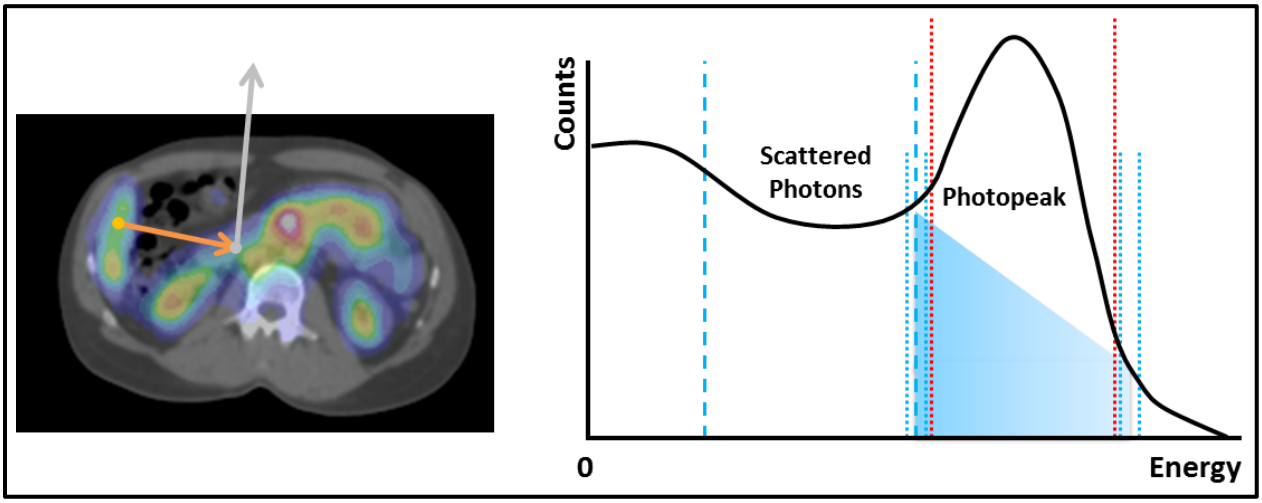

Figure B.3: Compton scattering in SPECT. Scattered photons may be detected in the energy window of the photopeak causing decreased image contrast. Correction is made using the triple-energy-window method, shown by the shaded trapezoid

Several other degrading factors besides attenuation affect the sensitivity, contrast and resolution of SPECT images. SPECT is photon limited with more than 99% of all photons emitted in the patient absorbed by the collimator. Noise from low counting statistics in the image contributes to loss of contrast. The detection efficiency can be increased by having wider spaces between the septa in the collimator, but this reduces the spatial resolution of the image. Thus, a tradeoff exists between spatial resolution and efficiency when considering the design of the collimator. One way of obtaining a higher counting efficiency without changing the collimation is for the SPECT system to have two rotating camera heads. The CDR also contributes to the sensitivity and spatial resolution of SPECT. CDR consists of three main components: the geometric response, septal penetration, and collimator scatter. Geometric response refers to the finite solid angle subtended by the collimator holes. This angle increases with increased distance from the detector and resolution is non-uniform with depth (see Figure B.4). While the geometric

response can be represented in analytical form, the septal penetration and collimator scatter response must be modeled using more advanced techniques such as MC simulation or function fitting of point-source measurements (Chun et al. 2013).

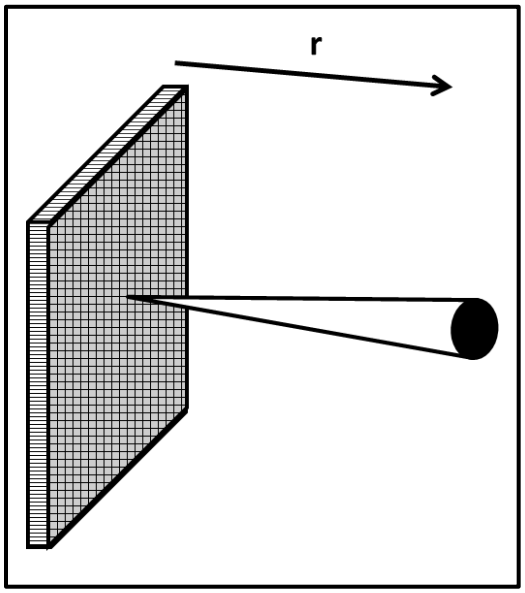

Figure B.4: Geometric contribution to CDR. The spatial resolution of the camera decreases with increasing depth of the imaging plane.

The images collected by the SPECT camera are 2D projections taken at different angles. These projection images are input into algorithms to reconstruct the 3D distribution of activity. Reconstruction algorithms are either analytical or iterative. Analytical reconstruction, such as filtered back projection (FBP), uses mathematical solutions to solve the inverse problem of determining the 3D activity distribution that forms the projection data. In essence, each projection is smeared back along the path of collection and areas of high activity will add constructively in the superposition of all projection angles. Analytical reconstruction is simple to implement but does not account for image degrading effects including depth-dependent spatial resolution, attenuation and scatter. In order to compensate for attenuation and noise, iterative approaches to SPECT reconstruction were developed. Iterative reconstruction algorithms start with an initial guess of the activity distribution and forward project this distribution through a

model of the SPECT camera. The resulting 2D projections are compared to the actual data and the difference between them is used to update the original source distribution. This process is repeated until convergence is reached. Common iterative algorithms include maximum-likelihood expectation maximization (MLEM) and OSEM. The MLEM algorithm compares all projection data when updating the distribution. The OSEM algorithm is a modification to MLEM with data grouped into subsets for comparison between calculated and real projections. Thus, the OSEM is computationally more efficient and results in more rapid and accurate data convergence. The benefit to iterative algorithms is the ability to incorporate models of attenuation, scatter, and CDR specific to the SPECT system. The main limitation to interactive techniques is an increased processing time, especially when a large number of iterations is required. However, improved computer speeds enabled iterative methods to become the standard for clinical SPECT reconstruction.

Positron Emission Tomography (PET)

PET imaging is based on the detection of annihilation photons created from the interaction of a positron and electron. Thus, PET tracers contain radioisotopes that undergo β^+ decay. Conservation of momentum requires that the photons are emitted in opposite directions and are subsequently detected by a ring of detector elements, shown in Figure B.5. The elements are linked electronically and isolate events that occur nearly simultaneously. These coincidence events create a line of response (LOR) and form projections that are then reconstructed into tomographic images. Because the beta particles only travel a short distance before annihilating with an electron, the reconstructed images represent the spatial distribution of radioactivity in the body, just as with SPECT images formed by single photon events.

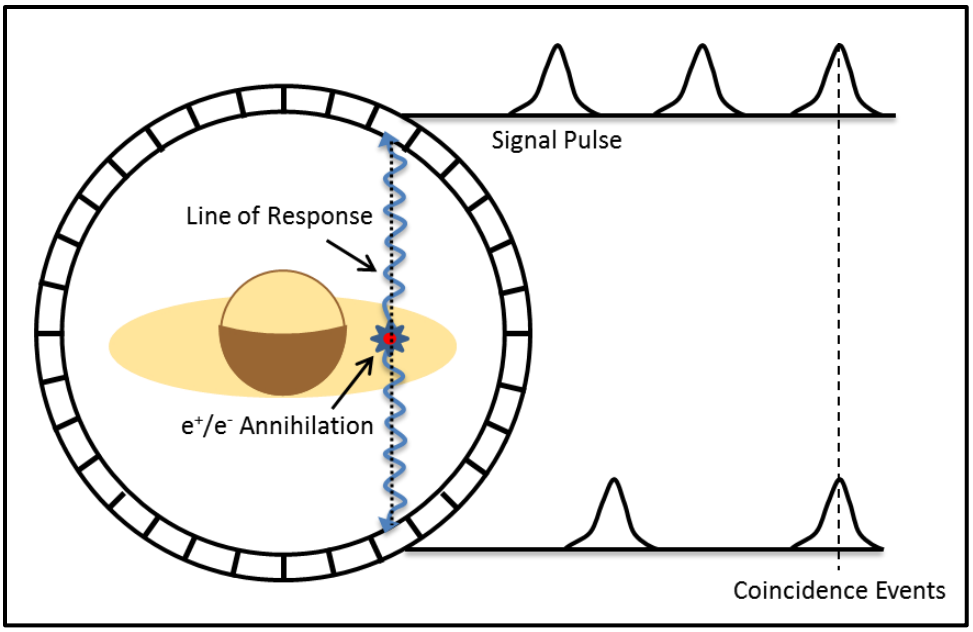

Figure B.5: PET imaging acquisition and electronic collimation by coincidence event detection.

Similar to SPECT systems, the PET detector ring consists of scintillation crystals linked to PMTs. However, due to the poor detection efficiency of NaI at the energy of annihilation photons (511 keV), scintillation crystals used in PET typically have a higher density and effective atomic number, such as bismuth germanium oxide (BGO), gadolinium oxyorthosilicate (GSO), or lutetium oxyorthosilicate (LSO). One difference in the PET detector is the lack of a physical collimator. Instead, the positional information of an event is defined by the LOR joining the two crystal elements that detected the coincidence events, known as electronic collimation. Unlike physical collimation, electronic collimation is able to make use of signals from photons detected from a range of incident angles and not only those with angles normal to the collimator face. This leads to better sensitivity and increased spatial resolution in PET compared to SPECT.

PET systems typically employ multiple detector rings aligned in the axial direction. These camera systems can operate in two different modes. In 2D PET, thin layers of septa are placed between the detector rings to reduce interplane scatter. Coincidence events are limited to detectors within the same ring or close neighbors. In 3D PET, the septa are removed and LORs

are formed between all detector pairs, increasing the overall sensitivity of the camera. Increased detector sensitivity reduces patient dose and produces higher quality images with less noise.

The three types of coincidence events that can be detected, true, scattered, and random are illustrated in Figure B.6. In a true event, the photon pair leaves the annihilation site and travel through the body without interaction where they are both detected within the timing interval for a coincidence event. If one or both of the photons undergoes Compton scattering in the body before being detected, a scattered coincidence event forms an incorrect LOR. A random event occurs by an incorrect pairing of photons from different annihilations that are detected within the coincidence time window. The photon pairs of these detected photons are either absorbed in the body or pass through the scintillator without interacting. Both scattered and random events contribute to noise in the image with scattered events accounting for up to 40% of the total.

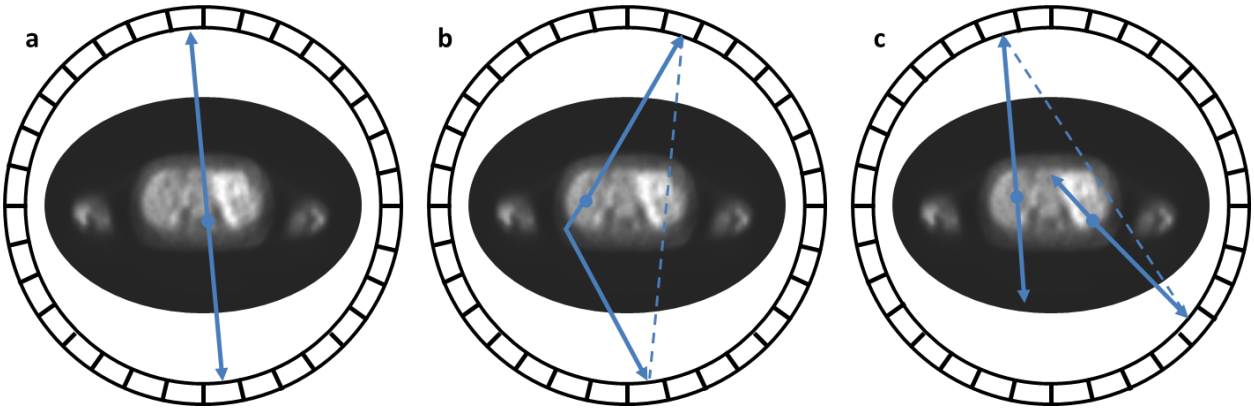

Figure B.6: Types of detection events in PET: (a) true, (b) scattered, and (c) random. The dotted lines indicate the assigned and incorrect LOR for scattered and random events

The resolution of PET is limited by several physical factors. The spatial resolution is defined, in part, by the positron range in tissue. Once emitted, the positron will travel a short distance, experiencing multiple interactions that reduce its kinetic energy until it slows down and annihilates with an electron. The energy and subsequent range of the emitted positron depends on the PET radioisotope; for ^{18}F, the range in tissue before annihilation is approximately 1 mm

(Levin & Hoffman 1999). Additionally there is a loss in spatial resolution due to non-collinearity of the photons that occurs if the positron is not exactly at rest at the time of annihilation. For ^{18}F, the distribution of angular deviation from 180° was measured experimentally in a patient with FHWM of 0.54 degrees (Shibuya et al. 2007). The loss in spatial resolution due to non-collinearity depends on the diameter of the detector ring and is approximately 1.5 mm (FHWM) for an 80-cm system (Levin & Hoffman 1999).

In order to achieve quantitative results, several corrections must be applied to PET images including normalization and compensation for random coincidence, scatter, and attenuation. PET image reconstruction is performed with the assumption that all LORs have the same sensitivity. However, due to differences in scintillation crystals and PMT response, each detector element has a different efficiency. Correction is performed by individual normalization for each. Random coincidences must be subtracted from the total number of events. Correction for random events is based on the rate of single events in each detector channel (r) and the camera resolving time (t). The rate of random coincidences for a given LOR between the i^{th} and j^{th} detector elements is:

$$R_{ij} = 2tr_i r_j \qquad \text{B.1}$$

Another technique for random event correction is delayed event subtraction. Here, a channel is created to measure signal from one detector that is delayed by an interval greater than the resolving time for true coincidence. The events detected by the delayed channel are not true coincidences and represent an estimate of the number of random coincidences in the prompt signal. Scatter correction is particularly important in 3D PET where gains in sensitivity are coupled to an increase in scattered events. Correction of scattered events is typically performed using modeled-based algorithms. These algorithms require knowledge of the attenuation in the

patient obtained from CT and a model of the scanner geometry and detector to calculate the percentage of Compton scattered photons incident on each detector.

The necessity of attenuation correction is greater for PET compared to SPECT because image data is dependent of the detection of not one but two photons. Attenuation increases image noise, artifacts, and distortion and correction is required for both qualitative and quantitative use of PET images. This is exacerbated in overweight or obese patients with larger body widths. However, unlike with SPECT, attenuation in PET can be determined by an attenuation map generated through CT. The probability of detecting each photon is given by:

$$P(x') = exp\left(-\int_0^{x'} \mu(x)dx\right) \quad \text{B.2}$$

where $\mu(x)$ is the position-dependent linear attenuation coefficient and x' is the total path length traveled through the photon. Therefore the total probability of detecting both photons is

$$P_{tot} = P_1 P_2 = exp\left(-\int_0^{a} \mu(x)dx\right) \quad \text{B.3}$$

where a is the total length of the LOR. The attenuation correction factor is then 1 - P_{tot}.

Image reconstruction for PET is similar to SPECT imaging. Analytical reconstruction, including FBP, can be applied to both 2D and 3D acquisition modes. In 2D PET, the in-plane LORs are arranged to form a set of 1D parallel projections (see Figure B.7); in 3D mode, the LORs may be arranged into 2D sets of parallel projections. Although corrections for scatter, random coincidences, and the effects of attenuation can be applied to the projection data prior to reconstruction, FBP often results in images with amplified noise and streak artifacts. Iterative methods alleviate many of the problems of FBP and permit the use of advanced image projection models that incorporate detector sensitivity, scatter and random correction models, and artifact

and noise reduction techniques directly into the PET reconstruction algorithm. Thus, iterative reconstruction improves image quality and yields quantitative results required for dosimetry.

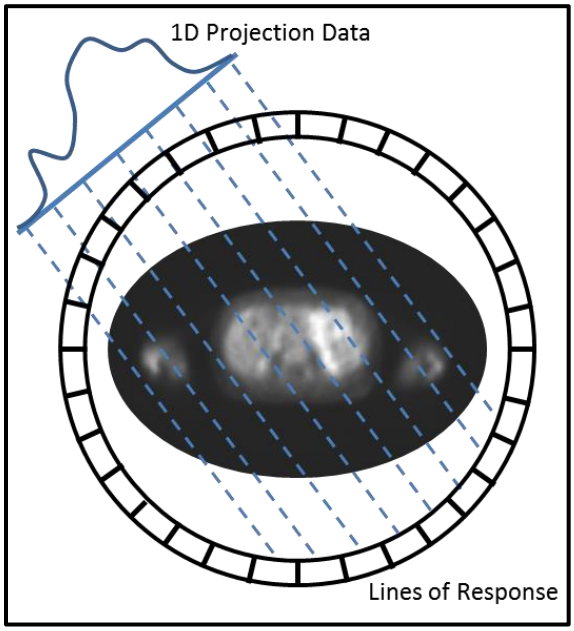

Figure B.7: PET projection data formed from events collected in a single detector ring.

Advancements in PET imaging include the capability of measuring photon time-of-flight (TOF). These systems exploit high light-output scintillators, high-performance PMTs and fast-timing electronics, to achieve an intrinsic system timing resolution of approximately 600 picoseconds (Karp et al. 2008). TOF PET systems use the time difference between detection of each coincident photon to localize the annihilation event along the LOR. The reduction in positional uncertainty results in detector sensitivity gain of up to a factor of four. Therefore, the use of TOF information can either decrease the scan time or enhance image contrast in PET. TOF PET is particularly useful for imaging large patients, in which increased attenuation and scatter results in poor image quality. In order to obtain the same noise-equivalent image for an obese patient compared to an average-sized patient, the acquisition time increases dramatically and is often unreasonable for clinical imaging. The increased sensitivity of TOF PET leads to improved image quality for heavy patients without increasing the scan time.

APPENDIX C

OVERVIEW OF MONTE CARLO METHODS

Monte Carlo methods describe statistical sampling techniques that approximate solutions to quantitative problems when closed form solutions are not attainable. The method was first developed at Los Alamos National Laboratory in 1946 by Stanislaw Ulam and John Von Neumann to estimate distances neutrons travel through various materials for radiation shielding calculations (Eckhardt 1987). Monte Carlo relies on repeated random sampling to obtain numeric results of an unknown probability distribution. Advancements in computer processing and architecture in the past 50 years have allowed Monte Carlo modeling and simulation of complex systems in many different disciplines.

Monte Carlo assumes that the system of interest is stochastic in nature, with events and input data described in probabilistic terms. The methodology follows three general steps (Harrison 2010, Raychaudhuri 2008). First, models of the probability density functions (PDFs) defining the range of simulation possibilities and their relative probability for each step in the system must be created. The PDF is not restricted to an analytical form and may be formulated from experimental data, theory or by a combination of data fitting to theory. Once the statistical distribution of each input parameter is defined, a set of random numbers is generated to sample these distributions to obtain a set of output parameters. This process is repeated, resulting in a collection of possible outcomes. The final step tallies the outcomes and statistical analysis is performed to provide a statistical confidence of the results as a function of the number of trials.

Monte Carlo methods depend on generating a large quantity of random numbers. Truly random numbers, such as the time of a radioactive decay event, cannot be created algorithmically. Instead, computers generate pseudo-random numbers uniformly over a given range of values using a deterministic pattern with an initial "random" seed. These numbers are typically sufficient for Monte Carlo, as the goal is to randomly sample large sets of data so that the samples are approximately evenly distributed. One benefit of pseudo-random numbers is that the sequence can be reproduced for testing or debugging if the same initial seed is used.

There are various ways to sample continuous or discrete distributions. The inverse transform method is the most direct method and can be applied to distributions with invertible PDFs. First the integral of the PDF is calculated, denoted as the cumulative distribution function (CDF) that is continuous and strictly increasing in [0,1):

$$F(x) = \int_0^1 p(x) \qquad \text{C.1}$$

Two steps are required to sample a random value x from the PDF. First, generate a random number u on the interval [0,1) and locate this position on the y-axis of the CDF. The random sample x is given by the inverse of the CDF:

$$x = F^{-1}(u) \qquad \text{C.2}$$

The inverse transformation method can also be used when the distribution is discrete. A discrete distribution is expressed in terms of the probability mass function (PMF), $p(x_i)$, and the cumulative PMF is given by:

$$F(x) = P(X \leq x) = \sum_{x_i \leq x} p(x_i) \qquad \text{C.3}$$

Again, the initial step involves sampling a random number u. The randomly sampled x_i from p is determined by the smallest positive integer i such that $u \leq F(x)$.

The inverse method is used in Geant4 to sample the distance a particle travels before interacting with the medium via a specific physical process (e.g Compton Scattering) (Agostinelli et al. 2003). The distance to interaction for a given process is determined by the mean free path (λ) of the particle. The probability of traveling a distance x without interaction is:

$$P(x) = e^{-n_\lambda} \tag{C.4}$$

where n_λ represents the total number of mean free paths traversed, which is independent of the interaction material.

$$n_\lambda = \int_{x_1}^{x_2} \frac{dx}{\lambda(x)} \tag{C.5}$$

The distance to the point of interaction, $s(x)$, given by the product of n_λ and $\lambda(x)$, can be sampled with a random number (η) uniformly distributed in the range (0,1):

$$n_\lambda = -\log(\eta) \tag{C.6}$$

This sampling is performed for all possible particle interactions. The process which returns the smallest distance is selected and its post step action is executed. If this is an interaction or decay, the particle is "killed" and secondary particles are generated and tracked. If not, the particle gets another chance to interact. The number of mean free paths for each unselected process is decremented by an amount corresponding to the length of the current step and the whole algorithm is repeated. An illustration of reducing the photon interaction lengths during Monte Carlo simulation is given in Figure C.1.

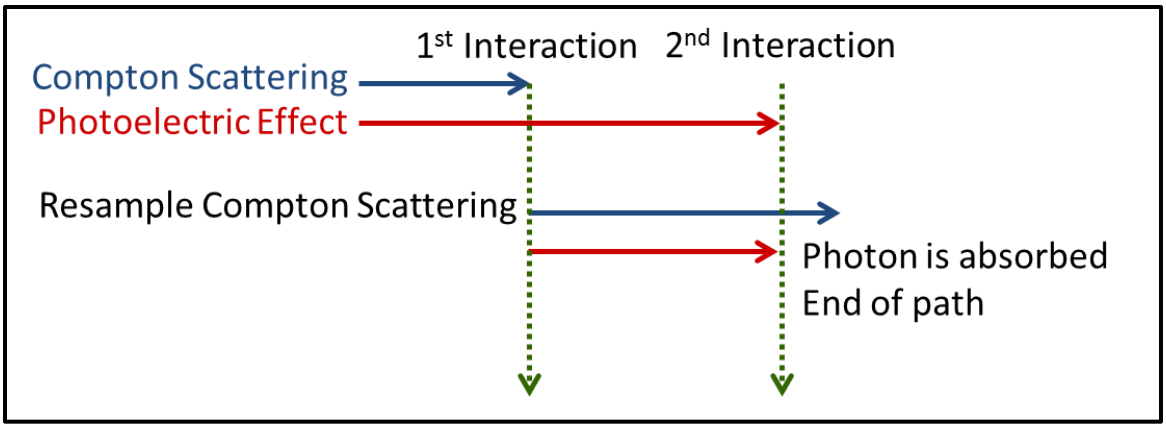

Figure C.1: Process of reducing photon interaction lengths during Monte Carlo simulation of particle interactions in matter.

In the case when the CDF is not invertible or when the inverse method is computationally slow, other sampling techniques may be employed. One such method is the accept-reject algorithm, first introduced by von Neumann (Neumann 1951). The acceptance-rejection approach is based on the observation that random variable selection is equivalent to uniformly sampling the area under the density function. The PDF of an arbitrary distribution $f(x)$ is sampled by choosing another distribution $g(x)$ that can be directly sampled, with the only restriction being $f(x) < M*g(x)$ for a constant M greater than 1. First, sample x from $g(x)$ and an additional random number, u, in the range (0,1). Then, check if $u < f(x)/M*g(x)$. If true, accept x and if not, reject the sampling and repeat. This method requires generating 2 random numbers and may lead to a lot of unwanted samples depending on the form of the distribution function. The number of rejections is exacerbated at higher dimensions and other more sophisticated sampling methods such as adaptive rejection sampling or the Metropolis-Hastings algorithm may be more efficient (Hastings 1970, Rubinstein & Kroese 2011).

The results of a Monte Carlo simulation represent an average of contributions from each history over the course of the entire sampling. Therefore, Monte Carlo methods are subject to

statistical analysis in order to establish the confidence in the results. One way to assess the statistical precision of the simulation tally is to estimate the relative error (R):

$$R = \sqrt{\frac{1}{N}\left(\frac{\overline{x^2}}{\bar{x}^2} - 1\right)} \qquad \text{C.7}$$

where N is the number of histories, the mean, $\bar{x}$, is the average value of the scores x_i, and $\overline{x^2}$ is the average value of the square of the scores, ${x_i}^2$. Equation IV.9 demonstrates that the relative error depends on the inverse square root of the number of histories, and in order to reduce the uncertainty by a factor of two, one must increase the number of samples by fourfold. It is important to note that this statistical analysis only evaluates the precision of the results and not the accuracy of how close the simulation estimates the true physical value. More details on estimating Monte Carlo precision and factors affecting the simulation accuracy can be found in Volume 1 of the MCNP manual (Sweezy et al. 2003).

APPENDIX D

MATERIAL TYPES AND INDENTIFIERS FOR ORGANS IN VIDA

Table C.1 lists the identification number and material used for each organ in VIDA. The density and composition of each material is defined in Table III.1. The skeleton may be defined as either whole bone or separated into cortical bone, red and yellow marrow as designated by the user in the simulation input file (Appendix E).

Table C.1: List of organs and assigned material type in VIDA Monte Carlo simulation.

Organ/Region	ID	Material
Body (remainder)	1	Soft tissue
Brain	2	Soft tissue
Cerebellum	3	Soft tissue
Brain stem	4	Soft tissue
Salivary glands	5	Soft tissue
Esophagus	6	Soft tissue
Right thyroid	7	Soft tissue
Left thyroid	8	Soft tissue
Thymus	9	Soft tissue
Right eye	10	Soft tissue
Right eye lens	11	Soft tissue
Left eye	12	Soft tissue
Left eye lens	13	Soft tissue
Right lung	14	Lung tissue
Left lung	15	Lung tissue
Liver	16	Soft tissue
Gall bladder	17	Soft tissue
Right kidney	18	Soft tissue
Left kidney	19	Soft tissue
Right adrenal	20	Soft tissue
Left adrenal	21	Soft tissue

Stomach	22	Soft tissue
Spleen	23	Soft tissue
Heart	24	Soft tissue
Pancreas	25	Soft tissue
Bladder	26	Soft tissue
Bladder contents	27	Water
Ascending large intestine	28	Soft tissue
Transcending large intestine	29	Soft tissue
Descending large intestine	30	Soft tissue
Sigmoid	31	Soft tissue
Rectum	32	Soft tissue
Small intestine	33	Soft tissue
GI contents	34	Soft tissue
Prostate (male only)	35	Soft tissue
Right testicle (male only)	36	Soft tissue
Left testicle (male only)	37	Soft tissue
Uterus (female only)	38	Soft tissue
Right ovary (female only)	39	Soft tissue
Left ovary (female only)	40	Soft tissue
Right breast	41	50% mammary / 50% adipose tissue
Left breast	42	50% mammary / 50% adipose tissue
Air	44	Air
Skeleton (omitting skull/mandible)	46-74	Whole bone or cortical bone
Skull	75	Whole skull or cortical bone
Mandible	76	Whole skull or cortical bone
Yellow marrow	77	Yellow marrow
Red marrow	78-108	Red marrow
Adipose	109	Adipose tissue
Tumors	111-120	Soft tissue

APPENDIX E

SAMPLE INPUT FILE FOR VIDA MONTE CARLO SIMULATION

The following is an example input file (data.dat) used for input to VIDA MC. The file indicates the location and names of the organ and activity maps and their dimensions. The user defines the source organs for primary events. This may be an individual organ (see Appendix D) or an identifier to run the whole body (999) or all organs (555). The user also specifies the atomic and mass numbers of the radionuclide and the type of material for the skeleton. The bone and marrow IDs can be defined as a single whole bone material (WB) or as distinct cortical bone, red and yellow marrow (RM).

```
-----------------------------------------------------------------
Sample data.dat file. The order of inputs is important.
-----------------------------------------------------------------

./organ_map.txt       : 3D organ map file name
./activity_map.txt    : 3D activity map file name
213                   : number of columns
142                   : number of rows
78                    : number of slices
1.9531 1.9531 5.0     : voxel dimensions, in mm (col, row, slice)
999                   : source organ (999 = body, 555 = organs)
53                    : radionuclide atomic number
131                   : radionuclide mass number
WB                    : marrow type (WB = mixture, RM = marrow)
exit                  : indicates end of input file
```

REFERENCES

Agostinelli, S., Allison, J., Amako, K., Apostolakis, J., Araujo, H., Arce, P., Asai, M., Axen, D., Banerjee, S., Barrand, G. et al. (2003), GEANT4–a simulation toolkit, *Nucl Instrum Meth A*, 506(3), 250–303.

Ahmadzadehfar, H., Muckle, M., Sabet, A., Wilhelm, K., Kuhl, C., Biermann, K., Haslerud, T., Biersack, H. & Ezziddin, S. (2012), The significance of bremsstrahlung SPECT/CT after yttrium-90 radioembolization treatment in the prediction of extrahepatic side effects, *Eur J Nucl Med Mol Imaging*, 39(2), 309–315.

Allison, J., Amako, K., Apostolakis, J., Araujo, H., Dubois, P. A., Asai, M., Barrand, G., Capra, R., Chauvie, S., Chytracek, R. et al. (2006), Geant4 developments and applications, *IEEE T Nucl Sci*, 53(1), 270–278.

Amato, E., Lizio, D. & Baldari, S. (2009), Absorbed fractions for photons in ellipsoidal volumes, *Phys Med Biol*, 54(20), N479–N487.

Amato, E., Lizio, D. & Baldari, S. (2011), Absorbed fractions for electrons in ellipsoidal volumes, *Phys Med Biol*, 56(2), 357–365.

Amro, H., Wilderman, S. J., Dewaraja, Y. K. & Roberson, P. L. (2010), Methodology to incorporate biologically effective dose and equivalent uniform dose in patient-specific 3-dimensional dosimetry for non-Hodgkin lymphoma patients targeted with ^{131}I-tositumomab therapy, *J Nucl Med*, 51(4), 654–659.

Armato III, S. G., McLennan, G., McNitt-Gray, M. F., Meyer, C. R., Yankelevitz, D., Aberle, D. R., Henschke, C. I., Hoffman, E. A., Kazerooni, E. A., MacMahon, H. et al. (2004), Lung image database consortium: developing a resource for the medical imaging research community, *Radiology*, 232(3), 739–748.

Attix, F. (1986), *Introduction to Radiological Physics and Radiation Dosimetry*, Wiley, John & Sons, Weinheim, Germany.

Aubert-Broche, B., Evans, A. C. & Collins, L. (2006), A new improved version of the realistic digital brain phantom, *Neuroimage*, 32(1), 138–145.

Baechler, S., Hobbs, R. F., Boubaker, A., Buchegger, F., He, B., Frey, E. C. & Sgouros, G. (2012), Three-dimensional radiobiological dosimetry of kidneys for treatment planning in peptide receptor radionuclide therapy, *Med Phys*, 39(10), 6118–6128.

Barone, R., Borson-Chazot, F., Valkema, R., Walrand, S., Chauvin, F., Gogou, L., Kvols, L. K., Krenning, E. P., Jamar, F. & Pauwels, S. (2005), Patient-specific dosimetry in predicting renal toxicity with ^{90}Y-DOTATOC: relevance of kidney volume and dose rate in finding a dose-effect relationship, *J Nucl Med*, 46(1 suppl), 99S–106S.

Bauman, G., Charette, M., Reid, R., Sathya, J. et al. (2005), Radiopharmaceuticals for the palliation of painful bone metastases–a systematic review, *Radiother Oncol*, 75(3), 258.E1–258.E13.

Beauregard, J.-M., Hofman, M. S., Pereira, J. M., Eu, P. & Hicks, R. J. (2011), Quantitative ^{177}Lu SPECT (QSPECT) imaging using a commercially available SPECT/CT system, *Cancer Imaging*, 11(1), 56–66.

Bodei, L., Cremonesi, M., Ferrari, M., Pacifici, M., Grana, C., Bartolomei, M., Baio, S., Sansovini, M. & Paganelli, G. (2008), Long-term evaluation of renal toxicity after peptide receptor radionuclide therapy with ^{90}Y-DOTATOC and ^{177}Lu-DOTATATE: the role of associated risk factors, *Eur J Nucl Med Mol Imaging*, 35(10), 1847–1856.

Boellaard, R. (2009), Standards for PET image acquisition and quantitative data analysis, *J Nucl Med*, 50(Suppl 1), 11S–20S.

Bolch, W., Bouchet, L., Robertson, J., Wessels, B., Siegel, J., Howell, R., Erdi, A., Aydogan, B., Costes, S. & Watson, E. (1999), MIRD pamphlet no. 17: the dosimetry of nonuniform activity distributions radionuclide S values at the voxel level, *J Nucl Med*, 40(1), 11S–36S.

Brans, B., Bodei, L., Giammarile, F., Linden, O., Luster, M., Oyen, W. & Tennvall, J. (2007), Clinical radionuclide therapy dosimetry: the quest for the "Holy Gray", *Eur J Nucl Med Mol Imaging*, 34(5), 772–786.

Breitz, H. B., Wendt, R. E., Stabin, M. S., Shen, S., Erwin, W. D., Rajendran, J. G., Eary, J. F., Durack, L., Delpassand, E., Martin, W. et al. (2006), ^{166}Ho-DOTMP radiation-absorbed dose estimation for skeletal targeted radiotherapy, *J Nucl Med*, 47(3), 534–542.

Brownell, G., Ellen, W. & Reddy, A. (1968), MIRD Pamphlet No 3 – absorbed fractions for photon dosimetry, *J Nucl Med*, 9, 27–39.

Brujic, D., Ainsworth, I. & Ristic, M. (2011), Fast and accurate NURBS fitting for reverse engineering, *Int J Adv Manuf Technol*, 54(5-8), 691–700.

Brujic, D., Ristic, M. & Ainsworth, I. (2002), Measurement-based modification of NURBS surfaces, *Comput Aided Des*, 34(3), 173–183.

Bruland, Ø. S., Nilsson, S., Fisher, D. R. & Larsen, R. H. (2006), High-linear energy transfer irradiation targeted to skeletal metastases by the α-emitter ^{223}Ra: adjuvant or alternative to conventional modalities?, *Clin Cancer Res*, 12(20), 6250s–6257s.

Burrill, J., Hafeli, U. & Liu, D. M. (2011), Advances in radioembolization-embolics and isotopes, *J Nucl Med Radiat Ther*, 2(1).

Bushberg, J., Seibert, J., Leidholdt Jr, E. & Boone, J. (2011), *The Essential Physics of Medical Imaging*, Lippincott Williams & Wilkins, Philadelphia, PA.

Campadelli, P., Casiraghi, E. & Esposito, A. (2009), Liver segmentation from computed tomography scans: a survey and a new algorithm, *Artif Intell Med*, 45, 185–196.

Chao, T. & Xu, X. (2001), Specific absorbed fractions from the image-based VIP-man body model and EGS4-VLSI Monte Carlo code: internal electron emitters, *Phys Med Biol*, 46(4), 901.

Chatal, J.-F. & Hoefnagel, C. A. (1999), Radionuclide therapy, *Lancet*, 354(9182), 931–935.

Cheng, K.-S., Wang, W., Qin, H., Wong, K.-Y., Yang, H. & Liu, Y. (2004), Fitting subdivision surfaces to unorganized point data using SDM, *in* '12th Pacific Conf. Computer Graphics and Applications (PG '04)', pp. 16–24.

Cherry, S. R., Sorenson, J. A. & Phelps, M. E. (2012), *Physics in Nuclear Medicine*, Elsevier Health Sciences, Philadelphia, PA.

Chiavassa, S., Bardiès, M., Guiraud-Vitaux, F., Bruel, D., Jourdain, J.-R., Franck, D. & Aubineau-Lanièce, I. (2005), OEDIPE: a personalized dosimetric tool associating voxel-based models with MCNPX, *Cancer Biother Radiopharm*, 20(3), 325–332.

Chun, S. Y., Fessler, J. & Dewaraja, Y. (2013), Correction for collimator-detector response in SPECT using point spread function template, *IEEE Trans Med Imag*, 32(2), 295–305.

Cicone, F., D'Arienzo, M., Carpaneto, A., Russo, E., Coniglio, A., Bischof Delaloye, A. & Scopinaro, F. (2013), Quantification of dose nonuniformities by voxel-based dosimetry in patients receiving ^{90}Y-ibritumomab-tiuxetan, *Cancer Biother Radiopharm*, 28(2), 98–107.

Clark, L. D., Stabin, M. G., Fernald, M. J. & Brill, A. B. (2010), Changes in radiation dose with variations in human anatomy: moderately and severely obese adults, *J Nucl Med*, 51(6), 929–932.

Collins, D., Zijdenbos, A., Kollokian, V., Sled, J., Kabani, N., Holmes, C. & Evans, A. (1998), Design and construction of a realistic digital brain phantom, *IEEE Trans Med Imag*, 17(3), 463–468.

Cosmo, G. (On behalf of the Geant4 Collaboration) (2014), Geant4 – towards major release 10, *J Phys Conf Ser*, 513(2), 022005.

Cristy, M. (1980), Mathematical phantoms representing children of various ages for use in estimates of internal dose, Technical Report ORNL/NUREG/TM-367, Oak Ridge National Laboratory.

Cristy, M. & Eckerman, K. F. (1987), Specific absorbed fractions of energy at various ages from internal photon sources, Technical Report ORNL/TM-8381 V, Oak Ridge National Laboratory.

Dale, R. & Carabe-Fernandez, A. (2005), The radiobiology of conventional radiotherapy and its application to radionuclide therapy, *Cancer Biother Radiopharm*, 20(1), 47–51.

Dale, R. G. (1985), The application of the linear-quadratic dose-effect equation to fractionated and protracted radiotherapy, *Br J Radiol*, 58(690), 515–528.

Danielsson, P.-E. (1980), Euclidean distance mapping, *Comput Vision Graph*, 14(3), 227–248.

D'Arienzo, M., Cicone, F., Chiacchiararelli, L., Coniglio, A., Delaloye, A. B. & Scopinaro, F. (2012), Three-dimensional patient-specific dosimetry in radioimmunotherapy with ^{90}Y-Ibritumomab-Tiuxetan, *Cancer Biother Radiopharm*, 27(2), 124–133.

DeNardo, G., DeNardo, S., Goldstein, D., Kroger, L., Lamborn, K., Levy, N., McGahan, J., Salako, Q., Shen, S. & Lewis, J. (1998), Maximum tolerated dose, toxicity, and efficacy of 131-I-Lym-1 antibody for fractionated radioimmunotherapy of non-Hodgkin's lymphoma, *J Clin Oncol*, 16(10), 3246–3256.

Dewaraja, Y. K., Frey, E. C., Sgouros, G., Brill, A. B., Roberson, P., Zanzonico, P. B. & Ljungberg, M. (2012), MIRD pamphlet no. 23: quantitative SPECT for patient-specific 3-dimensional dosimetry in internal radionuclide therapy, *J Nucl Med*, 53(8), 1310–1325.

Dewaraja, Y. K., Koral, K. F. & Fessler, J. A. (2010*a*), Regularized reconstruction in quantitative SPECT using CT side information from hybrid imaging, *Phys Med Biol*, 55(9), 2523.

Dewaraja, Y. K., Schipper, M. J., Shen, J., Smith, L. B., Murgic, J., Savas, H., Youssef, E., Regan, D., Wilderman, S. J., Roberson, P. L. et al. (2014), Tumor-absorbed dose predicts progression-free survival following ^{131}I-Tositumomab radioimmunotherapy, *J Nucl Med*, 55, 1047–1053.

Dewaraja, Y. K., Wilderman, S. J., Koral, K. F., Kaminski, M. S. & Avram, A. M. (2009), Use of integrated SPECT/CT imaging for tumor dosimetry in I-131 radioimmunotherapy: a pilot patient study, *Cancer Biother Radiopharm*, 24(4), 417–426.

Dewaraja, Y. K., Wilderman, S. J., Ljungberg, M., Koral, K. F., Zasadny, K. & Kaminiski, M. S. (2005), Accurate dosimetry in ^{131}I radionuclide therapy using patient-specific, 3-dimensional methods for SPECT reconstruction and absorbed dose calculation, *J Nucl Med*, 46(5), 840–849.

Dewaraja, Y., Schipper, M., Roberson, P., Wilderman, S., Amro, H., Regan, D., Koral, K., Kaminski, M. & Avram, A. (2010), ^{131}I-Tositumomab radioimmunotherapy: initial tumor dose-response results using 3-dimensional dosimetry including radiobiologic modeling, *J Nucl Med*, 51(7), 1155–1162.

Eary, J., Pollard, K., Durack, L., Bice, A., Lewellen, T., Matthews, D., Press, O., Nelp, W., Appelbaum, F. & Bernstein, I. (1994), Post therapy imaging in high dose I-131 radioimmunotherapy patients, *Med Phys*, 21(7), 1157–1162.

Eckhardt, R. (1987), Stan Ulam, John von Neumann, and the Monte Carlo method, *Los Alamos Science*, pp. 131–141.

Ellett, W. & Humes, R. (1972), MIRD pamphlet no. 8: absorbed fractions for small volumes containing photon - emitting radioactivity, *J Nucl Med*, Suppl No 6, 7.

Ersahin, D., Doddamane, I. & Cheng, D. (2011), Targeted radionuclide therapy, *Cancers*, 3(4), 3838–3855.

Fernández, M., Hänscheid, H., Mauxion, T., Bardiès, M., Kletting, P., Glatting, G. & Lassmann, M. (2013), A fast method for rescaling voxel S values for arbitrary voxel sizes in targeted radionuclide therapy from a single Monte Carlo calculation, *Med Phys*, 40(8), 082502.

Flöry, S. & Hofer, M. (2010), Surface fitting and registration of point clouds using approximations of the unsigned distance function, *Comput Aided Geom D*, 27(1), 60–77.

Flux, G., Bardies, M., Monsieurs, M., Savolainen, S., Strand, S.-E. & Lassmann, M. (2006), The impact of PET and SPECT on dosimetry for targeted radionuclide therapy, *Z Med Phys*, 16(1), 47–59.

Flux, G. D., Haq, M., Chittenden, S. J., Buckley, S., Hindorf, C., Newbold, K. & Harmer, C. L. (2010), A dose-effect correlation for radioiodine ablation in differentiated thyroid cancer, *Eur J Nucl Med Mol Imaging*, 37(2), 270–275.

Flynn, A. A., Pedley, R. B., Green, A. J., Dearling, J. L., El-Emir, E., Boxer, G. M., Boden, R. & Begent, R. H. (2003), The nonuniformity of antibody distribution in the kidney and its influence on dosimetry, *Radiat Res*, 159(2), 182–189.

Fong, D. C.-L. & Saunders, M. (2011), LSMR: an iterative algorithm for sparse least-squares problems, *SIAM J Sci Comput*, 33(5), 2950–2971.

Forrer, F., Krenning, E. P., Kooij, P. P., Bernard, B. F., Konijnenberg, M., Bakker, W. H., Teunissen, J. J. M., de Jong, M., van Lom, K., de Herder, W. W. & Kwekkeboom, D. J. (2009), Bone marrow dosimetry in peptide receptor radionuclide therapy with [^{177}Lu-DOTA^{0},tyr^{3}]octreotate, *Eur J Nucl Med Mol Imaging*, 36(7), 1138–1146.

Frantz, V. K., Ball, R. P., Keston, A. S. & Palmer, W. W. (1944), Thyroid carcinoma with metastases: studied with radioactive iodine, *Ann Surg*, 119(5), 668.

Frey, E. C., Humm, J. L. & Ljungberg, M. (2012), Accuracy and precision of radioactivity quantification in nuclear medicine images, *Semin Nucl Med*, 42(3), 208–218.

Furhang, E. E., Chui, C. S., Kolbert, K. S., Larson, S. M. & Sgouros, G. (1997), Implementation of a Monte Carlo dosimetry method for patient-specific internal emitter therapy, *Med Phys*, 24(7), 1163–1172.

Gardin, I., Bouchet, L. G., Assié, K., Caron, J., Lisbona, A., Ferrer, L., Bolch, W. E. & Vera, P. (2003), Voxeldose: a computer program for 3-D dose calculation in therapeutic nuclear medicine, *Cancer Biother Radiopharm*, 18(1), 109–115.

Giammarile, F., Bodei, L., Chiesa, C., Flux, G., Forrer, F., Kraeber-Bodere, F., Brans, B., Lambert, B., Konijnenberg, M., Borson-Chazot, F. et al. (2011), EANM procedure guideline for the treatment of liver cancer and liver metastases with intra-arterial radioactive compounds, *Eur J Nucl Med Mol Imaging*, 38(7), 1393–1406.

Greenberg, J. S. & Deutsch, M. (1956), Positrons from the decay of P^{32} and Y^{90}, *Phys Rev*, 102, 415–421.

Guy, M. J., Flux, G. D., Papavasileiou, P., Flower, M. A. & Ott, R. J. (2003), RMDP: a dedicated package for ^{131}I SPECT quantification, registration and patient-specific dosimetry, *Cancer Biother Radiopharm*, 18(1), 61–69.

Hall, E. J. & Giaccia, A. J. (2006), *Radiobiology for the Radiologist*, Lippincott Williams & Wilkins, Philadelphia, PA.

Hamburg, M. A. & Collins, F. S. (2010), The path to personalized medicine, *N Engl J Med*, 363(4), 301–304.

Harrison, R. L. (2010), Introduction to Monte Carlo simulation, *in* 'AIP conference proceedings', Vol. 1204, p. 17.

Hastings, W. K. (1970), Monte Carlo sampling methods using Markov chains and their applications, *Biometrika*, 57(1), 97–109.

Hauf, S., Kuster, M., Batic, M., Bell, Z., Hoffmann, D., Lang, P., Neff, S., Pia, M., Weidenspointner, G. & Zoglauer, A. (2013*a*), Radioactive decays in Geant4, *IEEE T Nucl Sci*, 60, 2966–2983.

Hauf, S., Kuster, M., Batic, M., Bell, Z., Hoffmann, D., Lang, P., Neff, S., Pia, M., Weidenspointner, G. & Zoglauer, A. (2013*b*), Validation of Geant4-based radioactive decay simulation, *IEEE T Nucl Sci*, 60(4), 2984–2997.

He, B., Du, Y., Segars, W. P., Wahl, R. L., Sgouros, G., Jacene, H. & Frey, E. C. (2009), Evaluation of quantitative imaging methods for organ activity and residence time estimation using a population of phantoms having realistic variations in anatomy and uptake, *Med Phys*, 36(2), 612–619.

He, B., Du, Y., Song, X., Segars, W. P. & Frey, E. C. (2005), A Monte Carlo and physical phantom evaluation of quantitative In-111 SPECT, *Phys Med Biol*, 50(17), 4169.

He, B. & Frey, E. C. (2006), Comparison of conventional, model-based quantitative planar, and quantitative SPECT image processing methods for organ activity estimation using In-111 agents, *Phys Med Biol*, 51(16), 3967–3981.

He, B. & Frey, E. C. (2010), The impact of 3D volume of interest definition on accuracy and precision of activity estimation in quantitative SPECT and planar processing methods, *Phys Med Biol*, 55(12), 3535–3544.

Hermoye, L., Laamari-Azjal, I., Cao, Z., Annet, L., Lerut, J., Dawant, B. M. & Van Beers, B. E. (2005), Liver segmentation in living liver transplant donors: comparison of semiautomatic and manual methods, *Radiology*, 234(1), 171–178.

Hertz, S. & Roberts, A. (1946), Radioactive iodine in the study of thyroid physiology. VII. The use of radioactive iodine therapy in hyperthyroidism, *JAMA*, 131(2), 81–86.

Hirayama, H., Namito, Y., Nelson, W. R., Bielajew, A. F., Wilderman, S. J. & Michigan, U. (2005), The EGS5 code system, Technical report, United States Department of Energy.

Hobbs, R. F., Wahl, R. L., Frey, E. C., Kasamon, Y., Song, H., Huang, P., Jones, R. J. & Sgouros, G. (2013*a*), Radiobiologic optimization of combination radiopharmaceutical therapy applied to myeloablative treatment of non-Hodgkin lymphoma, *J Nucl Med*, 54(9), 1535–1542.

Hobbs, R. F., Wahl, R. L., Lodge, M. A., Javadi, M. S., Cho, S. Y., Chien, D. T., Ewertz, M. E., Esaias, C. E., Ladenson, P. W. & Sgouros, G. (2009), ^{124}I PET-based 3D-RD dosimetry for a pediatric thyroid cancer patient: real-time treatment planning and methodologic comparison, *J Nucl Med*, 50(11), 1844–1847.

Hobbs, R., Jentzen, W., Bockisch, A. & Sgouros, G. (2013), Monte Carlo-based 3-dimensional dosimetry of salivary glands in radioiodine treatment of differentiated thyroid cancer estimated using ^{124}I PET, *Q J Nucl Med Mol Imaging*, 57(1), 79.

Howard, D. M., Kearfott, K. J., Wilderman, S. J. & Dewaraja, Y. K. (2011), Comparison of I-131 radioimmunotherapy tumor dosimetry: unit density sphere model versus patient-specific Monte Carlo calculations, *Cancer Biother Radiopharm*, 26(5), 615–621.

Hu, S.-M. & Wallner, J. (2005), A second order algorithm for orthogonal projection onto curves and surfaces, *Comput Aided Geom D*, 22(3), 251–260.

ICRP (1975), *Report of the Task Group on Reference Man*, ICRP Publication 23. Pergamon Press, Oxford, U.K.

ICRP (2002), *Basic Anatomical and Physiological Data for Use in Radiological Protection: Reference Values*, ICRP Publication 89. Pergamon Press, Oxford, U.K.

ICRU (1992), *Photon, Electron, Proton and Neutron Interaction Data for Body Tissue*, ICRU Report 46. International Commission on Radiation Units and Measurements, Bethesda, MD.

Ivanchenko, V., Apostolakis, J., Bagulya, A., Abdelouahed, H., Black, R., Bogdanov, A., Burkhard, H., Chauvie, S., Cirrone, P., Cuttone, G. et al. (2011), Recent improvements in Geant4 electromagnetic physics models and interfaces, *in* T. Takeda, ed., 'Progress in Nuclear Science and Technology', Vol. 2, Atomic Energy Society of Japan, pp. 898–903.

Ivanchenko, V., Kadri, O., Maire, M. & Urban, L. (2010), Geant4 models for simulation of multiple scattering, *in* 'Journal of Physics: Conference Series', Vol. 219, p. 032045.

Jaccard, P. (1912), The distribution of the flora of the alpine zone, *New Phytol*, 11, 37–50.

Jackson, P. A., Beauregard, J.-M., Hofman, M. S., Kron, T., Hogg, A. & Hicks, R. J. (2013), An automated voxelized dosimetry tool for radionuclide therapy based on serial quantitative SPECT/CT imaging, *Med Phys*, 40(11), 112503.

Jiang, H. & Paganetti, H. (2004), Adaptation of GEANT4 to Monte Carlo dose calculations based on CT data, *Med Phys*, 31(10), 2811–2818.

Johnson, P. B., Whalen, S. R., Wayson, M., Juneja, B., Lee, C. & Bolch, W. E. (2009), Hybrid patient-dependent phantoms covering statistical distributions of body morphometry in the US adult and pediatric population, *Proc IEEE*, 97(12), 2060–2075.

Johnson, T. K., McClure, D. & McCourt, S. (1999), MABDOSE I: characterization of a general purpose dose estimation code, *Med Phys*, 26(7), 1389–1395.

Jönsson, H. & Mattsson, S. (2004), Excess radiation absorbed doses from non-optimised radioiodine treatment of hyperthyroidism, *Radiat Prot Dosim*, 108(2), 107–114.

Kaminski, M. S., Tuck, M., Estes, J., Kolstad, A., Ross, C. W., Zasadny, K., Regan, D., Kison, P., Fisher, S., Kroll, S. et al. (2005), ^{131}I-tositumomab therapy as initial treatment for follicular lymphoma, *N Engl J Med*, 352(5), 441–449.

Kao, Y.-H., Steinberg, J. D., Tay, Y.-S., Lim, G. K., Yan, J., Townsend, D. W., Takano, A., Burgmans, M. C., Irani, F. G., Teo, T. K. et al. (2013), Post-radioembolization yttrium-90 PET/CT – part 1: diagnostic reporting, *EJNMMI Res*, 3, 56.

Kao, Y. H., Tan, E. H., Ng, C. E. & Goh, S. W. (2011), Yttrium-90 time-of-flight PET/CT is superior to bremsstrahlung SPECT/CT for postradioembolization imaging of microsphere biodistribution, *Clin Nucl Med*, 36(12), e186–e187.

Karp, J. S., Surti, S., Daube-Witherspoon, M. E. & Muehllehner, G. (2008), Benefit of time-of-flight in PET: experimental and clinical results, *J Nucl Med*, 49(3), 462–470.

Kessler, R. M., Seibyl, J., Cowan, R. L., Zald, D., Young, J. S., Ansari, M. S. & Stabin, M. G. (2014), Radiation dosimetry of ^{18}F-FPEB in humans, *J Nucl Med*, 55(7), 1119–1121.

Kolbert, K. S., Pentlow, K. S., Pearson, J. R., Sheikh, A., Finn, R. D., Humm, J. L. & Larson, S. M. (2007), Prediction of absorbed dose to normal organs in thyroid cancer patients treated with ^{131}I by use of ^{124}I PET and 3-dimensional internal dosimetry software, *J Nucl Med*, 48(1), 143–149.

Kolbert, K. S., Sgouros, G., Scott, A. M., Bronstein, J. E., Malane, R. A., Zhang, J., Kalaigian, H., McNamara, S., Schwartz, L. & Larson, S. M. (1997), Implementation and evaluation of patient-specific three-dimensional internal dosimetry, *J Nucl Med*, 38(2), 301–307.

Koral, K. F., Yendiki, A., Lin, Q. & Dewaraja, Y. K. (2005), Comparison of 3-D OSEM versus 1-D SAGE for focal total-activity quantification in I-131 SPECT with HE collimation, *IEEE T Nucl Sci*, 52(1), 154–158.

Kost, S. D., Dewaraja, Y. K., Abramson, R. G. & Stabin, M. G. (2015), VIDA: a voxel-based dosimetry method for targeted radionuclide therapy using Geant4, *Cancer Biother Radiopharm*, 30(1), 16–26.

Kramer, R., Zankl, M., Williams, G. & Drexler, G. (1982), The calculation of dose from external photon exposures using reference human phantoms and Monte Carlo methods, Part 1: the male (ADAM) and female (EVA) adult mathematical phantoms, Technical Report GSF-Report S-885, GSF–National Research Center for Environment and Health.

Kwekkeboom, D., Bakker, W., Kam, B., Teunissen, J., Kooij, P., De Herder, W., Feelders, R., van Eijck, C., De Jong, M., Srinivasan, A. et al. (2003), Treatment of patients with gastro-entero-pancreatic (GEP) tumours with the novel radiolabelled somatostatin analogue [^{177}Lu-DOTA0, Tyr3] octreotate, *Eur J Nucl Med Mol Imaging*, 30(3), 417–422.

Lanconelli, N., Pacilio, M., Meo, S. L., Botta, F., Di Dia, A., Aroche, L. T., Pérez, M. C. & Cremonesi, M. (2012), A free database of radionuclide voxel S values for the dosimetry of nonuniform activity distributions, *Phys Med Biol*, 57(2), 517.

Lassmann, M., Reiners, C. & Luster, M. (2010), Dosimetry and thyroid cancer: the individual dosage of radioiodine, *Endocr Relat Cancer*, 17(3), R161–R172.

Lechner, A., Pia, M. & Sudhakar, M. (2009), Validation of Geant4 low energy electromagnetic processes against precision measurements of electron energy deposition, *IEEE T Nucl Sci*, 56(2), 398–416.

Levin, C. S. & Hoffman, E. J. (1999), Calculation of positron range and its effect on the fundamental limit of positron emission tomography system spatial resolution, *Phys Med Biol*, 44(3), 781.

Lhommel, R., Goffette, P., Van den Eynde, M., Jamar, F., Pauwels, S., Bilbao, J. I. & Walrand, S. (2009), Yttrium-90 TOF PET scan demonstrates high-resolution biodistribution after liver SIRT, *Eur J Nucl Med Mol Imaging*, 36(10), 1696.

Ljungberg, M. & Sjögreen-Gleisner, K. (2011), The accuracy of absorbed dose estimates in tumours determined by quantitative SPECT: a Monte Carlo study, *Acta Oncol*, 50(6), 981–989.

Ljungberg, M., Sjögreen, K., Liu, X., Frey, E., Dewaraja, Y. & Strand, S.-E. (2002), A 3-dimensional absorbed dose calculation method based on quantitative SPECT for radionuclide therapy: evaluation for ^{131}I using Monte Carlo simulation, *J Nucl Med*, 43(8), 1101–1109.

Ljungberg, M. & Strand, S.-E. (1989), A Monte Carlo program for the simulation of scintillation camera characteristics, *Comput Methods Programs Biomed*, 29(4), 257–272.

Loevinger, R. & Berman, M. (1976), *A Revised Schema for Absorbed-dose Calculations for Biologically Distributed Radionuclides*, MIRD Pamphlet 1 – Revised. Society of Nuclear Medicine, New York, NY.

Loevinger, R., Budinger, T. F. & Watson, E. E. (1988), *MIRD Primer for Absorbed Dose Calculations*, Society of Nuclear Medicine, New York, NY.

Loudos, G., Tsougos, I., Boukis, S., Karakatsanis, N., Georgoulias, P., Theodorou, K., Nikita, K. & Kappas, C. (2009), A radionuclide dosimetry toolkit based on material-specific Monte Carlo dose kernels, *Nucl Med Commun*, 30(7), 504–512.

Ma, Y. L. & Hewitt, W. (2003), Point inversion and projection for NURBS curve and surface: control polygon approach, *Comput Aided Geom D*, 20(2), 79–99.

Machac, J., Weintraub, J., Nowakowski, F., Mobley, D., Zhang, Z. & Warner, R. (2007), Variations in liver perfusion patterns in patients with liver tumors undergoing therapy with yttrium-90 microspheres studied with SPECT/CT, *J Nucl Med*, 48, 396P.

Madsen, M. T. (2007), Recent advances in SPECT imaging, *J Nucl Med*, 48(4), 661–673.

Marcatili, S., Pettinato, C., Daniels, S., Lewis, G., Edwards, P., Fanti, S. & Spezi, E. (2013), Development and validation of RAYDOSE: a Geant4-based application for molecular radiotherapy, *Phys Med Biol*, 58(8), 2491–2508.

Marine, P. M., Stabin, M. G., Fernald, M. J. & Brill, A. B. (2010), Changes in radiation dose with variations in human anatomy: larger and smaller normal-stature adults, *J Nucl Med*, 51(5), 806–811.

McKay, E. (2011), GRNT: A Geant4 code for radionuclide therapy dosimetry, *in* 'University of Wollongong, Geant4 Workshop'.

Meller, S. (1997), Targeted radiotherapy for neuroblastoma, *Arch Dis Child*, 77(5), 389–392.

Milroy, M., Bradley, C., Vickers, G. & Weir, D. (1995), G1 continuity of B-spline surface patches in reverse engineering, *Comput Aided Des*, 27(6), 471–478.

Mishchenko, Y. (2015), A fast algorithm for computation of discrete Euclidean distance transform in three or more dimensions on vector processing architectures, *Signal Image Video P*, 9(1), 19–27.

Mukherjee, J., Kaltsas, G., Islam, N., Plowman, P., Foley, R., Hikmat, J., Britton, K., Jenkins, P., Chew, S. & Monson, J. (2001), Treatment of metastatic carcinoid tumours, phaeochromocytoma, paraganglioma and medullary carcinoma of the thyroid with ^{131}I-meta-iodobenzylguanidine (^{131}I-mIBG), *Clin Endocrinol*, 55(1), 47–60.

Neumann, J. v. (1951), Various techniques used in connection with random digits. Monte Carlo methods, *Nat Bureau Standards*, 12, 36–38.

Niemierko, A. (1997), Reporting and analyzing dose distributions: a concept of equivalent uniform dose, *Med Phys*, 24(1), 103–110.

Norris, H., Zhang, Y., Bond, J., Sturgeon, G. M., Minhas, A., Tward, D. J., Ratnanather, J. T., Miller, M. I., Frush, D., Samei, E. & Segars, W. P. (2014), A set of 4D pediatric XCAT reference phantoms for multimodality research, *Med Phys*, 41(3), 033701.

Norris, H., Zhang, Y., Frush, J., Sturgeon, G. M., Minhas, A., Tward, D. J., Ratnanather, J. T., Miller, M. I., Frush, D., Samei, E. & Segars, W. P. (2014*a*), The development of a population of 4D pediatric XCAT phantoms for CT imaging research and optimization, *Proc. SPIE*, 9033, 90331V.

O'Donoghue, J. A. (1999), Implications of nonuniform tumor doses for radioimmunotherapy, *J Nucl Med*, 40(8), 1337–1341.

Papavasileiou, P., Divoli, A., Hatziioannou, K. & Flux, G. D. (2007), The importance of the accuracy of image registration of SPECT images for 3D targeted radionuclide therapy dosimetry, *Phys Med Biol*, 52(24), N539.

Parker, C., Nilsson, S., Heinrich, D., Helle, S., O'Sullivan, J., Fosså, S., Chodacki, A., Wiechno, P., Logue, J., Seke, M. et al. (2013), Alpha emitter radium-223 and survival in metastatic prostate cancer, *N Engl J Med*, 369(3), 213–223.

Pentlow, K. S., Graham, M., Lambrecht, R., Cheung, N.-K. & Larson, S. (1991), Quantitative imaging of I-124 using positron emission tomography with applications to radioimmunodiagnosis and radioimmunotherapy, *Med Phys*, 18(3), 357–366.

Pereira, J., Stabin, M., Lima, F., Guimarães, M. & Forrester, J. (2010), Image quantification for radiation dose calculations–limitations and uncertainties, *Health Phys*, 99(5), 688.

Petoussi-Henss, N., Zankl, M., Fill, U. & Regulla, D. (2002), The GSF family of voxel phantoms, *Phys Med Biol*, 47(1), 89.

Pichardo, J. C., Trindade, A. A., Brindle, J. M. & Bolch, W. E. (2007), Method for estimating skeletal spongiosa volume and active marrow mass in the adult male and adult female, *J Nucl Med*, 48(11), 1880–1888.

Piegl, L. & Tiller, W. (1997), *The NURBS Book*, Springer-Verlag, New York, NY.

Pottmann, H. & Leopoldseder, S. (2003), A concept for parametric surface fitting which avoids the parametrization problem, *Comput Aided G*, 20(6), 343–362.

Prideaux, A. R., Song, H., Hobbs, R. F., He, B., Frey, E. C., Ladenson, P. W., Wahl, R. L. & Sgouros, G. (2007), Three-dimensional radiobiologic dosimetry: application of radiobiologic modeling to patient-specific 3-dimensional imaging–based internal dosimetry, *J Nucl Med*, 48(6), 1008–1016.

Prvulovich, E. M., Stein, R. C., Bomanji, J. B., Ledermann, J. A., Taylor, I. & Ell, P. J. (1998), Iodine-131-MIBG therapy of a patient with carcinoid liver metastases, *J Nucl Med*, 39(10), 1743.

Rao, M., Stough, J., Chi, Y.-Y., Muller, K., Tracton, G., Pizer, S. M. & Chaney, E. L. (2005), Comparison of human and automatic segmentations of kidneys from CT images, *Int J Radiation Oncology Biol Phys*, 61(3), 954–960.

Raychaudhuri, S. (2008), Introduction to Monte Carlo simulation, *in* 'Winter Simulation Conference, Dec. 2008', pp. 91–100.

Ristic, M., Brujic, D. & Ainsworth, I. (2004), Measurement-based updating of turbine blade CAD models: a case study, *Int J Comp Integ M*, 17(4), 352–363.

Rubinstein, R. Y. & Kroese, D. P. (2011), *Simulation and the Monte Carlo Method*, John Wiley & Sons, Hoboken, NJ.

Sandström, M., Garske-Román, U., Granberg, D., Johansson, S., Widström, C., Eriksson, B., Sundin, A., Lundqvist, H. & Lubberink, M. (2013), Individualized dosimetry of kidney and bone marrow in patients undergoing ^{177}Lu-DOTA-octreotate treatment, *J Nucl Med*, 54(1), 33–41.

Schipper, M., Koral, K., Avram, A., Kaminski, M. & Dewaraja, Y. (2012), Prediction of therapy tumor-absorbed dose estimates in I-131 radioimmunotherapy using tracer data via a mixed-model fit to time activity, *Cancer Biother Radiopharm*, 27(7), 403–411.

Schneider, U., Pedroni, E. & Lomax, A. (1996), The calibration of CT Hounsfield units for radiotherapy treatment planning, *Phys Med Biol*, 41(1), 111–124.

Segars, W., Lalush, D. & Tsui, B. (1999), A realistic spline-based dynamic heart phantom, *IEEE Trans Nucl Sci*, 46(3), 503–506.

Segars, W., Lalush, D. & Tsui, B. (2000), Development of an interactive software application to model patient populations in the 4D NURBS-based cardiac torso phantom, *in* 'IEEE Med Imag Nucl Sci Symp Conf Rec', Vol. 3, pp. 20/51–20/55.

Segars, W., Lalush, D. & Tsui, B. (2001*a*), Modeling respiratory mechanics in the MCAT and spline-based MCAT phantoms, *IEEE Trans Nucl Sci*, 48(1), 89–97.

Segars, W. P., Bond, J., Frush, J., Hon, S., Eckersley, C., Williams, C. H., Feng, J., Tward, D. J., Ratnanather, J. T., Miller, M. I., Frush, D. & Samei, E. (2013), Population of anatomically variable 4D XCAT adult phantoms for imaging research and optimization, *Med Phys*, 40(4), 043701.

Segars, W. P., Sturgeon, G., Li, X., Cheng, L., Ceritoglu, C., Ratnanather, J. T., Miller, M. I., Tsui, B. M. W., Frush, D. & Samei, E. (2009), Patient specific computerized phantoms to estimate dose in pediatric CT, *Proc. SPIE*, 7258, 72580H.

Segars, W. P., Tsui, B., Lalush, D., Frey, E., King, M. & Manocha, D. (2001), Development and Application of the New Dynamic NURBS-based Cardiac-Torso (NCAT) Phantom, PhD thesis, University of North Carolina at Chapel Hill.

Segars, W., Sturgeon, G., Mendonca, S., Grimes, J. & Tsui, B. (2010), 4D XCAT phantom for multimodality imaging research, *Med Phys*, 37, 4902.

Senthamizhchelvan, S., Hobbs, R. F., Song, H., Frey, E. C., Zhang, Z., Armour, E., Wahl, R. L., Loeb, D. M. & Sgouros, G. (2012), Tumor dosimetry and response for ^{153}Sm-ethylenediamine tetramethylene phosphonic acid therapy of high-risk osteosarcoma, *J Nucl Med*, 53(2), 215–224.

Sgouros, G., Frey, E., Wahl, R., He, B., Prideaux, A. & Hobbs, R. (2008), Three-dimensional imaging-based radiobiological dosimetry, *Semin*, 38(5), 321–334.

Sgouros, G. & Hobbs, R. F. (2014), Dosimetry for radiopharmaceutical therapy, *Semin Nucl Med*, 44(3), 172–178.

Sgouros, G., Hobbs, R. F., Atkins, F. B., Van Nostrand, D., Ladenson, P. W. & Wahl, R. L. (2011), Three-dimensional radiobiological dosimetry (3D-RD) with ^{124}I PET for ^{131}I therapy of thyroid cancer, *Eur J Nucl Med Mol Imaging*, 38(1), 41–47.

Sgouros, G., Kolbert, K. S., Sheikh, A., Pentlow, K. S., Mun, E. F., Barth, A., Robbins, R. J. & Larson, S. M. (2004), Patient-specific dosimetry for ^{131}I thyroid cancer therapy using ^{124}I PET and 3-dimensional-internal dosimetry (3D-ID) software, *J Nucl Med*, 45(8), 1366–1372.

Sgouros, G., Squeri, S., Ballangrud, Å. M., Kolbert, K. S., Teitcher, J. B., Panageas, K. S., Finn, R. D., Divgi, C. R., Larson, S. M. & Zelenetz, A. D. (2003), Patient-specific, 3-dimensional dosimetry in non-Hodgkin's lymphoma patients treated with ^{131}I-anti-B1 antibody: assessment of tumor dose-response, *J Nucl Med*, 44(2), 260–268.

Shcherbinin, S., Celler, A., Belhocine, T., Vanderwerf, R. & Driedger, A. (2008), Accuracy of quantitative reconstructions in SPECT/CT imaging, *Phys Med Biol*, 53(17), 4595.

Shcherbinin, S., Grimes, J., Bator, A., Cwikla, J. & Celler, A. (2014), Three-dimensional personalized dosimetry for ^{188}Re liver selective internal radiation therapy based on quantitative post-treatment SPECT studies, *Phys Med Biol*, 59(1), 119.

Shcherbinin, S., Piwowarska-Bilska, H., Celler, A. & Birkenfeld, B. (2012), Quantitative SPECT/CT reconstruction for ^{177}Lu and ^{177}Lu/^{90}Y targeted radionuclide therapies, *Phys Med Biol*, 57(18), 5733.

Shepp, L. & Logan, B. (1974), The Fourier reconstruction of a head section, *IEEE T Nucl Sci*, 21(3), 21–43.

Shibuya, K., Yoshida, E., Nishikido, F., Suzuki, T., Tsuda, T., Inadama, N., Yamaya, T. & Murayama, H. (2007), Limit of spatial resolution in FDG-PET due to annihilation photon non-collinearity, *in* R. Magjarevic & J. Nagel, eds, 'World Congress on Medical Physics and Biomedical Engineering 2006', Vol. 14 of *IFMBE Proceedings*, pp. 1667–1671.

Siegel, J. A., Thomas, S. R., Stubbs, J. B., Stabin, M. G., Hays, M. T., Koral, K. F., Robertson, J. S., Howell, R. W., Wessels, B. W., Fisher, D. R. et al. (1999), MIRD pamphlet no. 16: techniques for quantitative radiopharmaceutical biodistribution data acquisition and analysis for use in human radiation dose estimates, *J Nucl Med*, 40, 37S–61S.

Sjögreen-Gleisner, K., Rueckert, D. & Ljungberg, M. (2009), Registration of serial SPECT/CT images for three-dimensional dosimetry in radionuclide therapy, *Phys Med Biol*, 54(20), 6181.

Snyder, W., Ford, M., Warner, G. & Watson, B. (1969), Estimates of absorbed fractions for monoenergetic photon sources uniformly distributed in various organs of a heterogeneous phantom, *J Nucl Med*, 10, 7S–52S.

Snyder, W. S., Ford, M. R. & Warner, G. G. (1978), *MIRD Pamphlet No. 5, Revised: Estimates of Specific Absorbed Fractions for Photon Sources Uniformly Distributed in Various Organs of a Heterogeneous Phantom*, New York, NY.

Stabin, M., E, W. & Cristy, M. (1995), Mathematical models and specific absorbed fractions of photon energy in the nonpregnant adult female and at the end of each trimester of pregnancy, Technical Report ORNL/TM-12907, Oak Ridge, TN: Oak Ridge National Laboratory.

Stabin, M. G. (1996), MIRDOSE: personal computer software for internal dose assessment in nuclear medicine, *J Nucl Med*, 37(3), 538–546.

Stabin, M. G. (2007), *Radiation Protection and Dosimetry: An Introduction to Health Physics*, Springer, New York, NY.

Stabin, M. G. (2008*a*), *Fundamentals of Nuclear Medicine Dosimetry*, Springer, New York, NY.

Stabin, M. G. (2008*b*), Uncertainties in internal dose calculations for radiopharmaceuticals, *J Nucl Med*, 49(5), 853–860.

Stabin, M. G. (2008*c*), Update: the case for patient-specific dosimetry in radionuclide therapy, *Cancer Biother Radiopharm*, 23(3), 273–284.

Stabin, M. G. & Konijnenberg, M. W. (2000), Re-evaluation of absorbed fractions for photons and electrons in spheres of various sizes, *J Nucl Med*, 41(1), 149–160.

Stabin, M. G. & Siegel, J. A. (2003), Physical models and dose factors for use in internal dose assessment, *Health Phys*, 85(3), 294–310.

Stabin, M. G., Sparks, R. B. & Crowe, E. (2005), OLINDA/EXM: the second-generation personal computer software for internal dose assessment in nuclear medicine, *J Nucl Med*, 46(6), 1023–1027.

Stabin, M. G., Xu, X. G., Emmons, M. A., Segars, W. P., Shi, C. & Fernald, M. J. (2012), RADAR reference adult, pediatric, and pregnant female phantom series for internal and external dosimetry, *J Nucl Med*, 53(11), 1807–1813.

Stillebroer, A. B., Zegers, C. M., Boerman, O. C., Oosterwijk, E., Mulders, P. F., O'Donoghue, J. A., Visser, E. P. & Oyen, W. J. (2012), Dosimetric analysis of ^{177}Lu-cG250 radioimmunotherapy in renal cell carcinoma patients: correlation with myelotoxicity and pretherapeutic absorbed dose predictions based on ^{111}In-cG250 imaging, *J Nucl Med*, 53(1), 82–89.

Strigari, L., Konijnenberg, M., Chiesa, C., Bardies, M., Du, Y., Gleisner, K. S., Lassmann, M. & Flux, G. (2014), The evidence base for the use of internal dosimetry in the clinical practice of molecular radiotherapy, *Eur J Nucl Med Mol Imaging*, pp. 1–13.

Strigari, L., Menghi, E., D'Andrea, M. & Benassi, M. (2006), Monte Carlo dose voxel kernel calculations of beta-emitting and Auger-emitting radionuclides for internal dosimetry: a comparison between EGSnrcMP and EGS4, *Med Phys*, 33(9), 3383–3389.

Sutherland, K., S, M. & Date, H. (2007), A simple parallelization of GEANT4 on a PC cluster with static scheduling for dose calculations, *J Phys: Conf Ser*, 74(1), 021020.

Sweezy, J. E., Booth, T. E., Brown, F. B., Bull, J. S., Forster, R. A., Goorley, J. T., Hughes, H. G., Mosteller, R. D., Prael, R. E., Sood, A. & Zukaitis, A. (2003), MCNP–a general Monte Carlo N-particle transport code, version 5, *Los Alamos, NM: Los Alamos National Laboratory*, .

Tagesson, M., Ljungberg, M. & Strand, S.-E. (1996), A Monte Carlo program converting activity distributions to absorbed dose distributions in a radionuclide treatment planning system, *Acta Oncol*, 35(3), 367–372.

Tsougos, I., Loudos, G., Georgoulias, P., Theodorou, K. & Kappas, C. (2010), Patient-specific internal radionuclide dosimetry, *Nucl Med Commun*, 31(2), 97–106.

Tuli, J. (1996), Evaluated nuclear structure data file, *Nucl Instrum Meth A*, 369(2), 506–510.

Tward, D. J., Ceritoglu, C., Kolasny, A., Sturgeon, G. M., Segars, W. P., Miller, M. I. & Ratnanather, J. T. (2011), Patient specific dosimetry phantoms using multichannel LDDMM of the whole body, *Int J Biomed Imaging*, 2011, 3:1–3:9.

Valentin, J. (2002), Basic anatomical and physiological data for use in radiological protection: reference values: ICRP Publication 89, *Annals of the ICRP*, 32(3), 1–277.

Valkema, R., de Jong, M., Bakker, W. H., Breeman, W. A., Kooij, P. P., Lugtenburg, P. J., de Jong, F. H., Christiansen, A., Kam, B. L., de Herder, W. W. et al. (2002), Phase I study of peptide receptor radionuclide therapy with [^{111}In-DTPA0]octreotide: the Rotterdam experience, *Semin Nucl Med*, 32(2), 110–122.

Van Ginneken, B., Heimann, T. & Styner, M. (2007), 3D segmentation in the clinic: a grand challenge, *in* 'Medical Image Computing and Computer Assisted Intervention'.

Veit, R., Zankl, M., Petoussi, N., Mannweiler, E., Williams, G. & Drexler, G. (1989), Tomographic anthropomorphic models, part I: construction technique and description of models of an 8 week old baby and a 7 year old child, Technical Report GSF-Bericht 3/89, GSF–National Research Center for Environment and Health.

Viola, P. & Wells III, W. (1997), Alignment by maximization of mutual information, *Int J Comput Vision*, 24(2), 137–154.

Walrand, S., Hesse, M., Demonceau, G., Pauwels, S. & Jamar, F. (2011), Yttrium-90-labeled microsphere tracking during liver selective internal radiotherapy by bremsstrahlung pinhole SPECT: feasibility study and evaluation in an abdominal phantom, *EJNMMI Res*, 1(1), 1–14.

Wang, W., Pottmann, H. & Liu, Y. (2006), Fitting B-spline curves to point clouds by curvature-based squared distance minimization, *ACM Trans Graph*, 25(2), 214–238.

Wessels, B. W., Konijnenberg, M. W., Dale, R. G., Breitz, H. B., Cremonesi, M., Meredith, R. F., Green, A. J., Bouchet, L. G., Brill, A. B., Bolch, W. E. et al. (2008), MIRD pamphlet no. 20: the effect of model assumptions on kidney dosimetry and response – implications for radionuclide therapy, *J Nucl Med*, 49(11), 1884–1899.

Wilderman, S. & Dewaraja, Y. (2007), Method for fast CT/SPECT-based 3D Monte Carlo absorbed dose computations in internal emitter therapy, *IEEE T Nucl Sci*, 54(1), 146–151.

Williams, G., Zankl, M., Abmayr, W., Veit, R. & Drexler, G. (1986), The calculations of dose from external photon exposures using reference and realistic human phantoms and Monte Carlo methods, *Phys Med Biol*, 31(4), 449–452.

Witzig, T. E., Gordon, L. I., Cabanillas, F., Czuczman, M. S., Emmanouilides, C., Joyce, R., Pohlman, B. L., Bartlett, N. L., Wiseman, G. A., Padre, N. et al. (2002), Randomized controlled trial of yttrium-90–labeled ibritumomab tiuxetan radioimmunotherapy versus rituximab immunotherapy for patients with relapsed or refractory low-grade, follicular, or transformed B-cell non-Hodgkin's lymphoma, *J Clin Oncol*, 20(10), 2453–2463.

Xu, X., Chao, T. & Bozkurt, A. (2000), VIP-man: an image-based whole-body adult male model constructed from color photographs of the Visible Human Project for multi-particle Monte Carlo calculations, *Health Phys*, 78(5), 476–486.

Xu, X. G. & Eckerman, K. F., eds (2010), *Handbook of Anatomical Models for Radiation Dosimetry*, CRC Press, New York, NY.

Yoriyaz, H., Stabin, M. G. & dos Santos, A. (2001), Monte Carlo MCNP-4B–based absorbed dose distribution estimates for patient-specific dosimetry, *J Nucl Med*, 42(4), 662–669.

Yushkevich, P., Piven, J., Hazlett, H., Smith, R., Ho, S., Gee, J. & Gerig, G. (2006), User-guided 3D active contour segmentation of anatomical structures: significantly improved efficiency and reliability, *Neuroimage*, 31(3), 1116–1128.

Zankl, M., Veit, R., Williams, G., Schneider, K., Fendel, H., Petoussi, N. & Drexler, G. (1988), The construction of computer tomographic phantoms and their application in radiology and radiation protection, *Radiat Environ Biophys*, 27(2), 153–164.

Zankl, M. & Wittmann, A. (2001), The adult male voxel model "Golem" segmented from whole-body CT patient data, *Radiat Environ Biophys*, 40(2), 153–162.

Zubal, I. G., Harrell, C. R., Smith, E. O., Rattner, Z., Gindi, G. & Hoffer, P. B. (1994), Computerized three-dimensional segmented human anatomy, *Med Phys*, 21, 299–302.